Mösl Thomas, BSc

Design and Validation of a Sensor System for the Determination of Phase and Concentration of Water in the Exhaust Tract of a Fuel Cell

MASTER'S THESIS

to achieve the university degree of

Diplom-Ingenieur

Master's degree program: Advanced Materials Science

submitted to

Graz University of Technology

Univ.-Prof. Mag.rer.nat. Dr.rer.nat. **Bergmann**, Alexander

Institute of Electronic Sensor Systems

Graz, July, 2019

EIDESSTATTLICHE ERKLÄRUNG
AFFIDAVIT

Ich erkläre an Eides statt, dass ich die vorliegende Arbeit selbständig verfasst, andere als die angegebene Quellen/Hilfsmittel nicht benutzt, und die den benutzten Quellen wörtlich und inhaltlich entnommenen Stellen als solche kenntlich gemacht habe. Das in TUGRAZ-online hochgeladene Textdokument ist mit der vorliegenden Masterarbeit identisch.

I declare that I have authored this thesis independently, that I have not used other than the declared sources/resources and that I have explicitly indicated all materials which have been quoted either literally or by content from the sources used. The text document uploaded to TUGRAZonline is identical to the present master's thesis.

Datum/ Date	Unterschrift/ Signature

Abstract

Fuel cell (FC) technology offers zero-emission electricity generation and a great potential to reduce the environmental impact of fossil fuels. This work represents the first step of testing a new sensor principle based on the photoacoustic (PA) effect for potential FC applications in the automotive industry. Major requirements for the PA sensor are a low response time, measurement and distinction of the three phases of water representing vapor, liquid and ice water content (VWC, LWC and IWC). Three fiber coupled laser diodes (LDs) with a center wavelength of (1364, 1550 and 1940) nm were selected according to carefully analyzed strong absorption bands with minimal interference. The optical setup was designed on the basis of calculations and ray tracing simulations according to specific PA cell boundary conditions. Beam shape, transmission and efficiency were further optimized to achieve a well-coupled laser beam into the resonant PA cell.
N-BK7® windows mounted on both sides of the resonant cell show high transmission, high water, chemical and heat resistance in order to withstand the harsh FC environment. Integrated heat cartridges were used to prevent potential water precipitation and resulting scattering effects on the window surface. LD characteristics were recorded and transverse beam profiles were investigated for potential optimization of the optical system.

The first validation of the PA sensor system, consisting of the optical system, resonant PA cell, a humidifier and detection software, was successfully accomplished in humid environment, the most relevant phase for low temperature PEMFC applications. Further PA signal amplification was achieved by LD wavelength tuning in agreement with the HITRAN atmospheric gas absorption data. The PA sensor, limited by the humidifier, displays a quadratic response to variations in the humidity conditions ((5 to 85) % rH). In addition, the results indicated a significantly faster response (τ_{63}) compared to the reference sensor. However, further research is required to fully understand the implications of the buffer gas (e.g molecular relaxation processes) on the PA signal.

Zusammenfassung

Die emissionsfreie Stromerzeugung einer Brennstoffzelle (FC) stellt ein großes Potential zur Reduzierung der Umweltbelastung durch Verbrennung fossiler Energieträger dar.
Diese Arbeit befasst sich mit der Analyse eines relativ neuen Sensorprinzips, basierend auf dem photoakustischen (PA) Effekt, für zukünftige FC Anwendungen in der Automobilindustrie. Der Fokus liegt auf der gleichzeitigen Bestimmung der Phase und Konzentration von Wasser (VWC, LWC und IWC) mit hoher Zeitauflösung, Sensitivität und Selektivität. Drei fasergekoppelte Laserdioden (LDs), mit einer mittleren Wellenlänge von (1364, 1550 und 1940) nm, wurden anhand sorgfältiger Analyse der Absorptionsbanden von Wasser ausgesucht. Der optische Aufbau wurde mittels geometrischer Berechnungen und Raytracing Simulationen unter Berücksichtigung von spezifischen PA Resonator Randbedingungen entworfen. Optimierungsprozesse der Strahlform, Kollimation und Transmission ermöglichten eine effiziente Einkopplung in die PA Zelle. N-BK7® Fenster, die auf beiden Seiten der Resonatorzelle befestigt wurden, weisen eine hohe Transmission, Wasser-, Chemikalien- und Hitzebeständigkeit auf, um den aggressiven Bedingungen standzuhalten. Integrierte Heizkartuschen dienen zur Beseitigung von potentiellen Wassertropfen und damit verbundenen Streueffekten auf der Fensteroberfläche. Ergänzend wurden LD Charakteristiken als auch Strahlprofile aufgezeichnet und analysiert.

Die erste Validierung des PA Sensorsystems (optischer Aufbau, PA Zelle, Befeuchter und Detektionssoftware) wurde erfolgreich in feuchter Atmosphäre, der wichtigsten Phase für Niedrigtemperatur PEMFC Anwendungen, untersucht. Anhand von HITRAN Absorptionsdaten wurde eine Verstärkung des PA Signals durch gezieltes LD Tuning erreicht. Der PA Sensor, limitiert durch den Befeuchter ((5 bis 85) % rH), zeigt eine quadratische Abhängigkeit von Feuchtigkeitsschwankungen und verspricht eine deutlich schnellere Reaktionszeit (τ_{63}) als der Referenzsensor. Die Auswirkung des Puffergases (z.B. molekulare Relaxationsprozesse) auf das PA Signal bedarf jedoch weiterer Untersuchungen.

Acknowledgement

Foremost, I would like to express my deepest gratitude and appreciation to my supervisor Professor *Alexander Bergmann*, head of the Institute of Electronic Sensor Systems, and my co-supervisor Professor *Anna Maria Coclite*, Institute of Solid State Physics, for their professional guidance, patience, motivation and constructive recommendations for this project. Without their endorsement, financial support and laboratory infrastructure in collaboration with *AVL List GmbH*, this project would not have been possible.

Besides my supervisors, I am particular grateful to *Christoph Kügele* for the extensive assistance, encouragement and expertise on PEMFC technology. My sincere thanks also goes to *Benjamin Lang* for the excellent teamwork concerning the PA measurement setup, in-depth discussions and support throughout the whole project.

Last but by no means least, I want to thank my family, who experienced all ups and downs of my research, for their continuous support and always believing in me. They are the most important people in my life and I dedicate this thesis to them.

Table of Contents

List of Figures

List of Tables

Terms

$\mathbf{CH_3OH}$	Chemical formula of methanol
$\mathbf{CH_4}$	Chemical formula of methane
$\mathbf{CO_2}$	Chemical formula of carbon dioxide
$\mathbf{CO_3^{2-}}$	Chemical formula of carbonate ion
CO	Chemical formula of carbon oxide
$\mathbf{CaF_2}$	Chemical formula of calcium fluoride
Cr	Symbol of the chemical element chromium
Cu	Symbol of the chemical element copper
C	Symbol of the chemical element carbon
Fe	Symbol of the chemical element iron
$\mathbf{H_2O}$	Chemical formula of water
$\mathbf{H_2}$	Chemical formula of diatomic hydrogen gas
$\mathbf{H_3O^+}$	Chemical formula of hydronium
$\mathbf{H^+}$	Chemical formula of the cationic form of atomic hydrogen
In	Symbol of the chemical element indium
$\mathbf{MgF_2}$	Chemical formula of magnesium fluoride
$\mathbf{N_2O}$	Chemical formula of nitrious oxide
$\mathbf{N_2}$	Chemical formula of diatomic nitrogen gas
$\mathbf{NO_2}$	Chemical formula of nitrogen dioxide

O_2	Chemical formula of diatomic oxygen gas
O_3	Chemical formula of ozone
OH^-	Chemical formula of hydroxide
O^{2-}	Chemical formula of the dianion of oxygen
Pt	Symbol of the chemical element platinum
$SO_3{}^-H^+$	Chemical formula of sulfonic acid functional groups
Sn	Symbol of the chemical element tin
ANAC	Operand for angular aberration radial direction with respect to the centroid
B270	Optical crown glass
E-V,R,T	Relaxation by electronic-vibration, rotation, translation energy transfer
HITRAN	High-resolution transmission molecular absorption database
I-V-P	Current-voltage-power
IWC	Ice water content The measure of the mass of water in solid state in unit volume of atmospheric air (g/m^3).
LWC	Liquid water content The measure of the mass of water in liquid state in unit volume of atmospheric air (g/m^3).
N-BK7®	RoHS-compliant borosilicate crown glass
NASA	National aeronautics and space administration
NPAR	Operand for non-sequential object parameter modification
OPLT	Operand for less than target value
R-T	Relaxation by rotation-translation energy transfer
RANG	Operand for ray angle in radians with respect to local z-axis
REAX	Operand for real ray x-coordinate

REAY Operand for real ray y-coordinate

rH Relative humidity
The ratio of the partial pressure p of water vapor in atmospheric air, over the equilibrium vapor pressure p_s of water at temperature T.

TWC Total water content
The measure of the total mass of water (liquid, gaseous and solid state) in unit volume of atmospheric air (g/m^3).

V-R,T Relaxation by vibration-rotation, translation energy transfer

V-V Relaxation by vibration-vibration energy transfer

VIS The part of the electromagnetic spectrum that is visible to the human eye.

VWC Vapor water content
The measure of the mass of water in gaseous state in unit volume of atmospheric air (g/m^3).

WAVE Operand for wavelength

WLWT Operand for wavelength weight

Abbreviations

1D	One-dimensional
2D	Two-dimensional
3D	Three-dimensional
ACL	Aspheric condenser lens
AFC	Alkaline fuel cell
AM	Arithmetic mean
AOI	Angle of incidence
AR	Anti-reflection
BFL	Back focal length
CAD	Computer-aided-design
CCD	Charge-coupled device
CF	Configuration
CIs	Confidence intervals
CT	Center thickness
DFB	Distributed feedback
DI	Deionized
FC	Fuel cell
FCEVs	Fuel cell electric vehicles
FL	Focal length

FP	Fabry-Pérot
FPGA	Field-programmable gate array
GDL	Gas diffusion layer
GIA	Geometric image analysis
GM	Global maximum
GUI	Graphical user interface
HFR	High frequency resistance
HHL	High heat load
HT	High temperature
IR	Infrared
ITO	Indium tin oxide
KEM	Knife-edge method
LD	Laser diode
LDE	Lens data editor
LM	Local maximum
LT	Low temperature
MCE	Multi-configuration editor
MCFC	Molten carbonate fuel cell
MEA	Membrane electrode assembly
MFC	Mass flow controller
MFE	Merit function editor
MIR	Mid-infrared
MM	Multi-mode
MSE	Mean square error
NA	Numerical aperture
NIR	Near-infrared

NSC	Non-sequential component
NSCE	Non-sequential component editor
NSQ	Non-sequential
OLED	Organic light emitting diode
PA	Photoacoustic
PAFC	Phosphoric acid fuel cell
PAS	Photoacoustic spectroscopy
PEMFC	Polymer electrolyte membrane fuel cell
ppbv	Parts per billion by volume
PTFE	Polytetrafluoroethylene
RMS	Root mean square
SCRs	Short concentric resonators
SD	Standard deviation
SE	System explorer
SM	Single-mode
SOFC	Solid-oxide fuel cell
SQ	Sequential
SSM	Scanning slit method
TEC	Thermoelectric cooler
TEM	Transverse electromagnetic

CHAPTER 1

Introduction

1.1 The Essence of Water

The water molecule H_2O, existing in one of the three phases (liquid, solid and gaseous), is fundamental for the development of life and climate on planet earth [51, 68, 118]. In the context of climate change, the vapor phase is seen as the most dominant factor for the global greenhouse effect [25, 93, 103] and provides direct feedback to the concentration of greenhouse gases [102]. Water appears to be the most significant molecule involved in the solar energy absorption and heat storage process. This behavior is linked to strong absorption of electromagnetic radiation in the infrared (IR) region as a result of transitions between vibrational-rotational energy levels [118]. The presence of water in different phases and concentrations plays a central role in a variety of industrial, commercial and meteorological applications. Particularly noteworthy for this work are the aviation industry to prevent the icing of blades and turbines [48], the climatic wind tunnels to investigate the effects of various environmental conditions on components and the automotive industry to optimize and control the water balance of a FC [42, 80, 108, 120].
The introduction of spectroscopic methods (e.g. photoacoustic spectroscopy (PAS)) for the simultaneous determination of phase and concentration could have a major impact on the water balance analysis of the entire FC. An enhancement of the water management may provide an increased life time, durability, performance and competitiveness in the industry. The state-of-the-art measurement techniques for the determination of the LWC, IWC and VWC are presented in the next paragraph.

Vapor Water Content (VWC)

The most widely employed techniques for the determination of the VWC are the **capacitive humidity sensor** and the **resistive humidity sensor**. The centerpiece of the capacitive humidity sensor is a sandwich structure, described by a thin film of polymer or metal oxide embedded between two conductive electrodes deposited on the substrate. The thin film either absorbs or releases water based on the relative humidity (rH) of the environment, which implies an almost proportional change in the dielectric properties of the thin film and thus the capacitance of the sensor [29, 90, 114]. Typical uncertainty and lowest response time τ_{63} are about $\pm$ (2 to 3) % rH and 8 s [97, 114].
Resistive humidity sensors detect the change in electrical impedance of a hygroscopic medium (conductive polymer, salt, etc.), which typically displays an inverse exponential relationship to humidity. The sensor material absorbs the water based on the ambient rH which implies the dissociation of ionic functional groups, leading to an increase in electrical conductivity. In contrast to capacitive sensors, the response time ranges from (10 to 30) s and the uncertainty is about (2 to 5) % rH [90]. Other common techniques for the determination of VWC are the quartz crystal micro balance, the surface wave sensor and the electrolytic sensor [47, 77, 84].

Liquid and Ice Water Content (LWC, IWC)

A variety of techniques, such as the **blade method**, the **rotating cylinder method** and the **hot wire principle** are globally recognized for the determination of the LWC/IWC in icing wind tunnels due to the extensive research and NASA validation data [48].
The blade method and the rotating cylinder method are based on the accumulation of ice over a certain period of time. Under controlled conditions (e.g. a water injected nozzle with a homogeneous droplet distribution) the obtained ice thickness allows a good estimate of the LWC [48]. Major disadvantages are the loss of temporal resolution, difficult phase discrimination due to the fact that ice, liquid and vapor can contribute to the final ice thickness and only validated results for a constant temperature of $-18\,^{\circ}\mathrm{C}$.
Several LWC measuring systems are based on the hot wire principle, which relies on the determination of the energy required to evaporate liquid droplets while maintaining a constant wire temperature. Additional heating elements with notches enable the determination of the total water content (TWC) and thus the calculation of the IWC. Examples for LWC/TWC hot wire measurement systems are the CSIRO King Probe, Nevzorov Sonde, the T-probe and SAE-WCM 2000 [48, 56, 58, 95].

1.2 Fuel Cell

In general, the FC represents an electrochemical cell (galvanic element), converting chemical energy of continuously supplied reactants directly into electrical energy. Five major FC types are categorized by their electrolyte, namely phosphoric acid fuel cell (PAFC), polymer electrolyte membrane fuel cell (PEMFC), alkaline fuel cell (AFC), molten carbonate fuel cell (MCFC) and solid-oxide fuel cell (SOFC) [4, 65, 82]. Table 1 displays the key FC specifications for each type.

Table 1: FC types: Overview of the most relevant FC specifications [82].

	PEMFC	PAFC	AFC	MCFC	SOFC
Electrolyte	Polymer membrane	Liquid H_3PO_4 (immobilized)	Liquid KOH (immobilized)	Molten carbonate	Ceramic
Charge carrier	H^+	H^+	OH^-	${CO_3}^{2-}$	O^{2-}
Operating temp.	(60 to 250) °C	200 °C	(60 to 220) °C	650 °C	(600 to 1000) °C
Catalyst	Platinum	Platinum	Platinum	Nickel	Perovskites
Cell components	Carbon based	Carbon based	Carbon based	Stainless based	Ceramic based
Fuel compatibility	H_2, CH_3OH	H_2	H_2	H_2, CH_4	H_2, CH_4, CO

Each FC type is based on the same underlying electrochemical principles but differs in terms of operating temperature range, fuel tolerance, performance characteristics and incorporated materials [65, 82]. FC technology offers attractive properties such as high efficiency, zero emission, modularity, simplicity and longevity compared to conventional energy conversion technologies. In recent years PEMFC has proven to be the main contributor to automotive applications due to their low operating temperature, high power and energy density, fast-start and on–off cycling characteristics [4, 11, 82]. According to the operating temperature, the PEMFC is categorized in a low temperature (LT) and high temperature (HT) model, (60 to 80) °C and (120 to 250) °C respectively.

1.2.1 Polymer Electrolyte Membrane Fuel Cell

The centerpiece of a PEMFC is a proton-conducting (H^+) polymer electrolyte membrane, usually a perfluorinated sulfonic acid polymer [4, 82]. The membrane is fixed between two porous, electrically conductive electrodes, typically fabricated from carbon fiber cloth or carbon fiber paper with an additional thin catalyst layer (e.g carbon supported platinum (Pt/C) nanoparticles) on either side of the membrane electrode interface [65, 82].

This multilayer compound is known as the membrane electrode assembly (MEA). In order to maximize the catalytic activity, the water removal from reaction sites, the gas diffusion into catalyst layer and the electrical conductivity, the MEA is typically fabricated using a dual-layer approach [4, 65, 82]. The highly active catalyst layer (Pt/C) is deposited directly onto both sides of the polymer electrolyte membrane, followed by the application of the thick porous, electrically conductive electrode layers, often referred to as the gas diffusion layer (GDL), on both sides of the membrane, as shown in Figure 1a. Other MEA fabrication methods are based on the direct deposition of the catalyst on the GDL [65].

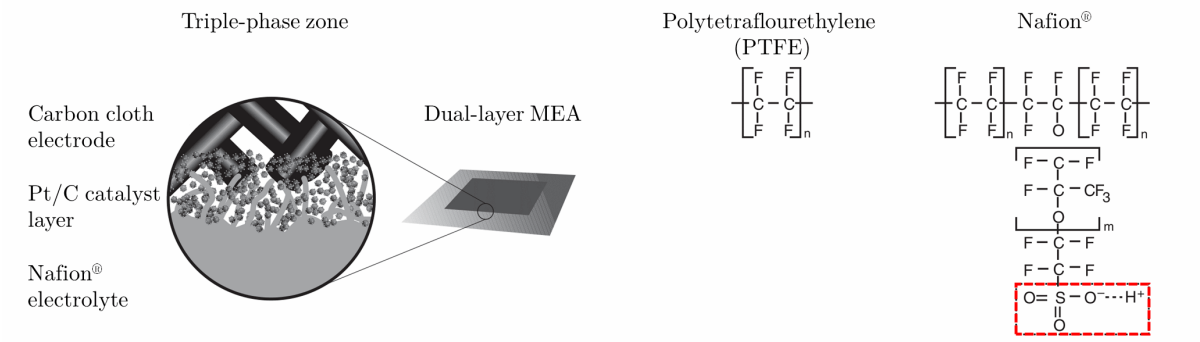

(a) MEA microstructure. **(b)** Chemical structure of Nafion®.

Figure 1: PEMFC: (a) MEA dual-layer fabrication approach. Detailed illustration of the final microstructure, highlighting the triple-phase zones at the reaction sites. (b) Chemical structure of Nafion® with the mechanically stable PTFE backbone and side chains with $SO_3^-H^+$ functional groups for the ionic conductivity. Figures reprinted from reference [82].

The electrochemical half reactions of a hydrogen-oxygen (H_2-O_2) PEMFC occur simultaneously at the surface of the catalyst sites at the interface between the electrode and the polymer electrolyte membrane [4]. These reaction sites, often called triple-phase zones, represent the regions where the electrolyte, electrode and gas phase are all in contact [4, 82]. At the anode side, the H_2 oxidation reaction occurs whereas at the cathode side the O_2 reduction reaction takes place.

$$\text{Anode:} \qquad \mathrm{H_2} \longrightarrow 2\mathrm{H^+} + 2e^- \tag{1.1}$$

$$\text{Cathode:} \qquad \frac{1}{2}\mathrm{O_2} + 2\mathrm{H^+} + 2e^- \longrightarrow \mathrm{H_2O} \tag{1.2}$$

$$\text{Overall:} \qquad \mathrm{H_2}(g) + \frac{1}{2}\mathrm{O_2}(g) \longrightarrow \mathrm{H_2O}(l) \tag{1.3}$$

The net result of the electrochemical reactions at the anode (H_2 supply) and cathode (O_2 supply) side is a direct electrical current through an external circuit, the formation of water at the anode side and heat [4]. It is apparent that both half reactions rely predominantly on the H^+ conductivity of the electrolyte membrane, which strongly depends on its humidification. Figure 2a illustrates a simplified scheme of an H_2-O_2 LT-PEMFC. A single cell generates approximately 1 V_{OC}. In multicell configurations in series, commonly known as FC stacks, voltages in the order of several 100 V are obtained. The physical/electrical connection in a FC stack is obtained by using bipolar plates, which serve as the anode in one cell and the cathode in the adjacent cell and provide pathways for the flow of reactant gases [4, 65, 82].

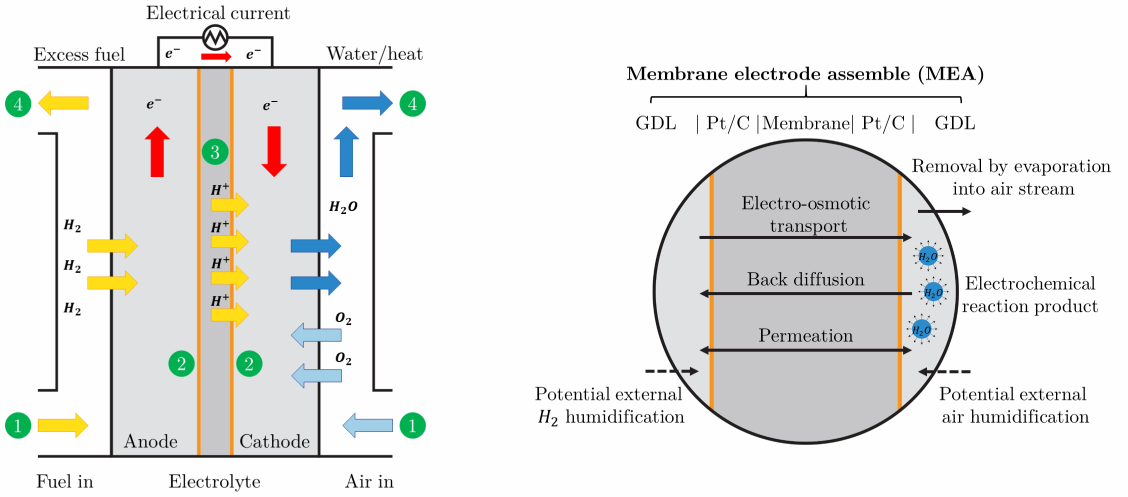

(a) Fundamental operation of the PEMFC.

(b) Water transport mechanisms.

Figure 2: PEMFC: (a) Scheme of major steps in electrochemical generation of electricity: 1) Reactant gas delivery into FC. 2) Electrochemical half reaction on both electrodes at the triple-phase zones. 3) H^+ transport through the membrane and e^- conduction through external circuit. 4) Product (water and heat) removal from the FC [82]. (b) Overview of crucial water transport mechanisms to, within, and from the electrolyte membrane.

The most popular and globally recognized electrolyte for PEMFC applications is per-sulfonated polytetrafluoroethylene (PTFE), better known as Nafion® (*Dupont*). It exhibits extraordinary high H^+ conductivity, mechanical and chemical stability and impermeability of the reaction gases [4, 82]. Its chemical structure consists of a PTFE backbone, more commonly known as Teflon, for mechanical strength and stability, and side chains with sulfonic acid ($SO_3^-H^+$) functional groups offering charged sites for the H^+ transport [82]. The ionic nature of the $SO_3^-H^+$ group leads to cluster formation of the ends of the side chains, creating hydrophylic regions within the membrane [4].

In the presence of water, the H^+ of the functional groups form hydronium complexes (H_3O^+) and separate from the sulfonic acid side chains [82]. As long as the membrane holds a significant amount of water, the H_3O^+ ions can move in the aqueous phase [105]. In fact, the actual water content across the membrane is heavily affected by water transport mechanisms during FC operations [4, 82, 105], as seen in Figure 2b. Water molecules are dragged from the anode to the cathode by the H^+ transport mechanism, referred to as electro-osmotic drag. The electrochemical water production and the electro-osmotic drag cause accumulation of water at the cathode side [11]. Due to this concentration gradient across the membrane, water molecules diffuse back to the anode. In addition, product water is removed from the cathode by the undersaturated reactant gas stream.

Water Management

In case the self-humidification processes within the FC are not enough to maintain extraordinary conductivity (fully hydrated membrane [121, 122]), preconditioning (e.g humidification) of the input reactant gases is applied. Hence, the humidity conditions within the PEMFC system represent the key parameter for controlling the water content in the membrane for optimum FC performance [4, 82]. Depending on the FC operation conditions, a minimal variation of the rH can cause damaging effects.

rH↑: High rH triggers the formation of water droplets (flooding process), which leads to the blockage of supply channels and GDLs and consequently to H_2 and air (O_2) starvation.

rH↓: Dry conditions result in a high electric membrane resistance against H^+ transport which is accompanied by a decrease of H^+ conductivity through the membrane.

rH↑↓: Rapid fluctuations in rH cause expansion and contraction of the sensitive membrane, which can lead to potential pinholes and defects ("Knallgas" reaction).

Therefore, the water balance is fundamental to maximize the H^+ conductivity and to prevent dehydration and flooding, mechanical, thermal and chemical degradation effects of the membrane and GDL [4, 16, 82] and detrimental effects on the FC performance and lifetime [18, 57, 91, 105, 106]. In order to optimize the water management of the PEMFC system, intrinsic parameters of the membrane such as water transport mechanism, conductivity and thickness and external variables including cell current, temperature and humidification of reactant gases need to be considered [20, 82].

Challenges in Automotive Applications

In contrast to stationary power application, PEMFC systems in automotive applications are exposed to less ideal operation conditions including road load variability (power demand), start-stop cycles, temperature fluctuations [4, 20, 82] and extreme weather conditions [82]. Hence, the preservation of a proper water balance throughout the entire FC is a major challenge in the automotive industry. A change in the FC operation point is a dynamic process in the range of ms, resulting in a different water production, temperature T, pressure p and mass flow $\dot{m}$. All these parameters directly affect the humidity conditions within a PEMFC and occur on a different time and length scale. The relevant time constants for these transient processes are ΔT in O(min), Δp and $\Delta \dot{m}$ in O(s), water production in O(ms), where O stands for the order of magnitude [88].

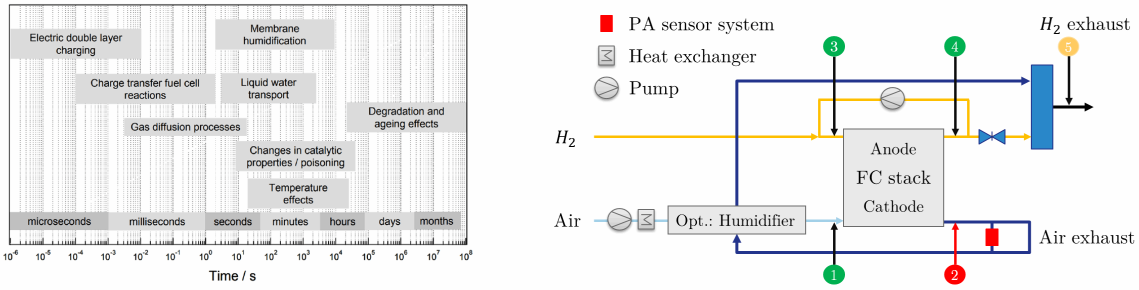

(a) **(b)**

Figure 3: PEMFC: (a) Overview of relevant time constants for dynamic processes. Figure reprinted from reference [81]. (b) Simplified scheme of a PEMFC system for the potential implementation of the PA sensor system at the exhaust tract, combined with a capacitive humidity sensor for optimal water management.

State-of-the-Art

In order to regulate the water management for the optimal FC operating point, a dynamic transient measurement of the humidity conditions at at least four points within the PEMFC system is necessary, as illustrated in Figure 3b. The two state-of-the-art approaches in the automotive industry to control the water balance are:

1. Simulation

A model driven soft sensor relies on the fundamental equations underlying the PEMFC process, namely mass-preservation principles, water balances, energy balances, thermodynamics and electrochemical reaction kinetics [36, 67]. Due to the complexity of the FC process, the simplified mathematical models may not provide satisfactory predictions of the

humidity conditions at the exhaust tract. Nonetheless, model- or map-based simulations are widely implemented in fuel cell electric vehicles (FCEVs).

2. Measurement

The industry standard for humidity (VWC) measurements in PEMFC test beds is a capacitive humidity sensor, e.g. HMT330-7 manufactured by *Vaisala*. As previously mentioned, the capacitive sensor provides a relative measurement of the humidity conditions. Major disadvantages of the application in a FC are the relatively high response time to a change in rH, in the range of seconds [115], and potential sensor blackouts caused by liquid water droplets, leading to an average recovery time of about 60 s [101]. Compared to the time scale of the dynamic processes in a FC, potential critical operation conditions may be detected with a time delay promoting degradation effects and performance loss. The concept of sensor shielding to prevent the liquid water impact was investigated in great depth by *Wolfgang Smode*, in his master's thesis [101]. However, in standard operating conditions, VWC and LWC, the main contributors to the TWC, need to be considered for a comprehensive water balance analysis of the PEMFC system.

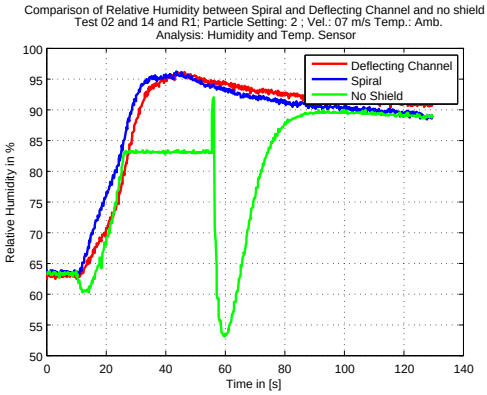

Figure 4: Capacitive humidity sensor: Comparison of rH between two shielding concepts and no shielding. The average recovery time due to water droplet impact is approximately 60 s without using a shield.[1]

1.3 Motivation

The simultaneous determination of phase and concentration of water with high time resolution, sensitivity and selectivity for industrial process monitoring and calibration/ certification, e.g. in the automotive and aviation industries, is currently limited by the sensitivity and response time of state-of-the-art sensor techniques. Based on the potential of innovative spectroscopic methods (e.g. PAS) for determining the concentration of water content in gases [14, 28, 59, 64], the step to optical methods lead to shorter response times, high selectivity, high sensitivity, and potential distinction of LWC, IWC and VWC.

[1] Used with permission of *Wolfgang Smode*, *AVL List GmbH*, (June, 2017) [101].

This work focuses on the exploration of a PA sensor system for the determination of phase and concentration of water for future potential implementation in LT-PEMFC water balance analysis at the exhaust tract, as illustrated in Figure 3b. The long-term goal is to improve dynamic process monitoring of the humidity condition throughout the FC. The short response time, high sensitivity and ability to determine the TWC (= LWC+VWC) allow a fast adjustment of the operating conditions to dynamic jumps in the power demand. In combination with the integration of capacitive humidity sensors at the green points in Figure 3b, a significant enhancement of the water balance analysis of a LT-PEMFC system can be achieved. Additional on-line high frequency resistance (HFR) tests offer further knowledge of the actual water content within the membrane [22]. All together would have a significantly beneficial effect on the FC durability, performance and lifetime [4]. The fundamental aspects of the PAS are explained in more detail in Section 2.2.

1.3.1 Objective

Based on the concept of the photoacoustic effect, the objective of this master's thesis is:

"*Design and validation of a PA sensor system for the determination of phase and concentration of water in the exhaust tract of the LT-PEMFC*"

In the same context, the on-going dissertation of *Benjamin Lang* focuses on the design, modeling and validation of a PA sensor system for water content and phase measurement in air flows, specifically for the application in icing wind tunnels for calibration/certification purposes. Both projects are based on the identical sensor principle for the determination of phase and concentration of water for applications under similar harsh environments. Due to the overlapping conditions and objectives, the PA sensor concept, data acquisition and signal processing were developed and provided by *Benjamin Lang*.
On the basis of the PA resonator cell, the project can be separated into four major parts:

1. Design and optimization of an optical setup for water phase discrimination
2. Component and material selection
3. Concept and realization of PA measurement setup
4. Validation test (proof of concept) in humid environment.

CHAPTER 2

Methodology and Concept

2.1 Absorption Spectroscopy

Optical spectroscopy is a powerful tool for continuous, highly sensitive and selective detection of multiple gaseous species. Mid-infrared (MIR) and IR range mark the most appealing spectral region to perform laser spectroscopy due strong absorption bands of many gas species and widespread availability of high quality and affordable cost sources, detectors and other equipment [71]. The absorption of radiation marks the most crucial interaction processes between electromagnetic radiation and matter, alongside Raman scattering and fluorescence emission [10]. Specific absorption characteristics, caused by the unique atomic and molecular nature of each molecule, allow the identification of the gaseous compounds and the determination of their concentrations. The essential theory of absorption spectroscopy is expressed by the Beer-Lambert law [17, 24, 45].

$$I(\widetilde{\nu}) = I_0 e^{-\alpha(\widetilde{\nu})l} \tag{2.1}$$

Equation (2.1) describes the exponential attenuation of the incident light intensity I_0 through an absorbing material. The exponential decay depends on the material's absorption coefficient $\alpha(\widetilde{\nu})$ and path length l. The characteristic wavenumber $\widetilde{\nu}$ dependency is given by

$$\widetilde{\nu} = \frac{1}{\lambda} = \frac{\nu}{c} = \frac{E_m - E_n}{hc} \tag{2.2}$$

which derives directly from quantum theory [17, 24]. The parameters ν, c, h, E_n and E_m represent the frequency of the incident light wave, the speed of light in vacuum, the Planck's constant, the lower and upper energy level, respectively. In addition, the absorption coefficient is linked to the cross section $\sigma(\widetilde{\nu})$ of the molecules by

$$\alpha(\widetilde{\nu}) = N\sigma(\widetilde{\nu}) = -\frac{1}{l}\ln\left[\frac{I(\widetilde{\nu})}{I_0}\right] \tag{2.3}$$

where N represents the number density in molec/cm^3 [17, 24]. As highlighted in literature [10, 45], the cross section can be expressed by the product of the line intensity S and a normalized line shape function $g(\widetilde{\nu})$ describing the broadening mechanism, measured in units $[S]$ =cm^{-1}/(molec $\cdot$ cm^{-2}) and $[g(\widetilde{\nu})]$ =cm. The determination of the absorption coefficient $\alpha(\widetilde{\nu})$ allows the calculation of the material's concentration C by

$$C = \frac{N}{N_{tot}} = -\frac{1}{lSg(\widetilde{\nu})}\ln\left[\frac{I(\widetilde{\nu})}{I_0}\right]\frac{1}{N_{tot}} \tag{2.4}$$

with $N_{tot} = N_L\frac{296}{T}p_0$ representing the total number density of molecules at temperature T and pressure p_0 . The Loschmidt number N_L is 2.479×10^{19} molec/cm^3 atm^{-1} at 296 K and 101 325 Pa. The line intensity of an absorption transition depends on the population density of the molecules in the lower energy level, given by the Boltzmann distribution, and the probability of the corresponding molecular transition expressed by the Einstein coefficient B_{nm} between the lower state n and the upper state m [10, 17, 24]. Additional important parameters to characterize the absorption line are the line shape and width, primarily influenced by three broadening mechanisms [8, 10, 17, 24, 45].

Natural line broadening: The lower limit of the absorption line width is defined by the finite lifetime of energy levels which manifests in a broadening ΔE of the energy level given by the uncertainty principle [44]. Due to the identical behavior of each atom or molecule, the line broadening mechanism is homogeneous and results in a Lorentzian line function $g(\widetilde{\nu})$.

$$\Delta E\Delta\tau = \frac{h}{2\pi} \tag{2.5}$$

Doppler broadening: This broadening effect (Doppler shift) is caused by the thermal motion of absorbing gas particles with respect to the propagation direction of the incident light source. Particle velocities follow the Maxwell distribution resulting in an inhomogeneous broadening, characterized by a Gaussian line function $g(\widetilde{\nu})$.

Collisional broadening: The collision between absorbing gas atoms or molecules imply a transfer of energy and an effective reduction of the lifetime of the excited state. The change in $\Delta\tau$ yields a broadening of ΔE (see Equation (2.5)). Identical to natural broadening, the process is homogeneous and follows a Lorentzian line function $g(\widetilde{\nu})$.

In general, natural line broadening is completely concealed by Doppler and Collisional broadening [24]. At high temperatures and pressures, Doppler and collisional broadening are significant and need to be considered. The combination of the individual line shapes yields to a Voigt line function $g(\widetilde{\nu})$, representing the convolution of the Lorentzian and Gaussian distribution [24, 45].

2.1.1 Water Phase Discrimination

As previously mentioned in Section 1.1, the water molecule exhibits strong absorption bands in the IR range as a result of characteristic transitions between the vibrational-rotational energy levels, closely related to its physical properties and state of matter [118]. Various studies have assessed the absorption characteristics of the individual water phases over a wide wavelength range [37, 60, 96, 117].

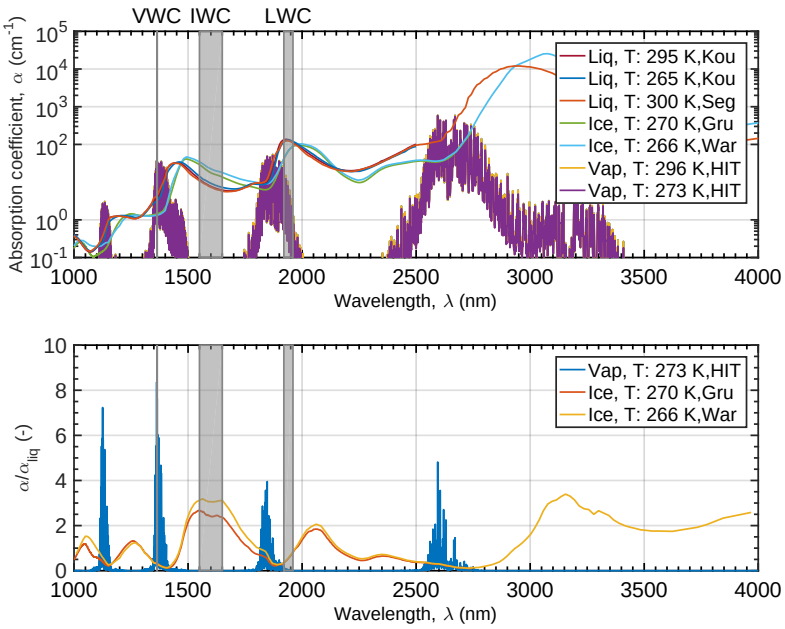

Figure 5: Water absorption spectra: Absorption coefficient for vapor, liquid and ice phase over wavelength. Additional absorption coefficient ratios for the determination of the lowest phase inference.[2]

[2] Grundy and Schmitt [37], Kou et al. [60], Segelstein [96], Warren [117], HITRAN database (2012) [34].

Together with the HITRAN database [34], a complete picture of the water absorption behavior of each individual phase, namely vapor, liquid and ice, was obtained. Phase discrimination relies on the wavelength dependent interaction between electromagnetic radiation and matter. In order to determine the highest ratio and lowest interference between each phase, the absorption coefficient ratios α/α_{liq} were investigated in more details, as seen in Figure 5. It is apparent to see that the vapor phase shows the highest ratio single line for small concentrations at 1364.69 nm. Furthermore, the ice phase displays minimal interference and a relatively high absorption coefficient ratio within (1550 to 1650) nm. The more challenging task is the detection of the liquid phase, due to the low absorption coefficient ratio and the simultaneous presence of multiple absorption bands of different phases. Based on Figure 5 and associated literature, the following three wavelengths/wavelength regions were selected for water phase discrimination:

VWC: 1364.69 nm **IWC:** (1550 to 1650) nm **LWC:** (1920 to 1960) nm

2.1.2 Laser Diode Selection

The spectral properties of an LD are essential for the PA phase discrimination in order to minimize the influence of interference of other species in spectral vicinity of the target absorption line. Based on the absorption characteristics of the water molecule, three fiber-coupled LDs with a central wavelength of approximately (1364, 1550 and 1940) nm were considered more carefully. Typically, the lasing wavelength can be optimized over a small range by a variation of the temperature and the injected drive current [104]. By varying the temperature, a change in the band gap energy of the semiconductor material is induced leading to a wavelength shift of the LD ($T \uparrow \lambda \uparrow; T \downarrow \lambda \downarrow$). In case of distributed feedback (DFB)-LDs, temperature variation affects the effective refractive index of the one-dimensional (1D) interference grating (Bragg scattering) which is incorporated in the active layer [12]. The variation of the effective refractive index n_{eff} implies a shift in the lasing wavelength λ, given by the expression of the Bragg wavelength. Additional information can be seen in Sections 3.6.2 and 4.4.1.

Table 2 shows important LD specifications such as the fiber core diameter $\varnothing$, the numerical aperture (NA), the peak wavelength λ_p, the threshold current I_{th}, the operating temperature T_{op} and power P_{op} for each LD according to the specification sheets provided by the manufacturers *NEL*, *FLC* and *OECA*. An overview of the corresponding LD mounts can be found in Table 25.

Table 2: Laser diode specifications[3].

	LD 1	LD 2	LD 3
Company	*NEL*	*FLC*	*OECA*
Modell	NLK1E5GAAA	FLX-1550-840M-FC200	LQ5-1940-200/HHL-FSMA
Laser class	3B	4	3B
Technology	DFB	Fabry-Pérot (FP)	FP
Fiber	Single-mode (SM)	Multi-mode (MM)	MM
Connector	FC/PC	FC-SMA	FSMA
$\varnothing$ (µm)	9.0	200	200
NA	0.12	0.22	0.22
λ_p (nm)	1364.69 ± 1.00	1550 ± 20	1940 ± 10
I_{th} (mW)	7.0	443.98	350
T_{op} (°C)	25	25	25
P_{op} (W)	0.02	0.6	0.2

2.2 Photoacoustic Spectroscopy

In contrast to conventional absorption spectroscopy, the PAS represents an indirect measurement of the optical energy absorbed by the target gas atoms or molecules. It is based on the detection of the local transient heating induced by the molecular absorption of a non-stationary (modulated or pulsed) light beam at proper wavelength and subsequent non-radiative relaxation of the excited state. [2, 10, 62, 71, 99]. The induced periodical local thermal expansion results in the generation of an acoustic wave of the same frequency that can be detected by a sensitive microphone [30]. This process is known as the PA effect. Under certain conditions, the induced pressure variations are directly proportional to the number of excited molecules; hence the gas concentration can be derived. The PA effect (formally called optoacoustic effect) was discovered in 1880 by Bell [6]. He demonstrated that the interaction of a periodically interrupted light beam with a solid material produces an acoustic signal. In 1881, the work of Röntgen [89], Tyndall [113] and Preece [87] revealed the existence of the PA effect in liquids and gases. Furthermore, the resonant amplification of the PA signal amplitude was discovered by Bell [7]. The invention of the first LD, delivering high-power, monochromatic and collimated beams, highlights a major breakthrough for the PAS. The first implementation in a PA gas detection system was realized by Kerr and Atwood in 1968 [53].

[3] LD specifications: *NEL* (February, 2017); *FLC* (October, 2016); *OECA* (November, 2016).

The pioneering work of Kreuzer in 1971 [61] marks the starting point of PA trace gas analysis. Since then, the technological progress in the field of laser sources (MIR-CO,-CO_2 gas laser and near-infrared (NIR) diode laser), resonant cell configurations and high-sensitivity pressure detection systems (microphones and electronics) have been instrumental in pushing the PA detection limit into the parts per billion by volume (ppbv) concentration range [9, 13, 26, 38, 39, 52, 73, 76].

2.2.1 Photoacoustic Effect in Gases

In general, the PA effect can be divided into three major steps [2, 10, 62, 75]:

1. Heat release by relaxation of absorbed light energy through non-radiative deactivation by R-T, V-R,T and E-V,R,T processes.
2. Acoustic and thermal wave generation based on localized transient heating and expansion.
3. Detection of the acoustic signal in the resonant PA cell using a microphone.

A closer look at the individual steps of the PA effect is given in the next paragraph.

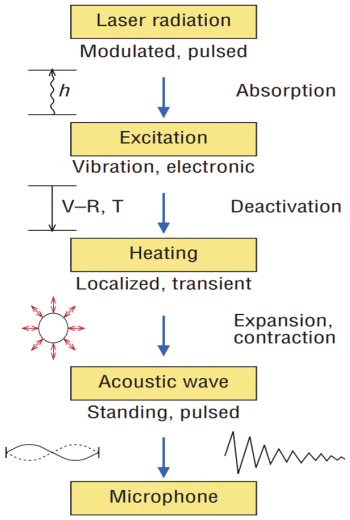

Figure 6: PA effect: Overview of the physical processes occurring after the optical excitation by a non-stationary light source. Figure reprinted from reference [76].

Heat Generation by Light Absorption

The molecular absorption of light by the material results in the excitation of internal energy levels (rotational, vibrational, electronic) and subsequent relaxation to the initial energy level through several processes, including radiation (spontaneous or stimulated emission), chemical reactions and non-radiative deactivation (collisional deactivation) [2, 71]. Radiative emissions are negligible for vibrational excitation in the IR due to the long life time τ_r compared to the time needed for a collisional deactivation τ_n in typical atmospheric conditions ($\tau_n \ll \tau_r$) so that τ can be approximated by τ_n [73]. Furthermore, chemical reactions do not play an important role due to the low incident optical energy [2, 46]. Hence, collisional deactivation is responsible for the complete conversion of the absorbed optical energy into translation (kinetic) energy of the surrounding gas molecules, which implies local heating and subsequent thermal expansion [74, 75]. For a simple two

level model of the absorption process, the heat production rate can be expressed by

$$H = N^{'} \frac{hc\Delta\widetilde{\nu}}{\tau_n} \tag{2.6}$$

showing a direct correlation to the number density of the excited energy level $N^{'}$, to the energy gap of the transition $\Delta\widetilde{\nu}$ and to the non-radiative energy level lifetime τ_n [71]. The two level system implies the relaxation processes into the initial energy level, hence the quantity $\Delta\widetilde{\nu}$ is considered to be equal to the laser frequency $\widetilde{\nu}_{LD}$ [71]. $N^{'}$ represents the time harmonic solution of the rate equation for the excited number density $N^{'}$ given by

$$\frac{dN^{'}}{dt} = \left(N - N^{'}\right)\sigma\Phi - N^{'}\sigma\Phi - \frac{N^{'}}{\tau} \tag{2.7}$$

with

$$\Phi = \Phi_0\left(1 + e^{i\omega t}\right) \qquad \text{and} \qquad \tau^{-1} = \tau_n^{-1} + \tau_r^{-1}. \tag{2.8}$$

The parameters Φ, σ, τ and ω display the complex modulated photon flux, the absorption cross section, the time constant of relaxation and the angular modulation frequency. The rate equation incorporates the absorption process, stimulated emission process and non-radiative relaxation of a simple two level excitation system. Considering the previously introduced approximation $\tau \cong \tau_n$, an average excitation rate of $\sigma\Phi$ ($N^{'} \ll N$) and the time dependent term of the photon flux Φ, the solution of Equation (2.7) is

$$N^{'} = \frac{N\sigma\Phi_0\tau}{\sqrt{1 + (\omega\tau)^2}} e^{-i(\omega t - \theta)}. \tag{2.9}$$

Taking into account that $\Delta\widetilde{\nu} \equiv \widetilde{\nu}_{LD}$ and $\tau \cong \tau_n$, the heat production rate in Equation (2.6) for a two level system becomes

$$H = N^{'} \frac{hc\widetilde{\nu}_{LD}}{\tau} = H_0 e^{i(\omega t - \theta)} \tag{2.10}$$

with

$$H_0 = \frac{N\sigma I_0}{\sqrt{1 + (\omega\tau)^2}} = \frac{\alpha I_0}{\sqrt{1 + (\omega\tau)^2}}. \tag{2.11}$$

The parameter θ, given by $\arctan(\omega\tau)$, considers the potential phase lag between the number density $N^{'}$ and the photon flux Φ [10, 71]. The obtained expression for the

deposited heat power density H in Equation (2.10) reveals a proportional relationship to the incident light intensity $I_0 = \Phi_0 hc\widetilde{\nu}_{LD}$, the absorption coefficient α and thus a direct dependence to the concentration C of the gas atoms or molecules [75], as seen in Equation (2.3). The time dependence of H, originating from the harmonic modulated photon flux given in Equation (2.8), represents the most important part of the fundamental equation of photoacoustics, as seen in Equation (2.10). For low modulation frequencies ω (in kHz range, $\omega\tau \ll 1$) and average excitation $\sigma\Phi$, the amplitude of the heat production rate can be simplified to

$$H_0 = N\sigma I_0 = \alpha I_0. \tag{2.12}$$

In these specific conditions, H is perfectly linear with the probed gas concentration, independent of the relaxation time and in phase with the optical modulated light intensity [71, 73]. The particular case of ($\omega\tau \gg 1$) due to long-lasting relaxation effects is discussed at the end of this section.

Acoustic Wave Generation

Acoustic and thermal wave generation can be theoretically addressed by the laws of fluid mechanics and thermodynamics. On the basis of the energy, momentum and mass conservation laws, given in the form of the heat diffusion, linearized Navier-Stokes and continuity equations, a linear wave equation for the sound pressure $p(\mathbf{r}, t)$ can be derived [2, 5, 27, 62, 75].

$$\nabla^2 p(\mathbf{r}, t) - \frac{1}{c_s^2}\frac{\partial^2 p(\mathbf{r}, t)}{\partial t^2} = -\frac{(\gamma - 1)}{c_s^2}\frac{\partial H(\mathbf{r}, t)}{\partial t} \tag{2.13}$$

The parameters c_s, γ and H are the velocity of sound, adiabatic coefficient of the gas and the absorbed heat density, respectively. Potential acoustic losses produced by heat conduction and viscosity are introduced in a further step as a perturbation of the loss-free solution of Equation (2.13) [10, 62]. The source term of Equation (2.13) is proportional to the heat power density H released in the material by non-radiative relaxation processes. The time evolution of the laser excitation and the relaxation dynamics determine the time dependency of the heat source [2, 75, 76]. The solution to the inhomogeneous wave equation is obtained by taking the time Fourier transform on both sides and expressing the acoustic pressure $p(\mathbf{r}, \omega)$ as an infinite series expansion of all normal modes $p_j(\mathbf{r}, \omega)$ of the homogeneous wave equation given by

$$p(\mathbf{r},\omega) = \sum_j A_j(\omega)\, p_j(\mathbf{r},\omega)\,. \tag{2.14}$$

All normal modes and their specific resonance frequency directly depend on the shape and dimensions of the resonant cavity [27, 62, 71]. The corresponding normal mode amplitude A_j is derived by multiplication of the complex conjugated $p_j^*(\mathbf{r},\omega)$ and subsequent integration over the cell volume V_c. The consideration of the orthogonality criterion between all normal mode solutions results in

$$A_j(w) = -\frac{i\omega}{\omega_j^2}\frac{(\gamma-1)}{V_c}\frac{\int p_j^*(\mathbf{r},\omega)\, H(\mathbf{r},\omega)\, dV}{1-\left(\frac{\omega}{\omega_j}\right)^2}. \tag{2.15}$$

The intergral in Equation (2.15) illustrates the coupling between the heat power density $H(\mathbf{r},\omega)$ and the normal mode $p_j(\mathbf{r},\omega)$ [62]. The light intensity $I_0(\mathbf{r},\omega)$ can be expressed by the total optical power P_0 and the normalized spatial distribution function $g(\mathbf{r})$ [10, 62]. Under the conditions in which Equation (2.12) is a good approximation, the heat production rate is

$$H(\mathbf{r},\omega) = \alpha P_0 g(\mathbf{r})\,. \tag{2.16}$$

In addition, potential losses are introduced as mode damping in form of the quality factor Q_j. It takes into account the ratio between the accumulated acoustic energy and the potential losses over one period, limiting the acoustic amplification of the PA measurement system [10, 27, 62]. Hence, Equation (2.15) becomes

$$A_j(w) = -\frac{i\omega}{\omega_j^2}\frac{(\gamma-1)}{V_c}\frac{\alpha P_0 L}{1-\left(\frac{\omega}{\omega_j}\right)^2-\frac{i\omega}{\omega_j Q_j}}\overbrace{\frac{1}{L}\int p_j^*(\mathbf{r},\omega)\, g(\mathbf{r})\, dV}^{I_j} \tag{2.17}$$

where I_j represents the spatial overlap of the incident laser beam and the pressure distribution of the j-th eigenmode of the resonant cell [10, 75]. The adjustment of the light path can lead to a suppression of undesired eigenresonances (I_j tends to 0) which may lead to a predominant excitation of a particular resonance [75]. In conclusion, the PA signal is proportional to the absorption coefficient α, length of interaction L and incident optical power P_0. Furthermore, it is inversely proportional to the cell volume V_c and modulation frequency ω [10, 76].

Detection of Acoustic Signal

In case of resonant operations, the modulation frequency is set to one of the eigenresonances of the PA cell ($\omega = \omega_j$) [2, 75]. The resulting sound pressure $p(\mathbf{r}, \omega)$ is obtained by combining Equations (2.14) and (2.17).

$$p(\mathbf{r}, \omega) = \sum_j -\frac{i\omega}{\omega_j^2} \frac{(\gamma - 1)}{V_c} \frac{\alpha P_0 L}{1 - \left(\frac{\omega}{\omega_j}\right)^2 - \frac{i\omega}{\omega_j Q_j}} I_j p_j(\mathbf{r}, \omega_j) \tag{2.18}$$

It is apparent from Equation (2.18), that not only the j-th but all eigenmodes of the resonant cell undergo a certain excitation. The amplitude of the considered resonance is amplified by the quality factor Q_j, whereas the amplitude of other distant resonances is damped by the quantity $\omega_j^2 - \omega_j^2$ [10, 27, 75]. A high quality factor ($Q_j > 50$) of the selected resonance combined with well separated eigenresonances of the PA cell leads to a much more efficient excitation of the particular resonance than the others. Hence, the contribution of all other resonances to the PA signal are insignificant and can be neglected. In this high Q-factor scenario, the series expansion of the acoustic pressure can be approximated by one single term, representing the resonance amplitude of the j-th eigenmode, obtained by setting $\omega = \omega_j$ in Equation (2.17) [2, 75].

$$A_j(\omega_j) = \frac{Q_j}{\omega_j} \frac{\alpha P_0 (\gamma - 1) L}{V_c} I_j \tag{2.19}$$

At resonance, the acoustic energy $E_j(\omega)$, proportional to $|A_j(\omega)|$, from many modulation cycles is accumulated in a standing acoustic wave and amplified by the quality factor Q_j [10, 62]. As mentioned before, the amplification of the PA signal is limited by the total losses of the resonant cell. The corresponding sound pressure $p(\mathbf{r}_M, \omega_j)$ for this resonant configuration at the microphone position r_M is obtained by combining Equations (2.14) and (2.19).

$$p(\mathbf{r}_M, \omega_j) = \underbrace{(\gamma - 1) \frac{Q_j}{\omega_j} \frac{L}{V_c} I_j p_j(\mathbf{r}_M, \omega_j)}_{C_j(\omega_j)} \alpha P_0 \tag{2.20}$$

All quantities in the pre-factor of αP_0 can be grouped and defined as the cell constant, expressing the sensitivity of the PA system at a particular resonance frequency [10, 75]. It takes into account the dimensions of the resonant cell, the frequency and the quality factor of the selected resonance, the microphone position, potential influence of the buffer gas and the spatial overlap integral of the laser beam and the pressure distribution.

The resulting PA signal amplitude for the resonant configuration becomes

$$S_{PA} = p\left(\mathbf{r}_M, \omega_j\right) = C_j\left(\omega_j\right) \alpha P_0. \tag{2.21}$$

It implies a linear dependence of the PA signal on the absorption coefficient α and laser power P_0 for low modulation frequencies ω and average excitation. Hence, the concentration of the target gas can be derived from the induced pressure variation [10, 27].

2.2.1.1 Influence of Molecular Relaxation Processes

In most cases, the condition $\omega\tau \ll 1$ is fulfilled and the obtained PA signal, Equation (2.21), is independent of the relaxation time and exhibits no phase shift. However, for specific molecules (e.g N_2, O_2, etc.) the assumption $\omega\tau \ll 1$ is no longer satisfied due to prolonged relaxation times compared to the period of the modulated light intensity. Taking into account Equation (2.11) and the probed gas concentration $C = N/N_{tot}$, the dependency of the PA signal on the relaxation time τ can be expressed as [10, 71, 73, 92]:

$$S_{PA} = \frac{C_j\left(\omega_j\right) \overbrace{C\sigma N_{tot}}^{\alpha} P_0}{\sqrt{1 + \left(\omega_j\tau\right)^2}} = \frac{C_j\left(\omega_j\right) \alpha P_0}{\sqrt{1 + \left(\omega_j\tau\right)^2}}. \tag{2.22}$$

In contrast to the instantaneous heat release, excess energy can be transferred by collision (V-V) to long lifetime excited states of the molecules in the vicinity. In fact, molecular relaxation does not depend only on the type of probed compound M, but also on the individual components M_i of the gas mixture. The global relaxation rate τ^{-1} can be expressed as the sum of the contribution from V-V relaxation processes of an excited state of a molecule M with the probed gas itself, indicated by τ_{M-M}^{-1}, and of all other components M_i, represented by $\tau_{M-M_i}^{-1}$ with respect to their concentrations C_i [10, 71, 92].

$$\tau^{-1} = C\tau_{M-M}^{-1} + \sum_{i}^{n} C_i \tau_{M-M_i}^{-1} \tag{2.23}$$

For slow relaxation processes, $\omega\tau \gg 1$, the PA signal experiences a phase shift ($\theta \neq 0$) with regard to the modulation signal, potential damping due to less efficient sample heating [73] and a parabolic dependency on the measured gas concentration C [71, 92]:

$$S_{PA} = \frac{C_j\left(\omega_j\right) \sigma N_{tot} P_0}{\omega_j} C\left(C\tau_{M-M}^{-1} + \tau_{oth}^{-1}\right). \tag{2.24}$$

2.3 Optics

2.3.1 Laser Beam Propagation

In general, laser beam propagation can be approximated by assuming an ideal Gaussian intensity profile ($M^2 = 1$), which corresponds to the theoretical transverse electromagnetic (TEM_{00}) Gaussian mode. Optical beams and laser resonators must consider diffraction and the wave nature of light. The paraxial Gaussian wave equation represents a differential approach for free-space wave propagation. It is an approximation of the Helmholtz equation which is derived from Maxwell's equations. In general, electromagnetic fields in free space are described by the Helmholtz equation

$$\left[\nabla^2 + k^2\right] \widetilde{E}(x, y, z) = 0. \tag{2.25}$$

$\widetilde{E}(x, y, z)$ represents the complex amplitude of a field distribution that is sinusoidal in time and $k = 2\pi/\lambda$ [98, 100]. For transverse modes the propagation direction is primarily along the z-axis. Hence the spatial dependence of the field shows an $exp(-jkz)$ variation with a spatial period of one wavelength λ in the z-direction. The concept of the paraxial Gaussian begins with the approximation of the Helmholtz equation by extracting the primary propagation factor out of $\widetilde{E}(x, y, z)$ as seen in

$$\widetilde{E}(x, y, z) \equiv \widetilde{u}(x, y, z)\, e^{-ikz}. \tag{2.26}$$

The complex scalar wave amplitude $\widetilde{u}(x, y, z)$ describes the transverse profile with its variation in propagation. Substitution of $\widetilde{E}(x, y, z)$ into the Helmholtz equation in rectangular coordinates yields the reduced equation

$$\frac{\partial^2 \widetilde{u}}{\partial x^2} + \frac{\partial^2 \widetilde{u}}{\partial y^2} + \frac{\partial^2 \widetilde{u}}{\partial z^2} - 2ik \frac{\partial \widetilde{u}}{\partial x} = 0. \tag{2.27}$$

As seen in Equation (2.26), the remaining slowly varying z dependence in the complex wave amplitude $\widetilde{u}(x, y, z)$ is the result of diffraction effects and can be expressed mathematically by the paraxial approximation [98].

$$\left|\frac{\partial^2 \widetilde{u}}{\partial z^2}\right| \ll \left|2k \frac{\partial \widetilde{u}}{\partial z}\right| \qquad \text{and} \qquad \left|\frac{\partial^2 \widetilde{u}}{\partial z^2}\right| \ll \left|\frac{\partial^2 \widetilde{u}}{\partial x^2}\right|, \left|\frac{\partial^2 \widetilde{u}}{\partial y^2}\right| \tag{2.28}$$

This approximation displays that the variation of propagation is slow compared to the optical wavelength λ, as in $exp(-jkz)$, but also to the transverse extent of the wave due to the finite width of the beam. Therefore, Equation (2.27) can be further reduced to the paraxial wave equation, given by

$$\frac{\partial^2 \widetilde{u}}{\partial x^2} + \frac{\partial^2 \widetilde{u}}{\partial y^2} - 2ik\,\frac{\partial \widetilde{u}}{\partial x} = 0. \tag{2.29}$$

The introduction of the Laplace operator ∇_t^2, which operates on coordinates of the transverse plane, yields a more general form of Equation (2.29).

$$\nabla_t^2 \widetilde{u}(\mathbf{s}, z) - 2ik\,\frac{\partial \widetilde{u}(\mathbf{s,z})}{\partial z} = 0 \tag{2.30}$$

The parameter $\mathbf{s}$ refers to the transverse coordinates in different coordinate systems. One solution to the paraxial wave equation is the fundamental Gaussian TEM_{00} mode

$$\widetilde{E}(r,z) = \widetilde{E_0}(r,z)\,\frac{\omega_0}{\omega(z)}\,exp\left[-\frac{r^2}{\omega^2(z)}\right]\,exp\left[-i\frac{kr^2}{2R(z)}\right]\,exp\left\{-i\left[kz - \psi(z)\right]\right\} \tag{2.31}$$

where ω_0, $\omega(z)$, $R(z)$ and $\psi(z)$ represent the beam waist, beam radius, the radius of the curvature of the wavefront and the Guoy phase shift along the propagation axis, respectively [32, 85, 98, 100, 107]. All necessary parameters of the Gaussian beam can be related to ω_0 and the ratio z/z_R by the following set of equations:

$$\begin{aligned} \omega_0 &= \sqrt{\frac{2z_R}{k}} = \sqrt{\frac{\lambda_0 z_R}{n\pi}} & R(z) &= z\left[1 + \left(\frac{z_R}{z}\right)^2\right] \\ \omega(z) &= \omega_0\sqrt{1 + \left(\frac{z}{z_R}\right)^2} & \psi(z) &= tan^{-1}\left(\frac{z}{z_R}\right). \end{aligned} \tag{2.32}$$

The Rayleigh length z_R, defined as the distance along the propagation axis over which the beam diameter spreads by a factor $\sqrt{2}$, is related to ω_0 shown in

$$z_R = \frac{\pi n \omega_0^2}{\lambda_0}. \tag{2.33}$$

It marks the approximate dividing line between the near field or collimated and far field regions [98, 100]. For $|z| \gg z_R$, the beam size $\omega(z)$ and the half-angle $\phi_{1/e}$ are given by

$$\omega(z) \approx \omega_0 \frac{z}{z_R} \tag{2.34}$$

$$\tan\phi_{1/e} = \frac{\lambda_0}{n\pi\omega_0} \approx \phi_{1/e}. \tag{2.35}$$

Within the far field region, the angular spread is defined by the width corresponding to the $1/e$ point for the $\widetilde{E}$ amplitude. Because $I \propto |E|^2$, the corresponding three-dimensional (3D) intensity distribution is given by

$$I(r,z) = I_0 \frac{\omega_0^2}{\omega^2(z)} exp\left[-2\frac{r^2}{\omega^2(z)}\right] \tag{2.36}$$

where I_0 is the maximum intensity at the center of the beam. ω_0 and $\omega(z)$ represent the $1/e^2$ intensity contour at the beam waist ($z = 0$) and at a distance z along the propagation axis. The term $\omega_0^2/\omega^2(z)$ guarantees that the total power is conserved during the propagation [112]. The total power of an optical beam $P(z)$ leads to the radial intensity variation along the propagation direction of

$$I(r,z) = \frac{2P(z)}{\pi\omega^2(z)} exp\left[-2\frac{r^2}{\omega^2(z)}\right]. \tag{2.37}$$

The higher-order solutions to the paraxial wave equation in free space can take the form of Hermite Gaussian functions in rectangular coordinates. Furthermore, they provide good approximations for the transverse eigenmodes of stable laser cavities with finite diameter mirrors [1, 98, 100].

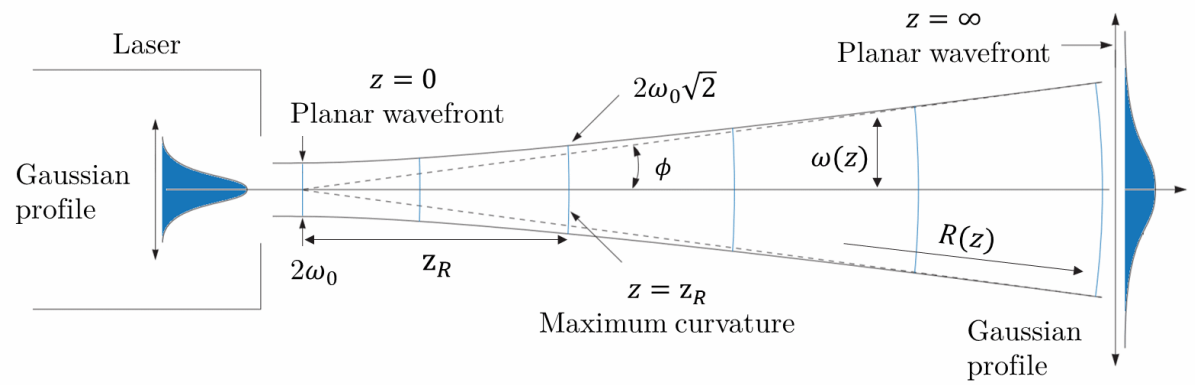

Figure 7: Laser beam propagation: Ray path illustration and Gaussian parameters associated with the minimum beam waist ω_0. Figure adapted from reference [49].

2.3.2 *Zemax OpticStudio*

Simulation and optimization of the optical setup was achieved by using the commercial software *Zemax OpticStudio*[4]. It is an optical design program, based on ray tracing, in particular light propagation through an optical system. Two distinct ray tracing modes are supported:

Sequential (SQ) mode: It is limited to modeling point sources situated on the object surface. Optical components are defined by surfaces (front and back) which are located using a local coordinate system [3]. All rays intersect with the same set of surfaces in a strict sequential order.

Non-sequential (NSQ) mode: In contrast to SQ mode, far more complex light sources, e.g. a Gaussian source, can be used. All optical components are modeled as 3D objects in a global independent coordinate system. Ray propagation through surfaces is determined exclusively by the position and properties of the objects. Therefore, multiple surface hits in any order are possible [3].

The most fundamental graphical user interfaces (GUIs) during the designing and optimization process are introduced in Figure 8 and discussed in more detail below.

1. The system explorer (SE) contains the most basic optical parameters including the aperture, fields, wavelengths, intensity profiles and many more.
2. The lens data editor (LDE) represents the main design interface of the optical setup including all components starting from the object to the image surface and their geometrical relation. It further shows the majority of the elemental lens data.
3. The multi-configuration editor (MCE) offers the ability to simultaneously define multiple configurations of system parameters, e.g. LD parameters and separation distances, for more comprehensive ray tracing simulations.
4. The merit function editor (MFE) provides a list of operands to construct the merit function with a specific set of constraints and target values for the optical system.
5. The non-sequential component editor (NSCE) is the equivalent to the LDE in NSQ mode. It displays all light sources and components as 3D objects.

[4] (2016), *Zemax OpticStudio* (16.5 SP3), *Zemax LLC*. [Software] Accessed: Dezember, 2016.

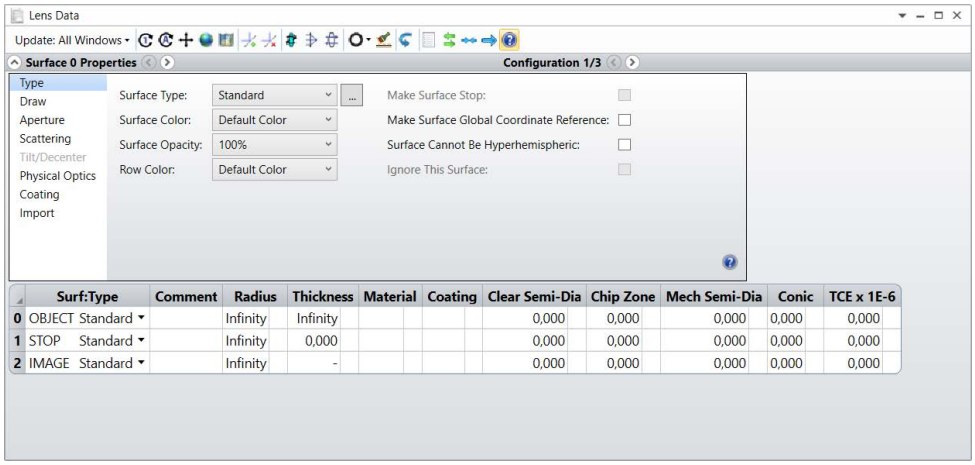

(a) LDE.

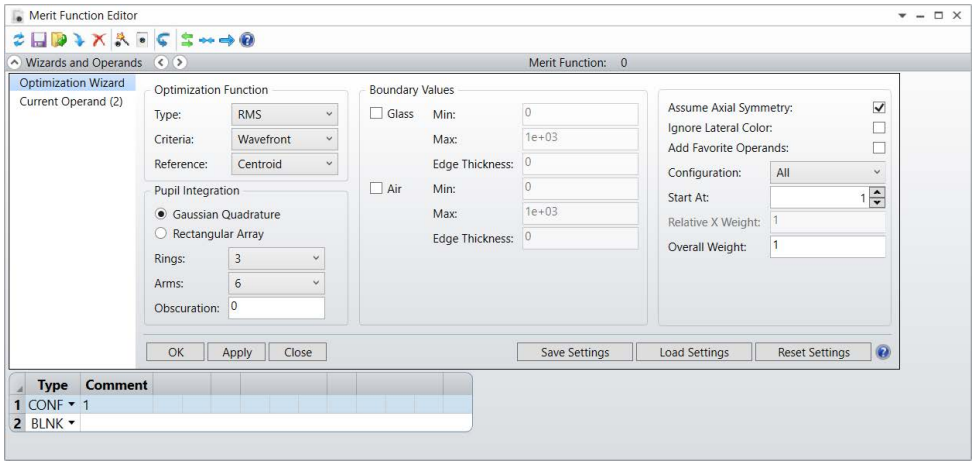

(b) MFE.

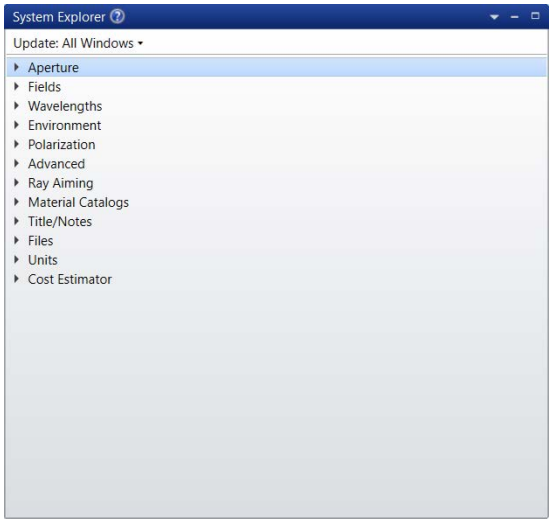

(c) SE.

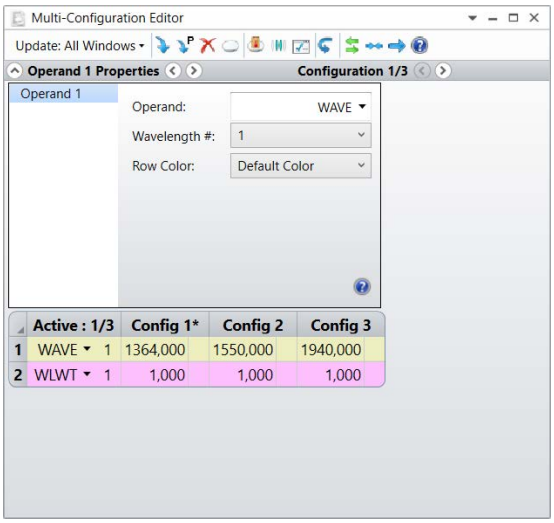

(d) MCE.

Figure 8: *Zemax*: Graphical user interfaces in SQ mode.

In this work, the design and optimization process of the optical setup was achieved in SQ mode. All optical devices implemented are part of the library of stock commercial lenses. Once the optical system was optimized, it was transferred to NSQ mode for a more extensive beam propagation analysis. This was done by the integrated convert to NSC group feature, which transforms a pre-defined range of surfaces in the LDE interface into a group of 3D objects in an NSQ optical system while preserving the geometric relations.

2.3.2.1 Apodization Type

Uniform: All optical rays are equally distributed over the entrance pupil ρ, representing the default setting in *Zemax*. The entrance pupil defines the system's clear aperture for optical ray tracing in SQ mode.

Gaussian: All optical rays launched from a light source in *Zemax* show a Gaussian intensity distribution over the entrance pupil ρ. The Gaussian apodization type implicates an amplitude variation over the entrance pupil that is of Gaussian shape. In *Zemax*, the light amplitude $A(\rho)$ is defined as

$$A(\rho) = A_0 \, exp\left(-G\rho^2\right). \tag{2.38}$$

$A(\rho)$ is normalized to unity at the center of the entrance pupil. The parameters ρ and G represent the normalized entrance pupil coordinate and the apodization factor, respectively. The apodization factor defines the rate of decrease of the beam amplitude with respect to the radial pupil coordinate. For uniform illumination, the apodization factor is $G = 0$. The fundamental Gaussian mode is achieved by $G = 1.0$. The amplitude at the edge of the entrance pupil drops to the $1/e$ of the center value. On the basis of $I \propto |E|^2$, the intensity falls to the $1/e^2$ point of the center intensity I_0.

$$I(\rho) = I_0 \, exp\left(-2G\rho^2\right) \tag{2.39}$$

$$= I_0 \, exp\left(-2\left(\sqrt{G}\rho\right)^2\right) \tag{2.40}$$

As seen in Equation (2.40), the entrance pupil radius is $\sqrt{G}$ times the Gaussian beam radius at the $1/e^2$ point in intensity. Hence, an increase in G significantly reduces the beam intensity at the edge of the entrance pupil. Figure 9 illustrates the influence of the apodization factor G on the beam intensity variation over the entrance pupil for uniform

and Gaussian illumination. In the particular case of $G = 1.0$, 2.0, 4.0, and 8.0, the system aperture clips only (13.5, 1.83, 0.0335 and 1.13×10^{-5}) % of the peak intensity, respectively. For this work, in the context of the three lens system, the $1/e^8$ beam width was used for the geometric calculations in order to minimize the energy cut-offs and optimize the collimation of the low intensity parts of the Gaussian profile.

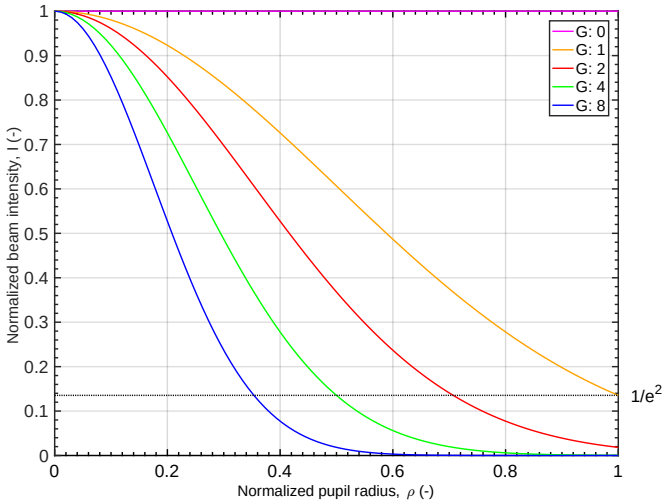

Figure 9: *Zemax*: Intensity distribution over entrance pupil for different values of the apodization factor G.

This was achieved by enlarging the apodization factor G from 1.0 to 4.0 and simultaneously increasing the aperture value from 0.22 to 0.44 in the SE interface in order to maintain the same geometric relations as seen in Equation (2.38). By this definition, the edge of the entrance pupil represents the $1/e^8$ point in intensity whereas the fiber diameter still equals the $1/e^2$ point in intensity of a Gaussian intensity profile.

2.3.2.2 Optimization

The optimization is done in the MFE interface, highlighted in Figure 8b. The merit function Equation (2.41) is a numerical representation of the optical setup deviation to a specific set of target values. It is described as a weighted sum of differences between target and current values of design parameters [21]. The optimization algorithm in *Zemax* will attempt to reduce the value of the merit function with respect to the boundaries to a minimum. Various types, criteria, integration methods and operands are available in order to set different constraints for the system.

$$MF^2 = \frac{\sum W_i(V_i - T_i)^2}{\sum W_i} \tag{2.41}$$

W_i....Absolute value of the operand i T_i....Target value of the operand i

V_i ....Current value of the operand i

For this work, the optimization process for the optical setup was focused on the beam dimensions at the image surface and the collimation quality. Therefore, certain merit function criteria and settings need to be addressed in more detail:

Type: Root mean square (RMS)
The merit function displays the RMS error of all the configurations regarding a specific criterion with optional incorporation of further constraints.

Criterion: Angular radius
It represents the radial extent of the angular aberration in the image space with respect to the centroid, which is defined as the average position of rays traced through the optical system. The target value is zero for ideal beam collimation.

Pupil integration method: Gaussian quadrature
Zemax uses the Gaussian quadrature numerical method to compute integrals as a weighted sum at specific points, defined by rings and arms, in order to construct the merit function. The intersection points of rings and arms represent a specific location on the entrance pupil as shown in Figure 10. At each point, represented by the ANAC operand, rays are being traced for the optimization algorithm.

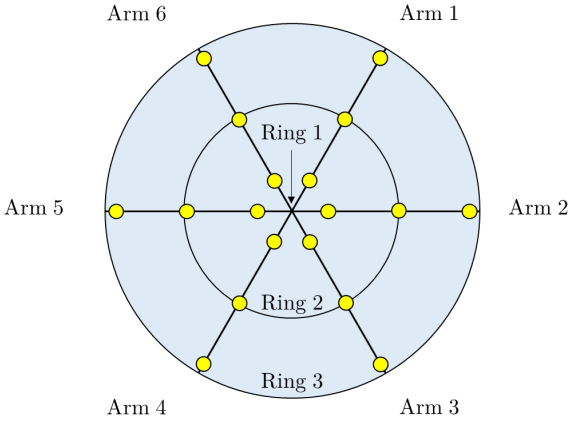

Figure 10: *Zemax*: Illustration of rings and arms and their intersection points in association to the Gaussian quadrature numerical method used for the optimization process.

Table 3: *Zemax*: List of all implemented operands in the design and optimization process.

Type	Description
WAVE	Wavelength
WLWT	Wavelength weight
REAX	Real ray x-coordinate
REAY	Real ray y-coordinate
OPLT	Less than target value
NPAR	NSQ object parameter modification
RANG	Ray angle in radians with respect to local z-axis
ANAC	Angular aberration radial direction with respect to the centroid

2.3.2.3 Ray Tracing

In this project, ray tracing analysis was focused on the beam dimensions and energy distribution at the image surface of the optical system. The irradiance distribution of the two-dimensional (2D) beam shape and the associated irradiance along the x- and y-axis were recorded for both uniform and Gaussian illumination types. In SQ mode, the data was recorded and displayed in the geometric image analysis (GIA) interface. In contrast, this part was accomplished by detectors in NSQ mode. All detectors were directly placed in the NSCE interface as independent 3D objects.

Furthermore, the polarization feature, which accounts for potential thin film, bulk and the Fresnel absorption effects, was activated in both modes for all ray tracing simulations in order to obtain a comprehensive feedback of the transmission efficiency of the optical system. In addition, the ignore error feature was selected in NSQ mode, in order to suppress potential geometric errors notifications due to the comprehensive ray tracing process. In the undesired case of geometric errors, each individual error ray was extracted from the ray database. Subsequent comprehensive step-by-step investigation of the error ray propagation through the optical system in regard to the associated energy loss was achieved by the integration of multiple detectors surfaces along the propagation axis.

2.3.3 Optical Ray Tracing

The next part focuses on optical ray tracing, especially on the collimation of a point source and expansion of a laser beam. In this section, the calculations are based on the assumption of ideal thin lenses [79].

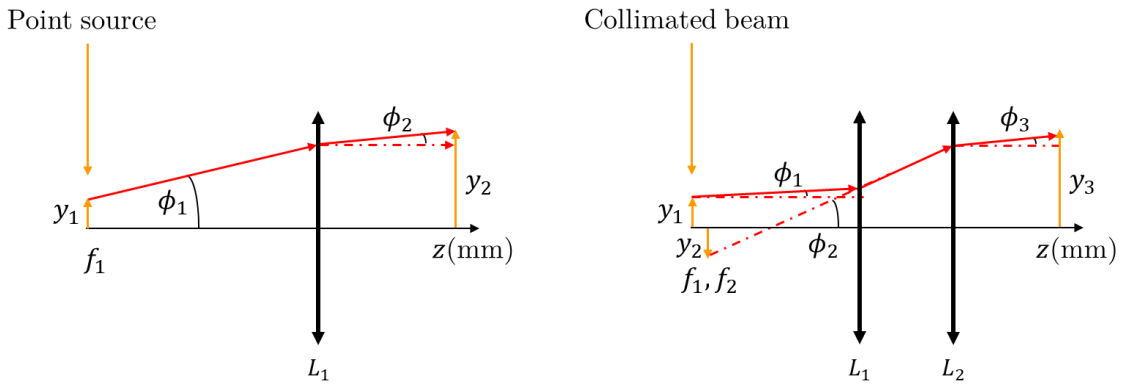

(a) **(b)**

Figure 11: Optical ray tracing: Ray propagation for (a) light collimation from a point source and (b) laser beam expansion.

2.3.3.1 Collimating Light from a Point Source

Due to the fact that nothing is ever a true point source, the actual size of the light source needs to be considered as well. Figure 11a shows a point source with a radius of y_1 and a divergence angle ϕ_1 [79]. The light collimation is done by a lens L_1 with a focal length f_1. By using the geometrical illustration and the optical invariant $y_2\phi_2 = y_1\phi_1$, the final beam radius y_2 and divergence ϕ_2 can be determined by

$$\phi_2 = \arctan\left(\frac{y_1}{f_1}\right) \qquad (2.42) \qquad\qquad y_2 = \frac{\tan(\phi_1)}{f_1}. \qquad (2.43)$$

2.3.3.2 Expanding a Laser Beam

For many optical applications, it is necessary to expand a laser beam. One possible arrangement of two lenses is shown in Figure 11b. In this case, a well-collimated laser beam of radius y_1 and divergence ϕ_1 is expanded by a divergent lens L_1 with a negative focal length f_1. This lens produces a virtual image with a radius y_2 and a divergence angle of ϕ_2. Based on the thin lens equation, a well-collimated laser beam yields $s_1 \approx \infty$

resulting in a virtual image at a distance $s_2 = f$, with $f = -f_1$. The second lens L_2 with a positive focal length f_2 re-collimates the expanded laser beam, resulting in a final beam radius y_3 and divergence ϕ_3. The geometrical illustration and the optical invariant lead to the following set of equations:

$$\phi_2 = \arctan\left(\frac{y_1}{|-f_1|}\right) \tag{2.44}$$

$$y_2 = \tan(\phi_1)\,|-f_1| \tag{2.45}$$

$$\phi_3 = \arctan\left(\frac{y_2}{f_2}\right) \tag{2.46}$$

$$y_3 = \tan(\phi_2) f_2. \tag{2.47}$$

The expansion ratio or magnification M, the expanded beam diameter $2y_3$ and the final beam divergence ϕ_3 are given by

$$M = \frac{y_3}{y_1} = \frac{\tan(\phi_2) f_2}{\tan(\phi_2)\,|-f_1|} = \frac{f_2}{|-f_1|} \tag{2.48}$$

$$y_3 = \tan(\phi_2) f_2 = \frac{y_1 f_2}{|-f_1|} \tag{2.49}$$

$$\phi_3 = \frac{y_2}{f_2} = \arctan\left[\frac{\tan(\phi_1)\,|-f_1|}{f_2}\right]. \tag{2.50}$$

In addition to the assumption of ideally thin lenses, further simplification can be achieved by $\tan\phi \approx \sin\phi \approx \phi$, representing the paraxial approximation.

2.4 Beam Profile Analysis

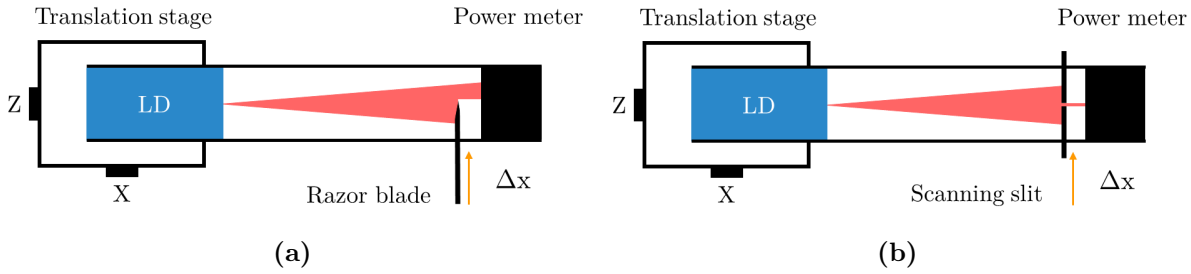

Figure 12: Beam profile analysis: Illustration of the basic measurement principle of the knife-edge method (a) and scanning slit method (b).

This section presents two commonly used beam profiling methods for a quantitative determination of the transverse laser beam profiles and divergence angles. In contrast to the beam profiler device, the knife-edge method (KEM) and the scanning slit method (SSM) are inexpensive and easily applicable to a variety of experiments.
In general, both techniques are based on the translation of a physical aperture (e.g. knife-edge or slit) through the x-y measurement plane, perpendicular to the direction of propagation of the laser beam. The aperture is parallel to the y-axis so that the x-axis equals the scanning direction as seen in Figure 12. Initially, the entire laser beam falls on the power meter showing the total beam power P_0. The change in transmitted power versus translation position of the aperture is measured by the power meter. In order to reduce possible diffraction effects, the spacing between the power meter and the aperture needs to be minimized. The recorded total beam power in the x-y plane along the propagation direction is given by the integral

$$P_0(x, y, z) = \int_{-\infty}^{\infty} \int_{-\infty}^{\infty} I(x, y, z)\, \mathrm{d}x\, \mathrm{d}y. \tag{2.51}$$

Based on the assumption of a radially symmetric Gaussian laser beam with an intensity described by Equation (2.36), the equation can be written as

$$P_0(x, y, z) = I_0 \frac{\omega_0^2}{\omega^2(z)} \int_{-\infty}^{\infty} \exp\left[-2\frac{(x - x_0)^2}{\omega^2(z)}\right] \mathrm{d}x \int_{-\infty}^{\infty} exp\left[-2\frac{(y - y_0)^2}{\omega^2(z)}\right] \mathrm{d}y. \tag{2.52}$$

This integral is solved by the error function (Equation (D.1)), which results in

$$P_0 = I_0\, \omega_0^2\, \frac{\pi}{2}. \tag{2.53}$$

2.4.1 Knife-Edge Method

A sharp knife-edge, typically a razor blade, is used as the aperture and mounted on a translation stage. The adjustment of the micrometer in appropriate increments leads to a decrease in transmitted power until the razor blade covers the entire beam. Hence, the transmitted power falls from P_0 to zero based on the translation position. $P_0/2$ marks the point of the half obstructed beam. An idealized schematic sample data is illustrated in Figure 13a [69]. The transmitted beam power $P(x, y, z)$ is obtained by the integration of the Gaussian irradiance profile over all y and the unobstructed range of x [63]. In order to obtain the normalized transmitted beam power $P_N(x, y, z)$, the integral is divided by the total beam power [23, 69].

$$P(x, y, z) = \int_x^\infty \int_{-\infty}^\infty I(x, y, z)\,\mathrm{d}x\,\mathrm{d}y \tag{2.54}$$

$$P_N(x, y, z) = \frac{\int_x^\infty \int_{-\infty}^\infty I(x, y, z)\,\mathrm{d}x\,\mathrm{d}y}{\int_{-\infty}^\infty \int_{-\infty}^\infty I(x, y, z)\,\mathrm{d}x\,\mathrm{d}y} \tag{2.55}$$

In combination with Equations (2.36) and (D.1), the solution for Equation (2.54) is

$$\begin{aligned} P(x, z) &= I_0 \frac{\omega_0^2}{\omega(z)} \frac{\pi}{2} \int_x^\infty \exp\left[-2\frac{(x - x_0)^2}{\omega^2(z)}\right] \mathrm{d}x \\ &= \frac{P_0}{2}\ \mathrm{erfc}\left[\sqrt{2}\frac{(x - x_0)}{\omega(z)}\right] \\ &= \frac{P_0}{2}\ \left[1 -\ \mathrm{erf}\left(\sqrt{2}\frac{(x - x_0)}{\omega(z)}\right)\right]. \end{aligned} \tag{2.56}$$

The Gaussian beam parameters of interest (e.g. beam radius $w_i(z)$ and beam diameter $D_i(z)$) can be obtained by fitting the experimental data in accordance with Equation (2.56). With respect to Equation (2.55), the normalized transmitted beam power amounts to

$$P_N(x, z) = \frac{1}{2}\ \left[1 -\ \mathrm{erf}\left(\sqrt{2}\frac{(x - x_0)}{\omega(z)}\right)\right]. \tag{2.57}$$

Further information about the error function and the complementary error function (erf and erfc) can be found in Appendix D.2.1.

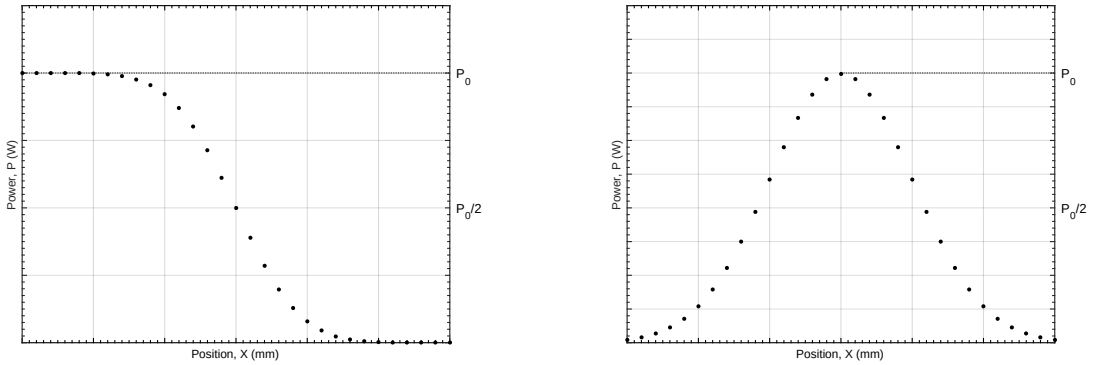

(a) KEM **(b)** SSM

Figure 13: Beam profile analysis: Idealized transmitted beam power P as a function of the aperture position for KEM and SSM measurements.

2.4.2 Scanning Slit Method

As mentioned before, both beam profiling techniques rely on the same principle. In this case, the Gaussian irradiance beam profile is obtained by the translation of a narrow slit aperture. In general, this method is based on the assumption of an infinitely narrow slit, which directly indicates the transmitted power through the slit at any point of the beam profile [19, 69]. Figure 13b displays the idealized experimental data as a function of the slit displacement along the x-axis. In contrast to the KEM, the Gaussian beam parameters are obtained by fitting the experimental data to a Gaussian model and subsequent shape-preserving piecewise cubic interpolation at the $1/e^2$ points in intensity.

Measurement Quality

In case of a finitely narrow slit, the transmitted power $P(x, z)$ can be described by the convolution integral given by

$$\begin{aligned}(f \star g)(t) &= \int_{-\infty}^{\infty} f(\tau) g(t-\tau)\,\mathrm{d}\tau \\ &= \int_{-\infty}^{\infty} f(t-\tau) g(\tau)\,\mathrm{d}\tau\end{aligned} \tag{2.58}$$

where f and g represent the experimental data and the finite slit size, respectively. Hence, the aspect ratio of the slit size to the actual beam size plays a crucial role for the measurement quality and resolution of extremely small intensity features.

CHAPTER 3

Realization

This chapter focuses on the simulation and optimization of the optical setup, incorporating specific boundary conditions and the laser beam coupling into the resonant PA cell. In addition, topics concerning LT-PEMFC material compatibility, PA cell heating problems and LD characterization measurements are discussed in detail. Ultimately, the complete PA setup and validation measurement in humid environment is outlined thoroughly.

3.1 Optical Setup

The main goal was to design a universal optical setup, eligible for all three LDs, in order to fulfill a set of specifications and constraints regarding the PA cell and beam shape. The design process consisted of a two step procedure. First, simple geometric calculations regarding the focal length, beam diameter and divergence angle were made. This was accompanied by material and optical component research in order to find a good starting point. The second step was the actual design and simulation of the optical system in *Zemax*. All listed optical lenses and anti-reflection (AR) coatings are exclusively manufactured by *Thorlabs, Inc* and are included in the *Zemax* lens catalog. Lens material and AR-C coating characteristics are further investigated and discussed in Section 3.2.

3.1.1 Light Source Modeling

According to the water absorption characteristics, as illustrated in Figure 5, three fiber coupled LDs with a center wavelength of (1364, 1550 and 1940) nm were selected.

3.1.1.1 Geometric Calculations

The first approach of simulating the fiber output was a point source with either a Gaussian or uniform intensity distribution. The point source model was designed based on optical fiber parameters, listed in Table 2. For simplification, the NA and fiber diameter were considered equal size for all LDs, 0.22 and 0.2 mm, respectively. Further details about the adaptation step can be found in Section 3.3.1. In addition, both parameters were assumed to represent the $1/e^2$ point in intensity for a Gaussian intensity profile. The geometric concept is illustrated in Figure 14b.

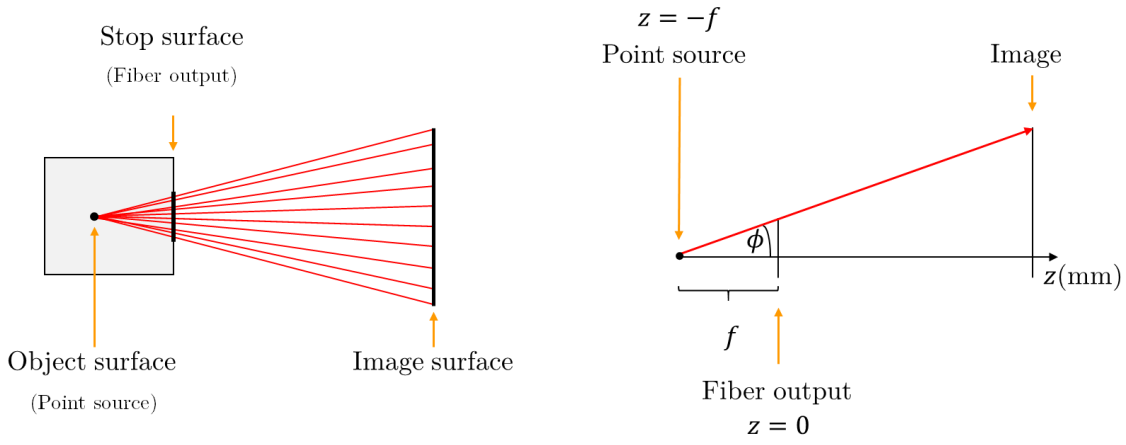

(a) **(b)**

Figure 14: Light source: (a) Illustration of a fiber coupled LD and (b) ray propagation for either uniform or Gaussian illumination.

According to Equations (3.1) and (3.2), the divergence angle ϕ and the distance f between the point source and the fiber output were determined to be $\phi = 12.71\,°$, equivalent to 2.218×10^{-1} rad, and $f = 0.4434$ mm, respectively. Together, these results represented a good starting point to build and optimize the optical model in *Zemax*.

$$\mathrm{NA} = n \cdot sin(\phi) \qquad (3.1)$$

$$tan(\phi) = \frac{\varnothing/2}{f} \qquad (3.2)$$

n ....Index of refraction

ϕ ....Half angle of the cone of radiation

$\varnothing$....Fiber diameter at I($1/e^2$)

f ....Focal length

3.1.1.2 Sequential Mode

Starting with a new project, the LDE interface showed three entries, in particular the object, stop and image surface. The first two represent the actual position of the point source and the associated fiber output beam size, respectively. The last entry depicts the image of the optical setup as shown in Figure 14. First, three configurations of the system parameter λ were implemented in the MCE interface according to Table 2. WAVE and WLWT operands were assigned to the wavelength and wavelength weight, respectively.

Table 4: Light source: Multiple configurations of system parameters in SQ mode.

CF... Configuration			
	WAVE (nm)	WLWT	P (W)
CF 1	1364	1.0	0.02
CF 2	1550	1.0	0.6
CF 3	1940	1.0	0.2

Next, the system aperture was set as the object space numerical aperture (NA = 0.22) in the SE interface. It defines the divergence of rays originating from the point source located at the object surface. By default, the entrance pupil is always illuminated uniformly. Both intensity profiles were achieved by adjusting the apodization type to either Gaussian or uniform. For Gaussian illumination, the apodization factor was set to 1.0, as discussed in Section 2.3.2.1. Hence, the intensity at the edge of the entrance pupil equals $1/e^2$. In addition, the telecentric object space feature was selected to ensure that all chief rays leaving the object surface are parallel to the local z-axis. Aside from the aperture settings, the field specifications need to be addressed for ray tracing simulations of a point source. In this particular case, only a single field point ($X = 0$, $Y = 0$, $W = 1$) was defined in the SE interface, where X, Y and W represent the magnitude of the field point at the object surface and the weight, respectively. All input parameters are based on Table 2.

3.1.1.3 Optimization

The optimization of the variable f for all three configurations at once was accomplished by the application of a simple merit function. For each configuration, the operands REAX, REAY and RANG were implemented in the MFE interface. The first two operands represent the real x- and y-coordinate at the stop surface for ray R_x and R_y, shown in Figure 15.

The REAX and REAY target value was defined as the given fiber radius ⌀/2, corresponding to the x- and y-coordinate respectively. The other operator describes the ray angle of R_x and R_y in radians with respect to the propagation axis (z-axis) at the stop surface. On the basis of the geometric calculations, the obtained divergence angle was set as the RANG target value in radians for both rays. The overall weight of all operands and configurations within the merit function was equally distributed in order to obtain an optimized variable that satisfies all three configurations at once. The minimum merit function was reached at a value of 7.85×10^{-17}, resulting in an optimized distance f and divergence angle ϕ.

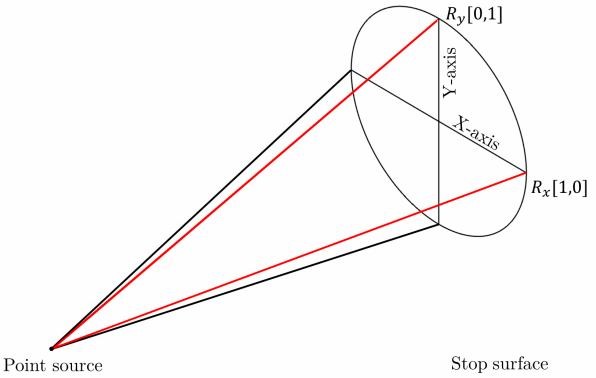

Figure 15: Light source: Marginal rays R_x and R_y defined by normalized entrance pupil coordinates in *Zemax*.

Merit Function Definition:		**Optimization Results:**		
Operands:	RANG	Uniform/ Gaussian illumination		
	REAX	Merit function :		7.85×10^{-17}
	REAY	f_{opt} (mm)	:	0.4434
Variable:	f	ϕ_{opt} (rad)	:	2.218×10^{-1}

This result confirms the previous geometric calculations in Section 3.1.1 based on Equations (3.1) and (3.2) and is valid for both intensity profiles, Gaussian and uniform, respectively. In the next step, a paraxial Gaussian beam was assumed in order to calculate all necessary input parameters for the NSQ Gaussian source as described in Section 3.1.1.4.

First, the Gaussian beam waist ω_0 was calculated for each configuration by Equation (2.35) with respect to the condition of $|z| \gg z_R$. Furthermore, the ideal Gaussian beam data, such as the radial beam size ω at the $1/e^2$ point in intensity, Rayleigh length z_r and divergence half-angle ϕ were computed at the stop surface. This was achieved by the integrated paraxial Gaussian beam calculator. The wavelength λ, the Gaussian waist size ω_0, the quality factor M^2 and the optimized distance f_{opt} served as the input parameters for all calculations. The ideal Gaussian beam data results at the stop surface are shown in Table 5. It is apparent that the calculated radial beam size ω is in good agreement with the given fiber radius. Due to the Rayleigh criteria in Equation (2.33), the point

source is a valid representation of Gaussian beams for this setup. Further information about paraxial Gaussian beams can be found in Section 2.3.1.

Table 5: Light source: Paraxial Gaussian beam calculator input parameters and results in SQ mode.

	Input parameters					Results at stop surface		
	λ (nm)	NA	ω_0 (mm)	M^2	f_{opt} (mm)	ω (mm)	z_r (mm)	ϕ (°)
LD 1	1364	0.22	1.925×10^{-3}	1.0	0.4434	0.1000	8.536×10^{-3}	12.71
LD 2	1550	0.22	2.188×10^{-3}	1.0	0.4434	0.1000	9.700×10^{-3}	12.71
LD 3	1940	0.22	2.738×10^{-3}	1.0	0.4434	0.1000	1.214×10^{-2}	12.71

3.1.1.4 Non-Sequential Mode

The program offers a pre-defined Gaussian source with an angular distribution defined by two parameters, namely the Gaussian beam size and position. The Gaussian beam size represents the radial beam size at the $1/e^2$ point in intensity. The second parameter is defined by the distance from the point of divergence of the rays to the source location. Hence, the parameters ω and f_{opt} were used for this setup, respectively. In other words, the Gaussian source assumes a virtual point source at a negative value of parameter f_{opt} with a beam size ω at the origin. In order to guarantee an exact model transfer to NSQ mode, all input parameters were based on the paraxial Gaussian beam calculator and optimization done in SQ mode, as summarized in Table 5.
Next, multiple configurations with respect to the three potential LDs were added to the optical setup in the MCE interface. In addition to the WAVE and WLWT parameters, the NPAR operand was employed to alter the power P and the beam size ω of the Gaussian source. All settings are displayed in Table 6.

Table 6: Light source: Multiple configurations of system parameters in NSQ mode.

	WAVE (nm)	WLWT	NPAR (W)	NPAR (mm)
CF 1	1364	1.0	0.02	0.1000
CF 2	1550	1.0	0.6	0.1000
CF 3	1940	1.0	0.2	0.1000

3.1.1.5 Ray Tracing

The ray tracing analysis, extensively discussed in Section 2.3.2.3, was performed in both operation modes by using the following settings:

Sequential Mode

For each configuration defined in the MCE interface (Table 4), 100 million rays were traced through the SQ light source model, shown in Figure 16a. The resolution of the detector in the GIA interface was set to 201 x 201 pixels. The image surface was located at $z = 5\,\text{mm}$ with respect to the fiber output. All ray tracing results at the image surfaces for both uniform and Gaussian illumination are displayed in Section 4.1.1.1.

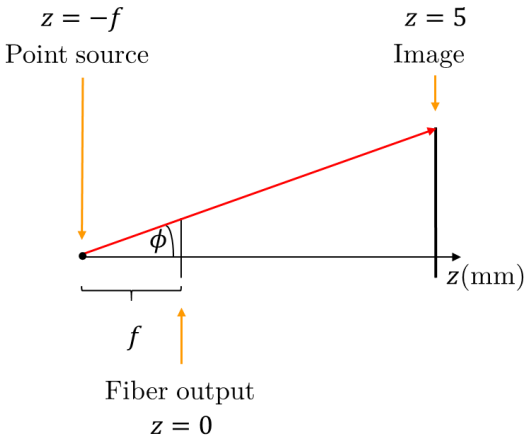

(a) SQ mode.

Non-Sequential Mode

In NSQ mode, one detector D_i with a resolution of 201 x 201 pixels was added to the optical system as shown in Figure 16b. Identical to SQ mode, the detector was placed at a z-position of 5 mm. In total, 100 million rays were traced for each configuration. All ray tracing results at the image surface for Gaussian illumination are shown in Section 4.1.1.2.

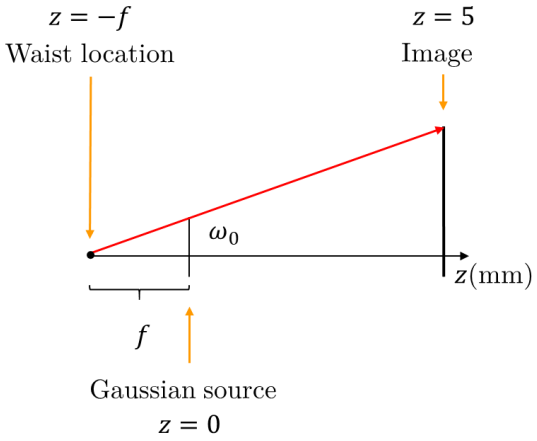

(b) NSQ mode.

Figure 16: Light source: Ray propagation in both modes for ray tracing analysis.

3.1.2 Design Specifications and Constraints

The previously designed and optimized light source served as the starting point for the modeling process of the final optical setup in *Zemax* for future PA measurement applications, in order to fulfill a set of specifications and constraints regarding the PA setup.

Boundary Conditions:

- Resonant PA cell dimensions: $(28 \times 10 \times 10)\,\mathrm{mm}$
- Laser window dimensions: $(28 \times 14 \times 3)\,\mathrm{mm}$
- Laser beam dimensions: $(22 \times 8)\,\mathrm{mm}$

Requirements:

- Optical setup for all three LDs
- Collimated laser beam into the PA cell
- High and efficient power output
- Laser intensity $\rightarrow$ zero at PA cell edge
- High resilience.

Due to the high sensitivity of the PA measurement to potential measurement artifacts based on light interaction with the PA cell material, the collimation quality and the beam dimensions were considered the most crucial parameters among the other for the designing process. On the basis of that two different optical concepts, distinctive by the number and type of lenses, were designed to guarantee a highly collimated laser beam with an intensity close to zero at the edge of the PA cell. Both optical systems are displayed and extensively discussed in the following section. Subsequently, the obtained ray tracing results were compared with regard to their beam dimensions, optical transmission, efficiency and resilience. More information can be found in Section 4.1.

3.1.3 Two Lens Setup

The first concept was an optical setup built of two plano-convex cylindrical lenses. Figure 17b shows the beam path through the optical setup in greater detail. The main reason to start with a two lens system was the simple design. Based on the fact of having only two optical devices in the beam path, the final beam transmission and efficiency were expected to be superior to a three lens setup.

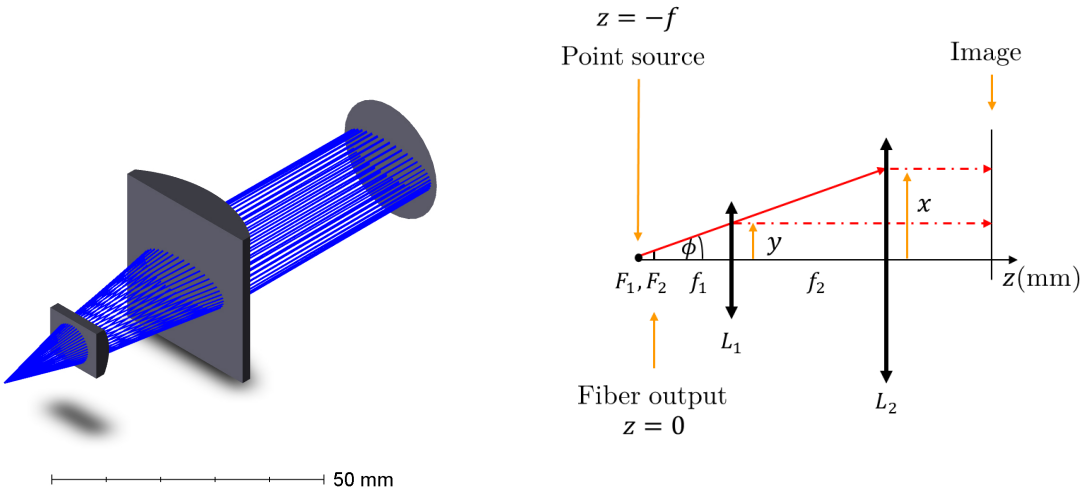

Figure 17: Two lens setup: (a) 3D lens concept and (b) ray propagation illustration.

3.1.3.1 Geometric Calculations

This optical setup is based on the light source model described in the previous Section 3.1.1. The first lens L_1, placed at a focal length of f_1, collimates the y-axis. X-axis collimation is done by the second lens in the setup, placed at a focal length of f_2, as shown in Figure 17b. F_1 and F_2 represent the focal point of L_1 and L_2 respectively. According to Equation (3.2), the focal lengths f_1 and f_2 were determined in order to satisfy the required elliptical laser beam dimensions as described in Section 3.1.2.

Geometric Calculation Results:

Uniform/ Gaussian illumination

$\phi\,(^\circ)$: 12.71

$f_1\,(\text{mm})$: 17.74

$f_2\,(\text{mm})$: 48.77

3.1.3.2 Sequential Mode

Starting with the light source model, two lenses were selected based on the geometric calculation results. In addition to the focal length, the center thickness, the height and absorption characteristics of the material were taken into account for the lens selection process as well. The most relevant lens parameters are displayed in Table 7.

Table 7: Two lens setup: Lens parameters for uniform and Gaussian illumination.

FL... Focal length BFL... Back focal length CT... Center thickness

Lens	Item (#)	FL (mm)	BFL (mm)	Length (mm)	Height (mm)	CT (mm)	Material	Coating
Lens 1	LJ1960L1	20.0	17.8	12.0	10.0	3.29	N-BK7®	AR-C
Lens 2	LJ1695L1	50.0	45.5	32.0	30.0	6.80	N-BK7®	AR-C

Both lenses were implemented in the optical system with the plano-side facing the light source as illustrated in Figure 17a. In order to ensure laser beam collimation in both axes, the second lens was rotated by 90 ° around the z-axis with respect to the first lens. Based on the light source model, the MCE interface was defined as shown in Table 4.

3.1.3.3 Optimization

In this case, the optimization process was focused on the actual position of lens L_1 and L_2 along the propagation axis as shown in Figure 17b. The main goal was to achieve a highly collimated laser beam that satisfies the required boundary conditions, defined in Section 3.1.2. Therefore, a sequential merit function with two variables, namely the focal lengths f_1 and f_2, was defined in the MFE interface as the following:

Merit Function Definition:

Type:	RMS	Operands:	ANAC
Criteria:	Angular radius		REAX + OPLT
Reference:	Centroid		REAY + OPLT
Pupil integration:	Gaussian quadrature	Variables:	f_1, f_2

The merit functions represent the RMS of all the configurations, regarding the angular radius criteria with respect to the centroid. 3 rings and 6 arms were specified for the Gaussian quadrature numerical method, resulting in a set of ANAC operands per configuration. Aside the RMS angular radius criteria, the beam dimension needed to be considered as well for the optimization process. This was accomplished by the implementation of a set of two operands (REAX and REAY) for each individual configuration. The associated target value corresponds to the x- and y-dimension of the desired beam profile at the image surface, respectively. In combination with the OPLT operand, the actual REAX and REAY value was forced to be less than the target value. Further information can be found in Section 2.3.2.

Optimization Results:

Uniform/ Gaussian illumination

Merit function	:	1.289×10^{-3}
RMS angular radius (rad)	:	2.027×10^{-3}
$f_{1_{opt}}$ (mm)	:	17.529
$f_{2_{opt}}$ (mm)	:	46.519

The optimization results for both focal lengths are in good agreement with the back focal lengths of both lenses, as seen in Table 7. The subscript *opt* identifies the optimized value.

3.1.3.4 Non-Sequential Mode

As described in Section 2.3.2, the optimized optical setup was transferred to NSQ mode by the convert to NSC group feature without affecting the geometric relations. In contrast to SQ mode, the point source was replaced by the Gaussian light source, previously defined in Section 3.1.1.4. Ultimately, three configurations were specified in the MCE interface in accordance with Table 6.

3.1.3.5 Ray Tracing

Identical to Section 3.1.1.5, the ray tracing analysis, extensively discussed in Section 2.3.2.3, was performed in both operating modes on the basis of the following settings:

Sequential Mode

A total number of 10 million rays were launched through the optical setup for each configuration, defined in the MCE interface. Compared to Section 3.1.1.5, the reduction in rays is due to the more complex optical system, as shown in Figure 18a, and the associated extended computation time. The resolution of the detector in the GIA interface was defined as 201 x 201 pixels. All ray tracing results at the image surface for Gaussian and uniform intensity distribution are displayed in Section 4.1.2.1.

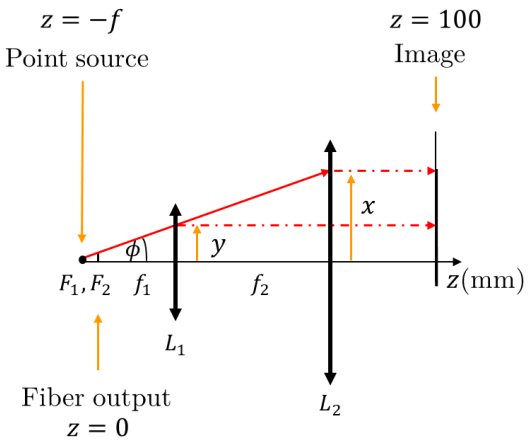

(a) SQ mode.

Non-Sequential Mode

In total, four detectors D_i, each with a resolution of 201 x 201 pixels, were installed in the optical setup along the LD propagation axis. As illustrated in Figure 18b the detectors were placed at a z-position of (25, 70, 85 and 100) mm with respect to the Gaussian source location. For each individual configuration, the same number of rays were traced through the entire optical setup as in SQ mode. All ray tracing results for Gaussian illumination at the image surface are displayed in Section 4.1.2.2.

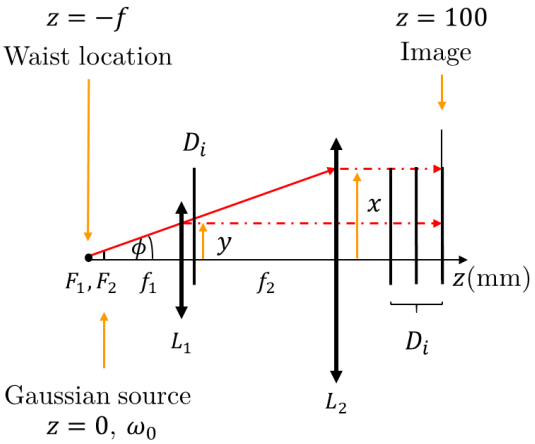

(b) NSQ mode.

Figure 18: Two lens setup: Ray propagation in both modes for ray tracing analysis.

3.1.4 Three Lens Setup A

The second concept illustrates a three lens system consisting of a collimation lens and two plano-cylindrical lenses, one convex the other concave respectively. On the basis of the required beam dimensions, defined in Section 3.1.2, the y-axis was adjusted by the collimation lens, whereas the x-axis was optimized by a beam expanding set of two cylindrical lenses. In this case, the x-dimension was further expanded by the plano-concave cylindrical lens L_2 and subsequently re-collimated by the plano-convex cylindrical lens L_3. In contrast to the first concept, the pre-collimation enables a high resilient and stable optical system.

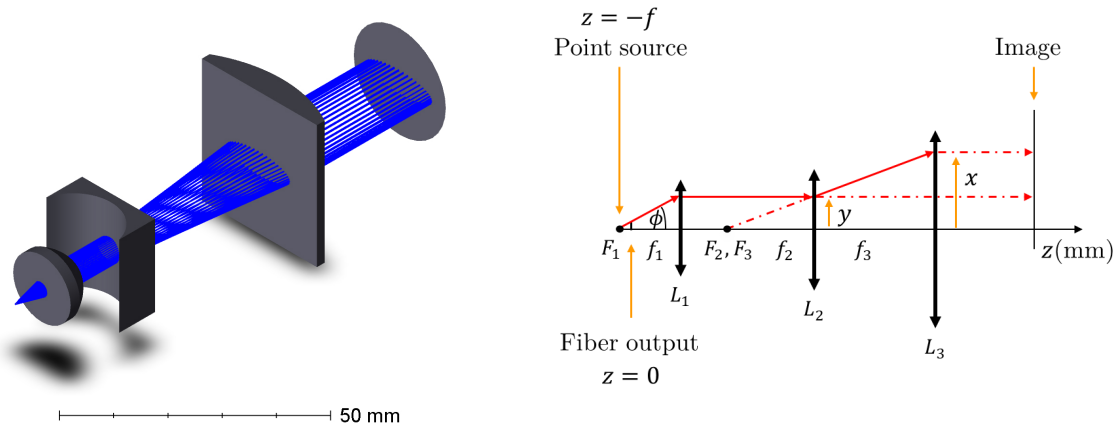

Figure 19: Three lens setup: (a) 3D lens concept and (b) ray propagation illustration.

3.1.4.1 Geometric Calculations

Based on the definition of the light source model, the ideal focal length f_1 for a beam diameter of 8 mm is 17.74 mm. The ideal magnification factor was determined to be $M = 2.75$ by Equation (2.48) for the defined laser beam dimensions in Section 3.1.2. This is valid for both intensity profiles. On the basis of the two lens results, the $1/e^2$ Gaussian beam width consideration was not sufficient enough for the geometrical calculations. In order to minimize the energy cut-offs and optimize the collimation of the low intensity parts, the $1/e^8$ beam width was used instead. Hence, an individual optical setup was designed for each illumination type.

In *Zemax*, this was achieved by changing the apodization factor G and NA to 4.0 and 0.44 in the SE interface, respectively. Further information about the apodization factor can be found in Section 2.3.1. The fiber output diameter, representing the $1/e^8$ width, was calculated with regard to the optimized focal length f_{opt} as shown in Section 3.1.1.3 by Equation (3.2). In conclusion, the starting parameters for both illumination types are:

Uniform illumination		Gaussian illumination ($1/e^8$)	
NA	0.22	NA	0.44
ϕ (rad)	0.2218	ϕ (rad)	0.4556
$\varnothing$ (mm)	0.1	$\varnothing$ (mm)	0.2173
f_1 (mm)	17.74	f_1 (mm)	8.164

The main lens selection criterion for each illumination type was the ideal focal length f_1 of L_1, followed by the center thickness and diameter. All necessary lens parameters for both uniform and Gaussian illumination can be found in Tables 8 and 9 respectively. Based on the real focal length of L_1, the collimated beam radius y was calculated by Equation (2.43). Next, the magnification factor M_{Dim} was computed by Equation (2.48) with respect to a beam diameter of 22 mm in the x-dimension. Based on this magnification, possible focal length combinations of f_2 and f_3 were considered for each illumination type. The actual magnification power M_{FL} of lens L_2 and L_3 was determined by Equation (2.48) as well. The final beam radius in the x-dimension was calculated by Equation (2.49). Further information about the beam expanding optics can be found in Section 2.3.3.1. The obtained beam radius in the x- and y-dimension at the image surface, the magnification parameters and the difference in back focal lengths (ΔBFL) are listed below.

Geometric Calculation Results:

Uniform illumination		Gaussian illumination ($1/e^8$)	
x (mm)	10.83	x (mm)	12.38
y (mm)	2.706	y (mm)	3.920
M_{Dim}	4.065	M_{Dim}	2.806
M_{FL}	4.000	M_{FL}	3.158
ΔBFL (mm)	39.80	ΔBFL (mm)	35.80

3.1.4.2 Sequential Mode

On the basis of the previous geometric calculation results, two optical setups were designed in order to fulfill the boundary conditions for both illumination types. Starting with the light source model of Section 3.1.1, three lenses were added along the propagation axis to the optical setup as highlighted in Figure 19. The design procedure was identical for both optical systems in SQ mode. Additional information about the implemented lenses can be found in Tables 8 and 9.

Uniform Illumination

First the aspheric condenser lens (ACL) L_1 was placed with the plano-side facing the light source into the optical setup as illustrated in Figure 19a. Subsequently, both cylindrical lenses were added and rotated by 90 ° about the z-axis with respect to the first lens. The distance between the ACL and the concave cylindrical lens L_2 was defined as 10 mm. The spacing between the plano-sides of the two cylindrical lenses L_2 and L_3 was set to the calculated difference in back focal lengths. Hence, collimation of the laser beam in both axes with regard to the boundary conditions in Section 3.1.2 was achieved. All settings and configurations in the MCE interface are based on the light source model as shown in Section 3.1.1 in Table 4.

Table 8: Three lens setup A: Lens parameters for uniform illumination.

Aspheric condenser lens

Lens	Item (#)	FL (mm)	BFL (mm)	Diameter (mm)	NA	CT (mm)	Material	Coating
Lens 1	ACL1512U	12.0 ± 8%	7.0	15	0.61	8.0	B270	AR-C

Cylindrical lenses

Lens	Item (#)	FL (mm)	BFL (mm)	Length (mm)	Height (mm)	CT (mm)	Material	Coating
Lens 2	LK1753L1	−15.0	−16.3	12.0	10.0	2.0	N-BK7®	AR-C
Lens 3	LJ1430L1	60.0	56.1	32.0	30.0	5.0	N-BK7®	AR-C

Gaussian Illumination

The step-by-step design process in SQ mode is identical to the uniform illumination described above. Based on the geometrical calculation results of the extended Gaussian profile ($1/e^8$), a different set of lenses was used in order to satisfy the final laser beam dimensions. All lens parameters used in this optical setup can be found in Table 9.

Table 9: Three lens setup A: Lens parameters for Gaussian illumination ($1/e^8$).

Aspheric condenser lens

Lens	Item (#)	FL (mm)	BFL (mm)	Diameter (mm)	NA	CT (mm)	Material	Coating
Lens 1	ACL108U	8.0 ± 8%	4.0	10	0.61	5.8	B270	AR-C

Cylindrical lenses

Lens	Item (#)	FL (mm)	BFL (mm)	Length (mm)	Height (mm)	CT (mm)	Material	Coating
Lens 2	LK1037L1	−19.0	−20.3	21.0	19.0	2.0	N-BK7®	AR-C
Lens 3	LJ1430L1	60.0	−56.1	32.0	30.0	5.0	N-BK7®	AR-C

3.1.4.3 Optimization

The optimization procedure was focused on the actual lens position of L_1 with respect to the light source. Furthermore, the lens position of L_3 with respect to lens L_2 along the propagation axis was considered as well, resulting in an optimized difference in back focal lengths (ΔBFL_{opt}). On the basis of the geometrical illustration in Figure 19b, the focal lengths f_1 and f_3 represent the variables that needed to be optimized to guarantee a well-collimated laser beam that fulfills the required boundary conditions, given in Section 3.1.2. Hence, a sequential merit function was defined in the MFE interface as the following:

Merit Function Definition:

Type:	RMS	Operands:	ANAC
Criteria:	Angular radius		REAX + OPLT
Reference:	Centroid		REAY + OPLT
Pupil integration:	Gaussian quadrature	Variables:	f_1, f_3

Further information about the merit function can be found in Section 2.3.2. The collimation was optimized by the angular radius criteria. The implementation of REAX, REAY and OPLT operands allowed the consideration of the required beam dimensions. Identical to the two lens setup, the associated target value for both operands corresponds to the maximum x- and y-dimension of the desired beam profile at the image surface, 4 mm and 11 mm respectively. This process was completed for both optical setups.

Optimization Results:

Uniform illumination			Gaussian illumination ($1/e^8$)		
Merit function	:	8.616×10^{-4}	Merit function	:	3.432×10^{-4}
RMS angular radius (rad)	:	1.102×10^{-3}	RMS angular radius (rad)	:	5.396×10^{-4}
$f_{1_{opt}}$ (mm)	:	6.625	$f_{1_{opt}}$ (mm)	:	3.960
ΔBFL_{opt} (mm)	:	40.400	ΔBFL_{opt} (mm)	:	36.979

3.1.4.4 Non-Sequential Mode

The optimized three lens setup for Gaussian illumination was transferred to NSQ mode by the convert to NSC group feature. In the next step, the Gaussian light source, defined in Section 3.1.1.4, was added to the optical system in the NSCE. Based on this light source file, the corresponding MCE settings in NSQ mode can be found in Section 3.1.1.4.

3.1.4.5 Ray Tracing

The ray tracing analysis, discussed in great detail in Section 2.3.2.3, was performed in both operation modes by using the following settings:

Sequential Mode

In this case, the ray tracing analysis was performed for the two developed optical systems, one for each illumination type in SQ mode. For each configuration, specified in the MCE, 10 million rays were launched and recorded at the image surface, located at $z = 100\,\text{mm}$ as displayed in Figure 20a. The resolution of the detector in the GIA interface was set to 201 x 201 pixels. All ray tracing results for both uniform and Gaussian intensity distribution are discussed in Section 4.1.3.1.

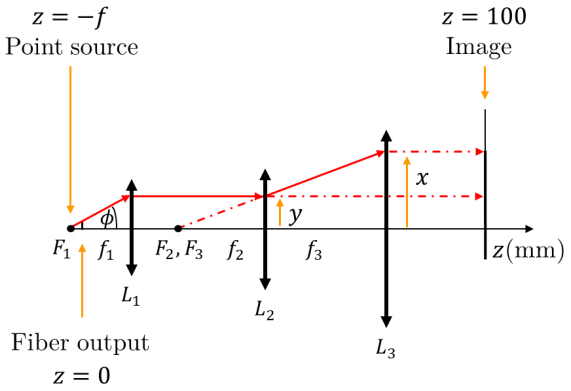

(a) SQ mode.

Non-Sequential Mode

In total, three detectors D_i, each with a resolution of 201 x 201 pixels, were placed in the optical system along the LD propagation axis at (70, 85 and 100) mm as illustrated in Figure 20b. For each configuration, defined in the MCE interface, 10 million analysis rays were drawn from the Gaussian source through the entire optical setup in NSQ mode. All ray tracing results at the detector surfaces are displayed in Section 4.1.3.2.

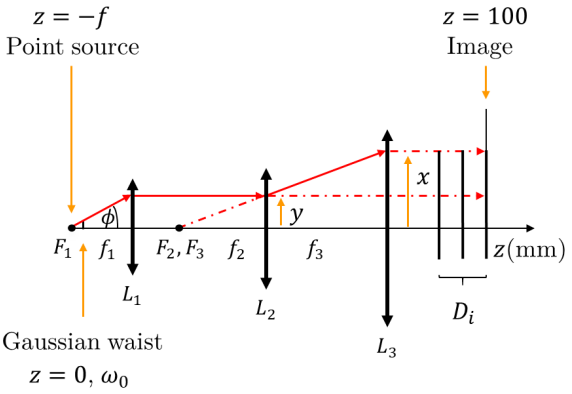

(b) NSQ mode.

Figure 20: Three lens setup: Ray propagation in both modes for ray tracing analysis.

3.1.5 Three Lens Setup B

The introduction of a new mounting concept for the laser windows on the resonant PA cell (Section 3.2.3.2) required a reduction of the window dimensions to $(21.19 \times 14 \times 3)$ mm. This adaptation led to a modification of the effective illuminable area in the PA resonator. Hence, new laser beam dimensions of (20×8) mm were necessary in order to prevent potential light interactions with PA cell material. All other boundary conditions and requirements, defined in Section 3.1.2, are still valid and remain unaffected. In the next step, the previous three lens setup A was adapted by introducing lenses of the same type with different focal lengths in order to satisfy the new beam dimensions. The most essential lens parameter for both uniform and Gaussian illumination are summarized in Tables 10 and 11. This modification procedure only affected the geometric calculations and the optimization process. All other steps of the design process, under consideration of the new lens parameters, are identical to Section 3.1.4 and are therefore not covered. The ray tracing results for SQ and NSQ mode are presented in Sections 4.1.4.1 and 4.1.4.2.

3.1.5.1 Geometric Calculations

Given the fact that the beam dimensions only changed in the x-axis, the adaptation focused only on the magnification power of the beam expansion setup, consisting of lens L_2 and L_3, whereas the collimation lens remained the same. The introduction of a new lens implies a reduction of the corresponding magnification factor M, defined by Equation (2.48), and thus of the final x-dimension at the image surface. According to the starting parameters and the mathematical procedure in Section 3.1.4.1, the following geometrical calculation results were obtained by means of the new lens data.

Geometric Calculation Results:

Uniform illumination			Gaussian illumination $(1/e^8)$		
x (mm)	:	8.546	x (mm)	:	9.259
y (mm)	:	2.706	y (mm)	:	3.920
M_{Dim}	:	3.695	M_{Dim}	:	2.551
M_{FL}	:	3.158	M_{FL}	:	2.362
ΔBFL (mm)	:	35.80	ΔBFL (mm)	:	29.40

Table 10: Three lens setup B: Lens parameters for uniform illumination.

Aspheric condenser lens

Lens	Item (#)	FL (mm)	BFL (mm)	Diameter (mm)	NA	CT (mm)	Material	Coating
Lens 1	ACL1512U	12.0 ± 8%	7.0	15	0.61	8.0	B270	AR-C

Cylindrical lenses

Lens	Item (#)	FL (mm)	BFL (mm)	Length (mm)	Height (mm)	CT (mm)	Material	Coating
Lens 2	LK1037L1	−19.0	−20.3	21.0	19.0	2.0	N-BK7®	AR-C
Lens 3	LJ1430L1	60.0	−56.1	32.0	30.0	5.0	N-BK7®	AR-C

Table 11: Three lens setup A: Lens parameters for Gaussian illumination ($1/e^8$).

Aspheric condenser lens

Lens	Item (#)	FL (mm)	BFL (mm)	Diameter (mm)	NA	CT (mm)	Material	Coating
Lens 1	ACL108U	8.0 ± 8%	4.0	10	0.61	5.8	B270	AR-C

Cylindrical lenses

Lens	Item (#)	FL (mm)	BFL (mm)	Length (mm)	Height (mm)	CT (mm)	Material	Coating
Lens 2	LK1900L1	−25.4	−26.7	18.0	16.0	2.0	N-BK7®	AR-C
Lens 3	LJ1430L1	60.0	−56.1	32.0	30.0	5.0	N-BK7®	AR-C

3.1.5.2 Optimization

In order to satisfy the required boundary conditions, the optimization process focused on the actual lens position of L_1 and L_3 along the propagation axis. The corresponding sequential merit function was defined in the exact same manner as described in Section 3.1.4.3. However, the target values of the REAX and REAY operators were adjusted to the new x- and y-dimensions of the desired beam profile, (10×4) mm respectively. All optimization results for the adapted optical setup are displayed in the following table. The data reveals a subtle improvement of the final beam collimation quality (RMS angular radius) for both illumination types over the previous three lens system.

Optimization Results:

Uniform illumination			Gaussian illumination ($1/e^8$)		
Merit function	:	4.122×10^{-4}	Merit function	:	3.355×10^{-4}
RMS angular radius (rad)	:	6.481×10^{-4}	RMS angular radius (rad)	:	5.275×10^{-4}
$f_{1_{opt}}$ (mm)	:	6.627	$f_{1_{opt}}$ (mm)	:	3.959
ΔBFL_{opt} (mm)	:	36.748	ΔBFL_{opt} (mm)	:	30.471

3.2 Component and Material Selection

This section gives a brief overview of the lens material and AR-C broadband coating. It is followed by the material selection for the laser windows with respect to LT-PEMFC material compatibility and transmission data. The second part of this section focuses on several heating methods of the laser window with respect to functionality and efficiency.

3.2.1 Optical Devices

On the basis of the previous section, aspheric and cylindrical lenses were used for the three lens setup B. All important lens parameters can be found in Tables 10 and 11. Both lens materials, namely optical crown glass (B270) and RoHS-compliant borosilicate crown glass (N-BK7®), show excellent transmission in the visible and near IR portions of the spectrum (350 to 2000) nm as shown in Figure 23. In general, the reflection at the glass/air interface accounts for approximately 4 % of the the total energy, resulting in a total transmission of only 92 % of the incident light at 0 ° incident angle. Fortunately, the application of AR coatings allows a significant reduction of reflectance losses while enhancing transmission within a specific wavelength range. The basic structure consists of stacked layers with various thickness in order to produce destructive interference for the reflected beam rays. In this particular case, the average reflectance of the AR-C coating is less than 0.5 % across the spectral range of (1050 to 1700) nm, as shown in Figure 21. Therefore, an optimal performance is guaranteed within this region for an angle of incidence (AOI) between (0 to 30) °. Apparently, the reflectance increases approximately to 3.6 % for LD three, which is in the order of magnitude of the reflection at glass/air interfaces. Nevertheless, the high disposable optical power still ensures sufficient coupling into the PA cell, so that potential reflectance losses can be considered insignificant.

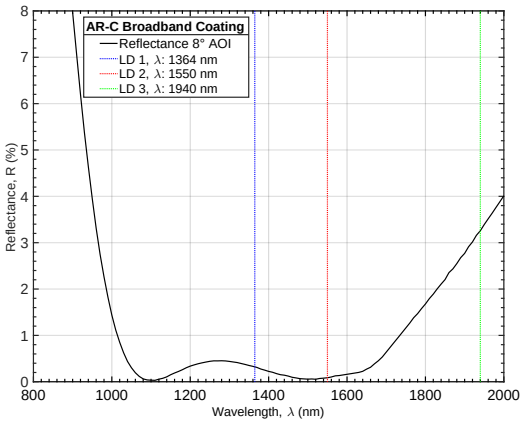

Figure 21: AR broadband coating: Reflectance over wavelength for AOI of 8 degrees.[5]

[5] (2014), Optical AR-C broadband coating specifications, *Thorlabs, Inc.* [Online] Accessed: March, 2018.

3.2.2 Laser Windows

As seen in Figure 32a, two laser windows are attached to the resonant PA cell. The intended integration of the PA sensor system into a LT-PEMFC leads to direct contact with humid environment. The presence of aggressive, humid H_2 may affect the properties of materials (e.g. tensile strength, fracture toughness, etc.), better known as hydrogen embrittlement. Furthermore, the contact with deionized (DI) water can lead to contamination of the FC by system materials with high solubility. Hence, FC material compatibility plays a crucial role for the laser window material selection. A detailed computer-aided-design (CAD) drawing of the laser window can be seen in Figure 22.

Characteristics:

- Window dimensions: $(21.19 \times 14 \times 3)\,\mathrm{mm}$
- High transmission: $(1000 \text{ to } 2000)\,\mathrm{nm}$
- High water resistance
- Chemical and heat resistance
- Durable and minimal aberrations

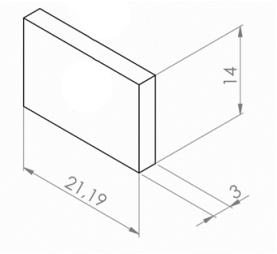

Figure 22: Laser window: CAD illustration.

Based on the database for material compatibility in LT-PEMFCs (*AVL List GmbH*, [94]) and a specific set of requirements, the materials calcium fluoride (CaF_2), magnesium fluoride (MgF_2) and N-BK7® were considered proper candidates. For each candidate, important material characteristics are shown in Table 12. It is mainly based on literature source [43], complemented by *Thorlabs, Inc.*[6] and *Schott AG*[7] data base. The parameters ρ, T_λ, c_p and T_m represent the density, transmission range, specific heat capacity and melting temperature for each material, respectively. In case of N-BK7®, T_m displays the

Table 12: Laser window: Relevant characteristics of multiple optical substrates.

Material	Crystal Structure	ρ ($\mathrm{g/cm^3}$)	T_λ (nm)	c_p (J/(gK))	T_m (K)	Solubility (g/100 mL H_2O)
CaF_2	Cubic	3.18	180 to 8000	0.854	1418	0.0016
MgF_2	Tetragonal	3.15	200 to 6000	1.003	1255	0.013
N-BK7®	Amorphous glass	2.51	350 to 2000	0.858	500	Insoluble

[6] (2014), Optical substrate specifications, *Thorlabs, Inc.* [Online] Accessed: March, 2018.

[7] (2017), Optical glass database, *Schott AG*. [Online] Accessed: March, 2018.

softening temperature. Figure 23 shows the transmission data over wavelength for 10 mm thick substrate of all candidates. Each one of the materials display excellent transmission in the NIR portion of the spectrum. For the final wavelength of 1940 nm, N-BK7® shows a drop in transmission to approximately 88 % as seen in Figure 23. Due to the high LD power, the total power transfer into the PA resonant cell is still sufficient enough. Hence, for a laser window with a thickness of 3 mm, the difference in transmission is negligible due to the high laser powers.

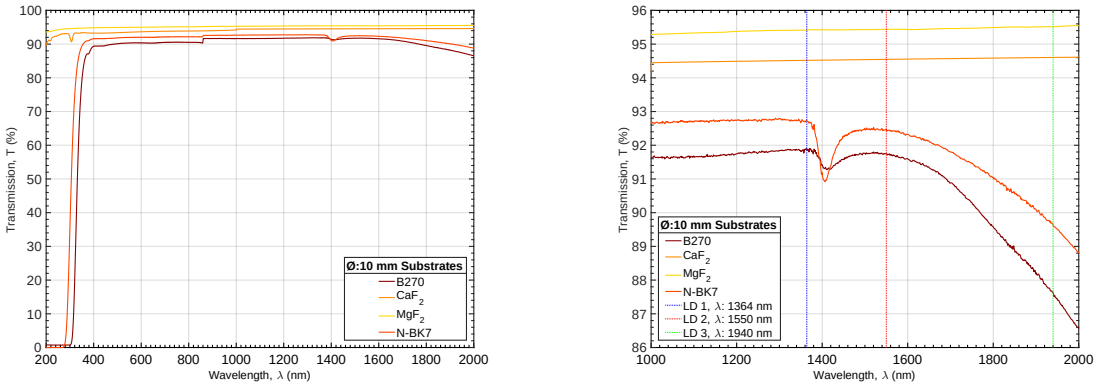

(a) **(b)**

Figure 23: Laser window: (a) Transmission range of optical materials with a thickness of 10 mm[6]. (b) Detailed view of the relevant section of the entire transmission spectrum for the PA measurement.

All materials fulfill the requirements for chemical and heat resistance. Hence, the main criterion was the materials' solubility in water. The harsh environment, especially the aggressive humid H_2, within a FC leads to the conclusion that N-BK7® was the best candidate. In contrast to CaF_2 and MgF_2, the material N-BK7® is no salt and therefore insoluble in water. This guarantees high durability of the laser windows and no risk of potential contamination of the LT-PEMFC.

3.2.3 Heating Concepts

The humid FC environment can lead to little water precipitation on the laser window surface, resulting in possible interaction with the incoming laser beam. In order to minimize these scattering effects and their influence on the measurement quality, several concepts of water precipitation removal were considered for this PA sensor system. The two most promising methods in the framework of LT-PEMFC compatibility will be explained in detail in the next section.

3.2.3.1 Joule Heating

In general, resistive heating describes the generation of heat by passing an electric current through a conductor. The desired energy conversion is based on resistive losses in the material. A popular method is the application of a conducting and transparent indium tin oxide (ITO) thin film onto the laser window surface. This compound, consisting of distinct variable proportions of indium (In), tin (Sn) and O_2, is a a heavily doped n-type semiconductor with a large band gap, high optical transmission in visible and NIR and high reflectance in the IR region, as shown in Figure 77 [40]. In terms of the broad LD wavelength range in the IR region for this particular application, the transmission performance of ITO thin film coated windows are not satisfactory. In order to achieve a trade-off between the power of heating and transmission performance, a more complex ITO thin film coating was designed by different deposition mask techniques. The most promising layout, highlighted in Figure 24, corresponds to an ITO thin film framed laser window with two additional electrodes on opposite sides. Based on the supply voltage, the crucial parameter, resistance R, can be adjusted by the ITO thickness, O_2 content and geometrical shape.[8]The dependency of the power of heating P on the resistance R and the current I is given by Equation (3.3). In addition, the correlation to its geometrical shape, bulk resistivity ρ and sheet resistivity R_s need to be taken into account as well.

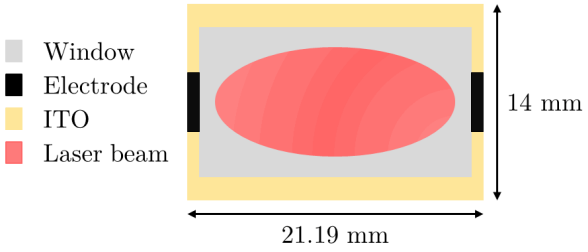

Figure 24: Resistive heating concept: ITO thin film coating with electrodes on laser window.

$$P = I^2 R \tag{3.3}$$

$$R = \rho \frac{L}{Wt} \tag{3.4}$$

$$R = \frac{\rho}{t} \frac{L}{W} \tag{3.5}$$

$$\rho = R_s t \tag{3.6}$$

The parameters L, W and t stand for the length, width and thickness of the ITO thin film coating. Due to the fact that the window dimensions are limited by the mount, an ITO thin film frame is accompanied by a decrease of the effective laser beam illumination area. As a consequence, the laser beam dimensions and the interaction volume within the resonant PA cell are significantly reduced.

[8] *Roland Selic*, (2017), *Piezocryst Advancded Sensorics GmbH*, ITO sputtering deposition.

3.2.3.2 Mount Heating

The implementation of heating cartridges in the laser window mount describes a different approach to remove water precipitates from the laser window surface. A detailed CAD drawing is displayed in Figure 25. As previously mentioned, the hydrogen embrittlement and contamination of the LT-PEMFC by system materials is an essential point for the selection of materials. In general, highly soluble materials, e.g. iron (Fe) or copper (Cu), are not suitable for LT-PEMFC applications. In contact with DI water, Cu and Fe cations can undergo a chemical reaction and create a protective layer on top of the Pt/C catalyst which leads to a reduction of the triple phase zone area, chemical reaction rate, FC performance and lifetime. In addition to excellent FC compatibility, the material must also possess excellent thermal conductivity to allow efficient removal of water droplets. Stainless steel (316L) was considered to be the best candidate due to outstanding strength and corrosion resistance combined with good thermal conductivity. Its wet corrosion resistance is attributed to the presence of a thin oxide film on the metal surface due to the high chromium (Cr) content in the steel alloy [31, 83]. In contrast to resistive heating, there is no variation of the effective illumination area. This method convinces with its functionality and simplicity for this specific application. Hence, the mount heating concept was selected for the removal of water precipitates. The laser windows were attached to the stainless steel mount by thermally conductive epoxy and sealed by thermally resistant O-rings. Two resistive heating cartridges were implemented in the mount on both sides for temperature management. A production tolerance of ± 0.1 mm was considered for the laser window dimensions, as discussed in Appendix B.1.

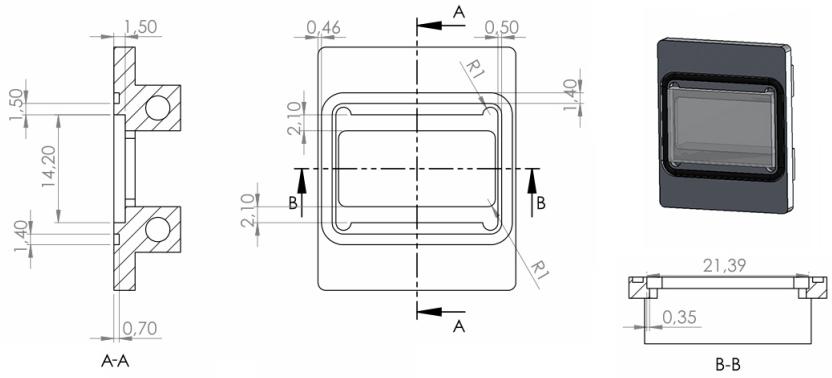

Figure 25: Mount heating concept: CAD drawings of laser window mount including two heating cartridges. Specified dimensions are in mm.[9]

[9] Used with permission of *Benjamin Lang, AVL List GmbH*, (June, 2017).

3.3 Measurement Setup Realization

This section covers the LD adaptations to guarantee similar fiber output for the PA measurement and the 3D rendering results for the optical setup realization. A complete list of all components can be found in Appendix C, Table 24.

3.3.1 Laser Diode Adaptations

Table 2 shows that LD one differs in the fiber and connector type, resulting in a different mode mixing, NA and fiber diameter. In order to simulate and design one optical setup for all three LDs, simplifications were necessary. For the simulation part, the NA and fiber diameter were considered equal size for all LDs, 0.22 and 0.2 mm, respectively. Therefore, a custom MM fiber cable, equipped with FC/PC and SMA connectors, was attached to the fiber coupled LD one by using a FC/PC to FC/PC mating sleeve. The MM fiber was selected according to the fiber specifications (NA, core diameter and wavelength) of the remaining LDs in order to achieve a similar fiber output.

3.3.2 Optical Setup Realization

The complete designing process was achieved by the commercial software *SolidWorks*[10], a solid modeling CAD program. A 60 mm cage system was used as the foundation for both optical setups, uniform and Gaussian illumination respectively. The fiber coupled LDs were individually connected to the optical setup by the SMA fiber adapter plate. Based on the *Zemax* simulation results, the fiber adapter plate and the ACL L_1 were placed in a lens tube for easy integration and removal, followed by two cage plates for the cylindrical lenses L_2 and L_3. The dimensions were based on the optimized three lens setup B, especially the optimized parameters $f_{1_{opt}}$ and ΔBFL_{opt} in Section 3.1.5.2. All important lens parameters can be found in Tables 10 and 11. This compact arrangement enables quick substitution of the lens tubes, one for each illumination type, and adjustment of the lens separation distances. Furthermore, the cage system provides a simple and elegant way to attach the optical system to the PA resonant cell, as shown in Figure 32b. The CAD design results for both illumination types are illustrated in Figures 27 and 28. Both figures display the top view of the cage system with sectional cuts.

[10] (2017), *SolidWorks Premium* (2017), *Dassault Systèmes*. [Software] Accessed: April, 2017.

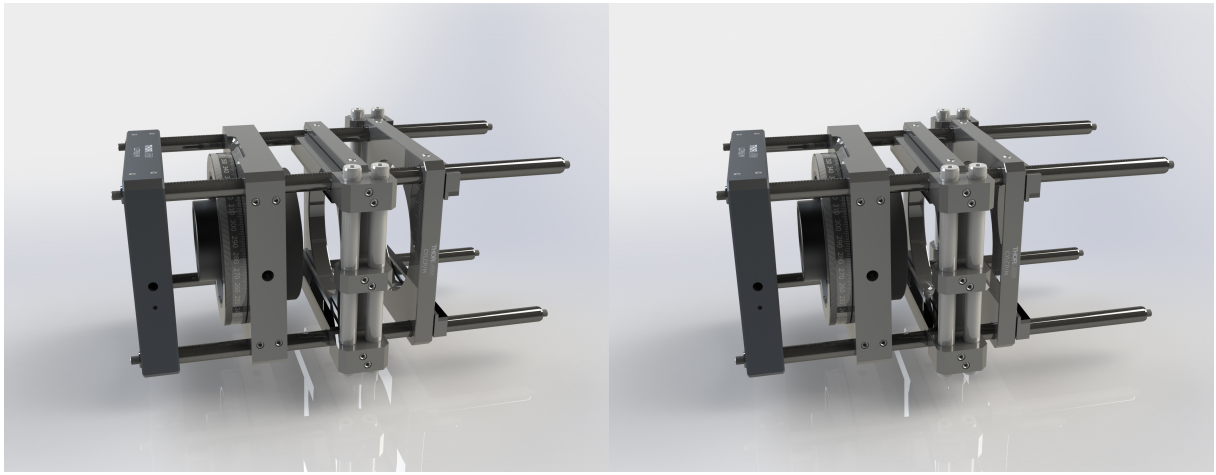

(a) Uniform illumination. **(b)** Gaussian illumination.

Figure 26: Optical setup realization: 3D rendering for both illumination types based on the three lens setup B simulation results in *Zemax*.

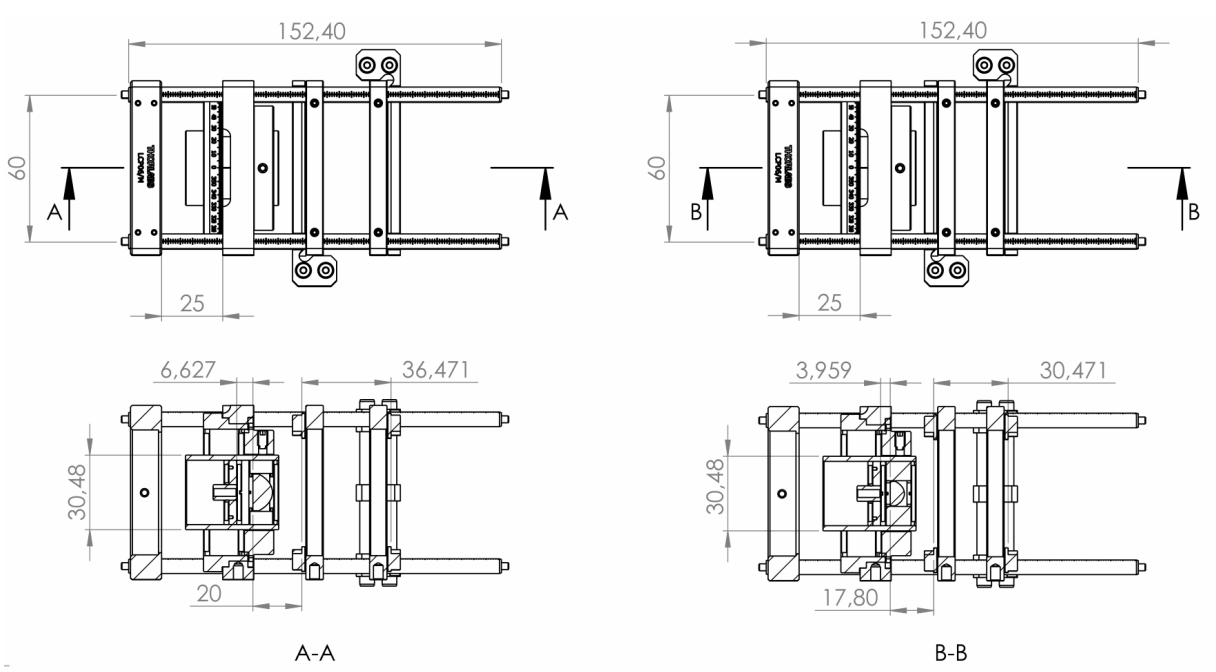

(a) Uniform illumination. **(b)** Gaussian illumination.

Figure 27: Optical setup realization: CAD drawings of the cage system for both illumination types. Specified dimensions are in mm.

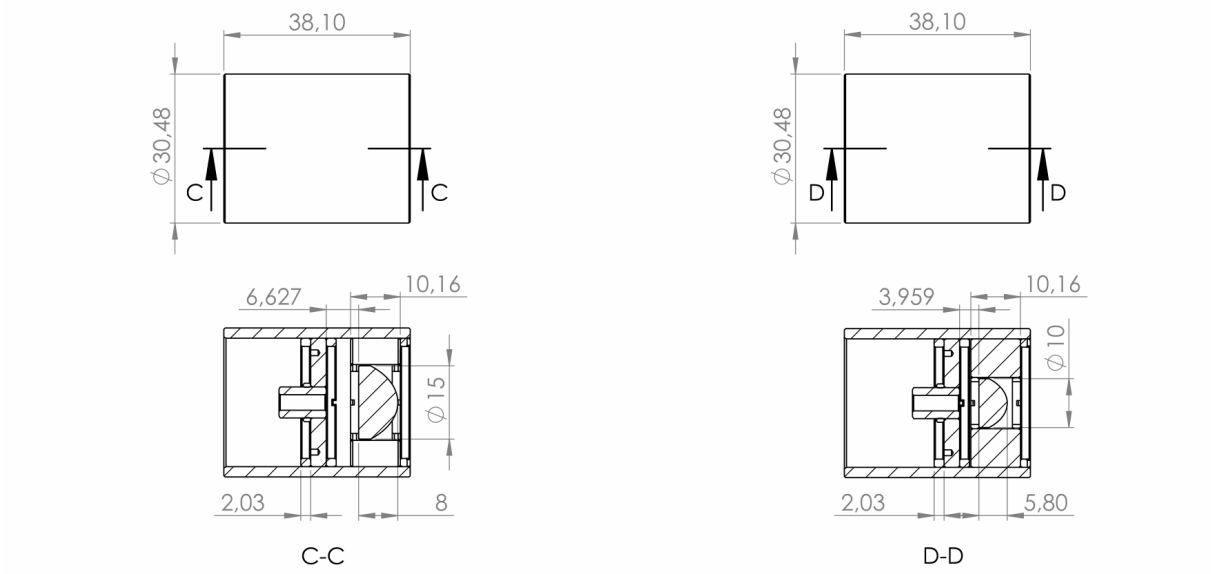

(a) Uniform illumination.

(b) Gaussian illumination.

Figure 28: Optical setup realization: CAD drawings of lens tube for both illumination types. Specified dimensions are in mm.

3.4 Laser Diode Characteristics

This segment includes the first part of the LD characterization measurements, particularly the current-voltage-power (I-V-P) characteristics of each individual LD, provided in Table 2. The employed experimental setup consists of the SMA fiber adapter plate, LMR1/M mount, PM16-401 power meter with thermal sensor and ITC4005 controller. It is noteworthy that the ITC4005 provides the functionality of both LD current regulator and thermoelectric cooler (TEC) controller in one single device. The SMA fiber adapter plate was mounted on the power meter using the LMR1/M mount. Subsequently, each individual fiber coupled LD was consecutively connected to the power meter in order to record the characteristics. In case of LD one, a custom MM fiber with both FC/PC connector on one side and SMA connector on the other was used. More details about the components can be found in Appendix D. For each measurement, the forward current I_f, voltage V and operating temperature T_{op} were adjusted by the ITC4005 controller. Based on the specifications in Table 2, each parameter was altered individually for each LD. In addition, a new variable ΔI_f was introduced, specifying the actual forward current step size. All measurement settings are summarized in Table 13.

Table 13: I-V-P characteristics: Measurement settings for the LD/TEC controller.

	ITC controller				
	$I_{f_{min}}$ (mA)	$I_{f_{max}}$ (mA)	ΔI_f (mA)	V_{max} (V)	T_{op} (°C)
LD 1	0	150	5	6	25
LD 2	0	2400	50	1.5	25
LD 3	0	2500	50	1.7	25

The resulting output power was measured by the power meter using the *Optical Power Meter Utility* software[11]. In order to minimize little power fluctuations of the laser output signal, 30 samples were recorded for each ΔI_f step. Furthermore, the integration time and averaging parameter were set to 1 s and 1 in the corresponding software, respectively. Prior to the actual measurement, the background signal was recorded for 100 counts in total. This procedure was repeated for each individual LD. All measurements were performed at room temperature.

[11] (2017), *Optical Power Meter Utility* (1.0.2), *Thorlabs, Inc.* [Software] Accessed: March, 2017.

Data Analysis

First, the arithmetic mean (AM) and the standard deviation (SD) of the background signal were calculated by Equations (D.8) and (D.9). This value was subtracted from the actual measurement results in order to minimize the background noise. As mentioned above, each ΔI_f step consisted of 30 measurement values. Hence, the AM and SD were determined for each single measurement step. The final I-V-P characteristic results for each fiber coupled LD are shown in Section 4.2. The complete experimental data analysis was achieved in *MATLAB*[12].

3.5 Beam Profile Analysis

This section focuses on the beam profile analysis of the fiber coupled LDs in order to investigate and optimize the actual laser beam shape. As discussed in Section 3.1.2, the divergence and final diameter of the output laser beam play a crucial role for the PA measurement setup. In general, a beam profiler represents an excellent device for a full analysis of complex beam profiles within a certain wavelength range. However, for this particular application the coverage of the entire lasing wavelength range (1000 to 2000) nm by a single device was neither available in the laboratory nor affordable. Therefore, on the basis of several publications [19, 69, 86] two different alternative beam profiling methods (e.g. **scanning slit method** and **knife-edge method**) were considered in more detail with focus on the beam divergence and diameter. Identical to Section 3.4, all tests were performed at room temperature and the experimental data analysis was accomplished in *MATLAB*. A list of all measurement devices used can be found in Appendix D, Table 26.

3.5.1 Validation Tests

A validation test for each individual method was carried out, in order to determine the accuracy and quality of the beam profile analysis results. All validation tests were performed on a *Qioptiq* laser module of the NANO 250 series with a center wavelength of 402 nm and maximum output power of 160 mW. The *NanoControl*[13]user software was used to drive the laser module. For all validation measurements, the laser module was operated in the internal constant power mode with an output power set point of 15 mW.

[12] (2016), *MATLAB* (R2016a), *MathWorks, Inc.* [Software] Accessed: February, 2016.

[13] (2017), *NanoControl* (1.2.3.0), *Qioptiq Photonics GmbH.* [Software] Accessed: April, 2017.

The operating temperature was set to 25 °C. The transmitted power was measured by the power meter using the *Optical Power Meter Utility* software[14]. The reference measurement was achieved by the BC106N beam profiler with the corresponding *Thorlabs Beam* software[15]. The device was used with the 40 dB AR coated attenuation filter.

3.5.1.1 Scanning Slit Method

A more detailed description of the SSM can be found in Section 2.4.2. Two razor blades were used to create the aperture in order to obtain the beam profile. One major drawback of the handmade slit is the final minimum gap size and the accuracy with respect to parallel alignment of the razor blade edges. The average razor blade thickness R_{th} and the slit size S_{th} were determined to be (100.0 ± 0.5) µm and (450.0 ± 0.5) µm, respectively.

Measurement Setup

The principle measurement setup can be seen in Figure 12b. The power meter and the beam profiler were placed at the same distance from the LD. Prior to the actual measurement, the background noise was recorded for 100 counts in total.

Settings:

Background		Measurement	
Counts (#)	: 100	Counts (#)	: 20
Integration time (s)	: 1	Integration time (s)	: 1
Averaging	: 1	Averaging	: 1
		Step size (mm)	: 0.050/0.025
		Range (mm)	: 7.00

Two different step sizes were used for the beam profiling measurement, in order to see the influence on the resolution of the actual beam profile. All settings can be seen in the previous table. 20 samples were taken per measurement increment during the SSM experiment. The reference x- and y-beam profile data was collected by the BC106N beam profiler. Further information can be found in Appendix D.2.2.

[14] (2017), *Optical Power Meter Utility* (1.0.2), *Thorlabs, Inc.* [Software] Accessed: March, 2017.

[15] (2017), *Thorlabs Beam* (6.0.785.2502), *Thorlabs, Inc.* [Software] Accessed: April, 2017.

Data Analysis

SSM experimental data processing included the AM and SD calculations of the background and measurement increment data in accordance with Equations (D.8) and (D.9). Subsequently, the background noise signal was subtracted from the actual measurement data in order to minimize the background noise level. The determination of the Gaussian beam parameters for the experimental and reference data was achieved by:

1. **Nonlinear Least Squares Regression**
   The experimental and reference data were fitted by using the iterative least squares algorithm in accordance with the Gaussian model in Equation (3.7) where a represents the amplitude, b is the centroid (location) and c is related to the peak width.

$$y = a \exp\left[-\left(\frac{x-b}{c}\right)^2\right] \tag{3.7}$$

   The *Cauchy* weight function for robust fitting was implemented in order to minimize the sensitivity to potential outliers. In addition, the 95 % parameter confidence intervals (CIs) as well as the 95 % prediction bounds for a new observation were calculated on the basis of the mean square error (MSE) and the estimated variance-covariance matrix of the fit. Subsequent shape-preserving piecewise cubic interpolation at the two $1/e^2$ points in intensity allowed the determination of the beam diameter $D_i(z)$ and radius $\omega_i(z)$ for both data sets.

According to Section 2.4.2, the measured transmitted power $P(x, z)$ is described by the convolution integral Equation (2.58) for a finite slit size. In order to assess the quality and accuracy of the SSM results, the convolution of the reference data and the slit size was calculated for the x- and y-profile. Based on the pixel size of the sensor surface, (6.45×6.45) µm, a set of different slit sizes were displayed in number of pixels. All results were rounded to the nearest integer less than or equal to the initial value. Convolution and nonlinear regression results for both data sets are discussed in Section 4.3.1.1.

Slit Dimensions:

	(µm)	(Pixel)		(µm)	(Pixel)		(µm)	(Pixel)
Slit 1 :	10	1	Slit 3 :	200	15	Slit 5 :	450	69
Slit 2 :	50	7	Slit 4 :	300	31	Slit 6 :	700	108

3.5.1.2 Knife-Edge Method

Section 2.4.1 discusses the measurement principle in more detail. Regular chrome platinum double edge blades by *Socieété BIC S.A* were used for the beam profiling process.

Measurement Setup

The measurement setup is illustrated in Figure 12a. The beam profiler was placed at the power meter position in order to guarantee the exact same distance from the LD. The background noise was recorded for 100 counts in total. During the KEM experiment, 20 samples were taken per measurement increment over a range of 12 mm.

Settings:

Background		Measurement	
Counts (#)	: 100	Counts (#)	: 20
Integration time (s)	: 1	Integration time (s)	: 1
Averaging	: 1	Averaging	: 1
		Step size (mm)	: 0.25/0.050
		Range (mm)	: 12.00

All settings can be seen in the table above. Instead of the direct measurement of the reference x- and y-profile, the whole 2D laser beam was recorded by the BC106N to obtain more accurate and significant reference data. Subsequent integration over all columns and rows of the 2D beam shape image revealed the x- and y-profile, respectively. This step resulted from the fact that the previously obtained profiles along the x- and y-axis represent only a single row and column of the entire laser beam according to the data specifications, respectively. Further information about the beam profiler can be found in Appendix D.2.2.

Data Analysis

KEM experimental data processing involved the computation of the AM and SD for the background data and for each measurement step according to Equations (D.8) and (D.9). The background level was further minimized by subtracting the background noise signal from the actual measurement data. The reference data analysis is equal to the previously described data analysis of the SSM. However, the determination of both profiles and

Gaussian beam parameters from the KEM experimental data is more complex. Three different approaches were employed to obtain the x- and y-profile from the experimental data. Each method displays the transmitted power $P(x, z)$ at a particular point x in the laser beam.

1. **Nonlinear Least Squares Regression**

   Experimental data fitting of the cumulative Gaussian distribution, derived in Section 2.4.1, was achieved by using the iterative least squares algorithm according to Equation (3.8). The fitting parameters $\omega(z)$, x_0 and P_0 represent the $1/e^2$ beam radius, the center of the laser beam and the maximum transmitted power. The +(-) sign expresses the translation of the razor blade in the negative (positive) x-direction.

$$P(x, z) = \frac{P_0}{2} \left[1 \pm \operatorname{erf}\left(\sqrt{2}\frac{(x - x_0)}{\omega(z)}\right)\right] \tag{3.8}$$

   Again, the *Cauchy* weight function was implemented to reduce the effect of laser fluctuations and outliers on the fitting process. Likewise, the 95 % parameter CIs and the 95 % prediction bounds for a new observation were determined based on the MSE and the estimated variance-covariance matrix of the nonlinear regression. The actual beam shape was obtained by Equation (3.9), the derivative of the fit equation.

$$\frac{\mathrm{d}P(x, z)}{\mathrm{d}x} = \frac{P_0\sqrt{2}}{\sqrt{\pi}\omega} \left[1 \pm \exp\left(\sqrt{2}\frac{(x - x_0)^2}{\omega(z)^2}\right)\right] \tag{3.9}$$

2. **Derivative of Data**

   The second method displays the derivation of the experimental data. The derivative at any data point is given by

$$\frac{\mathrm{d}P}{\mathrm{d}x} = \left[\frac{y_{i+1} - y_i}{x_{i+1} - x_i}\right] \tag{3.10}$$

   where y represents the transmitted power at the translation position x for the i^{th} and $(i + 1)^{th}$ data point, respectively. The associated error $\Delta\,\mathrm{d}P/\,\mathrm{d}x$ was calculated by standard error propagation of measurement uncertainties such as SD of transmitted power and micrometer reading error.

$$\Delta\frac{\mathrm{d}P}{\mathrm{d}x} = (\Delta y_{i+1} + \Delta y_i)\left|\frac{1}{x_{i+1} - x_i}\right| + (\Delta x_{i+1} + \Delta x_i)\left|\frac{y_{i+1} - y_i}{(x_{i+1} - x_i)^2}\right| \tag{3.11}$$

3. Averaged Derivative of Data

In contrast to method two, Equation (3.12) allows for additional smoothing of the derivative at any data point. This was achieved by averaging the derivative of two adjacent data points [69].

$$\left.\frac{\mathrm{d}P}{\mathrm{d}x}\right|_{avg.} = \frac{1}{2}\left[\frac{y_{i+1}-y_i}{x_{i+1}-x_i} + \frac{y_i-y_{i-1}}{x_i-x_{i-1}}\right] \tag{3.12}$$

The parameters x and y represent the translation position and the transmitted power for two adjacent data points, labeled by a subscript i, $i+1$ or $i-1$. Identical to method two, the associated error $\Delta\,\mathrm{d}P/\,\mathrm{d}x|_{avg.}$ was obtained by standard error propagation of measurement uncertainties.

$$\begin{aligned}\Delta\left.\frac{\mathrm{d}P}{\mathrm{d}x}\right|_{avg.} = \frac{1}{2}\Bigg[&(\Delta y_{i+1}+\Delta y_i)\left|\frac{1}{x_{i+1}-x_i}\right| + (\Delta x_{i+1}+\Delta x_i)\left|\frac{y_{i+1}-y_i}{(x_{i+1}-x_i)^2}\right| \\ &+(\Delta y_i+\Delta y_{i-1})\left|\frac{1}{x_i-x_{i-1}}\right| + (\Delta x_i+\Delta x_{i-1})\left|\frac{y_i-y_{i-1}}{(x_i-x_{i-1})^2}\right|\Bigg]\end{aligned} \tag{3.13}$$

3.5.2 Beam Profiling Measurements

On the basis of previous validation test results, the KEM was used for LD characterization measurements due to its accuracy and simplicity. Due to time constraints, this section only considers the beam profile analysis of LD three with a center wavelength of 1940 nm.

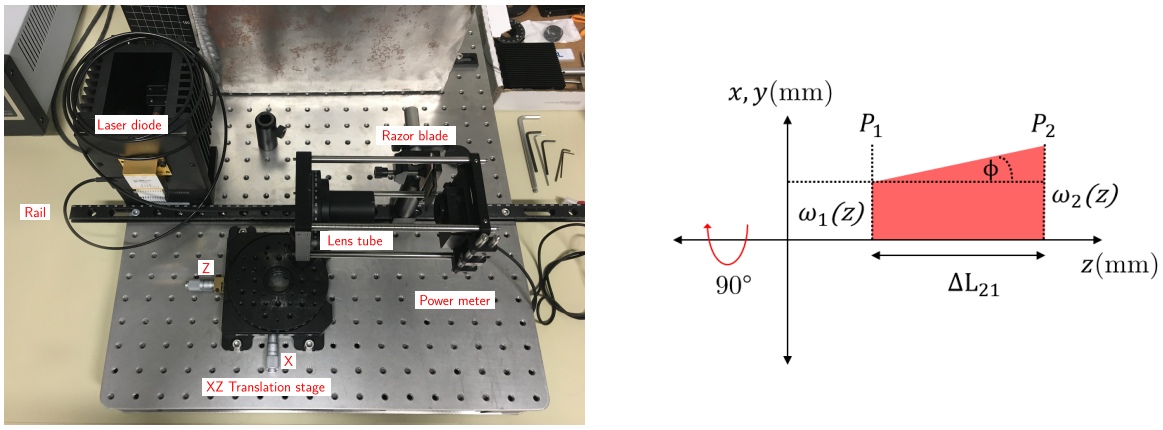

(a) **(b)**

Figure 29: KEM: (a) Experimental setup for the determination of the LD beam profile. (b) Measurement principle for beam waist and divergence along the x- and y-axis.

Figure 29 shows the experimental setup for the beam profiling method. The fiber coupled LD was connected to the SMA fiber adapter plate inside the lens tube which was mounted in the 360 ° rotation mount. The power meter was placed in the cage system, aligned to the center of the fiber adapter plate. The razor blade was aligned perpendicular to the laser propagation direction. All measurements were performed at a constant LD operating temperature T of 25 °C and forward current I_f of 600 mA. As seen in Section 3.5.1.2, the KEM reveals the Gaussian beam parameters $\omega(z)$, x_0 and P_0 at any point along the LD propagation direction. In order to determine the beam divergence, given by Equation (3.14), two measurement points P_i with a separation distance ΔL_{21} along the propagation axis were considered as shown in Figure 29b. This procedure was applied to the x- and y-axis by simply rotating the LD by 90 ° about the local z-axis.

$$\phi = \arctan\left[\frac{\omega_2(z) - \omega_1(z)}{L_2(z) - L_1(z)}\right] \tag{3.14}$$

The corresponding divergence error $\Delta\phi$, given by Equation (3.15), was obtained by standard error propagation. $\Delta\omega_i$ and ΔL_i represent the fit parameter uncertainty, standard error, determined by the estimated variance-covariance matrix of the nonlinear regression and the corresponding reading error along the LD propagation axis.

$$\begin{aligned}\Delta\phi =&(\Delta\omega_2 + \Delta\omega_1)\left|\frac{L_2(z) - L_1(z)}{(L_2(z) - L_1(z))^2 + (\omega_2(z) - \omega_1(z))^2}\right| + \\ &(\Delta L_2 + \Delta L_1)\left|-\frac{\omega_2(z) - \omega_1(z)}{(L_2(z) - L_1(z))^2 + (\omega_2(z) - \omega_1(z))^2}\right|\end{aligned} \tag{3.15}$$

Prior to each measurement, the background signal was recorded for 100 counts. The change in transmitted power was measured by taking 20 samples per translation increment. All settings used in the power meter software are the following:

Settings:[16]

Background		Measurement	
Counts (#)	: 100	Counts (#)	: 20
Integration time (s)	: 1	Integration time (s)	: 1
Averaging	: 1	Averaging	: 1

3.5.2.1 Laser Diode

Measurement Setup

Three different step sizes were used for each measurement, in order to get homogeneously distributed data points along the measurement curve, as seen in Figure 13a. As mentioned above, two measurement points P_1 and P_2, separated by ΔL_{21}, were considered along the propagation axis for the x- and y-profile. The separation distance was adjusted by the translation stage, resulting in a ΔL_i micrometer reading error of 0.005 mm. In total, the KEM was carried out four times.

X-Profile (0 °):		**Y-Profile (90 °):**	
P_1/P_2		P_1/P_2	
Step size (mm)	: 0.25/0.050/0.025	Step size (mm)	: 0.25/0.050/0.025
Range (mm)	: 8.00	Range (mm)	: 8.00
ΔL_{21} (mm)	: 5	ΔL_{21} (mm)	: 5

[16] (2017), *Optical Power Meter Utility* (1.0.2), *Thorlabs, Inc.* [Software] Accessed: March, 2017.

Data Analysis

The data analysis for P_1 and P_2 are identical to the KEM validation test in Section 3.5.1.2. The nonlinear regression model and the corresponding Gaussian beam parameters $\omega(z)$, x_0 and P_0 are given by Equation (3.8). Specific data points in the tails and outliers were excluded from the fitting process. The 95 % prediction bounds for a new observation were estimated using MSE and variance-covariance matrix of the nonlinear iterative least squares regression. Furthermore, the derivative and the averaged derivative of the measured data are given by Equations (3.10) and (3.12). The beam divergence was determined by Equations (3.14) and (3.15). This data analysis procedure was applied to both axes. All results are discussed and illustrated in Figures 62 to 65.

3.5.2.2 Laser Diode with Aspheric Condenser Lens

This section focuses on the collimated LD beam profile based on the optimized three lens setup B in Sections 3.1.5 and 4.1.4.

Measurement Setup

In addition to the previous measurement, the ACL L_1 was mounted in the lens adapter and aligned to the LD with respect to Section 3.1.5.2. Homogeneously distributed data points were achieved by two different step sizes. Again, two measurement points P_1 and P_2 were considered along the LD propagation axis for the x- and y-profile, separated by ΔL_{21} of 40 mm.

X-Profile (0 °):		**Y-Profile (90 °):**	
$\underline{P_1/P_2}$		$\underline{P_1/P_2}$	
Step size (mm) :	0.25/0.050	Step size (mm) :	0.25/0.050
Range (mm) :	7.00	Range (mm) :	7.00
ΔL_{21} (mm) :	40	ΔL_{21} (mm) :	40

The corresponding ΔL_i rail reading error is given by 0.5 mm. Based on the obtained results, the ACL alignment was slightly adjusted in order to improve the final collimation of the LD. The same procedure was employed at different angles (45, 180, 225, 270 and 315) ° for P_i in order to get a more comprehensive beam profile image. In total, 10 additional KEM measurement runs were performed.

Multiple Profiles:

$\underline{P_1/P_2}$

Step size (mm) : 0.25/0.050

Range (mm) : 7.00

ΔL_{21} (mm) : 30

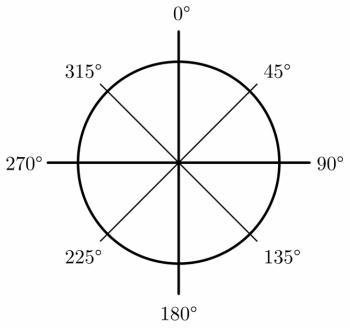

Figure 30: KEM: Beam profile analysis for several angles.

Data Analysis

Due to significant deviations of the experimental data from the ideal Gaussian profile, the obtained results from the nonlinear regression model, given by Equation (3.8) were not satisfying and representative. Hence, only evaluation methods two and three, described in Section 3.5.1.2, were considered for the data analysis. This procedure was applied to each measurement angle for both measurement points P_1 and P_2. In order to determine the beam diameter $D_i(z)$, shape-preserving piecewise cubic interpolation at the two $1/e^2$ points in intensity of both data sets, namely the derivative and averaged derivative, was employed. In this case, the beam divergence was calculated by

$$\phi = 2 \arctan \left[\frac{D_2(z) - D_1(z)}{2(L_2(z) - L_1(z))} \right] \tag{3.16}$$

where $D_i(z)$ is the $1/e^2$ beam diameter at measurement point P_i located at position L_i with the corresponding divergence error $\Delta\phi$ given by

$$\begin{aligned} \Delta\phi = &(\Delta D_2 + \Delta D_1) \left| \frac{4(L_2(z) - L_1(z))}{4(L_2(z) - L_1(z))^2 + (D_2(z) - D_1(z))^2} \right| + \\ &(\Delta L_2 + \Delta L_1) \left| -\frac{4(D_2(z) - D_1(z))}{4(L_2(z) - L_1(z))^2 + (D_2(z) - D_1(z))^2} \right| . \end{aligned} \tag{3.17}$$

The uncertainty of each interpolation point was assumed to be $\pm$ 0.005 mm, resulting in an beam diameter error ΔD_i of $\pm$ 0.01 mm. The parameter ΔL_i corresponds to the reading error along the LD propagation axis. All results are displayed in Figures 66 to 70.

3.6 Validation Test

The first validation test of the PA sensor system was performed in humid environment, the most relevant phase in LT-PEMFC applications. First, this section gives a complete overview of all main components of the final PA experimental setup. Subsequently, the optimization process of the PA signal amplitude is discussed in great detail. In conclusion, the final validation measurement of the PA sensor for LT-PEMFC water balance analysis is considered in depth. All measurements were performed at room temperature.

3.6.1 Photoacoustic Setup

The total PA measurement setup is illustrated in Figure 31. Four specific components can be identified and assigned to either the preconditioning or measurement part. Each component is discussed in more detail in the following section.

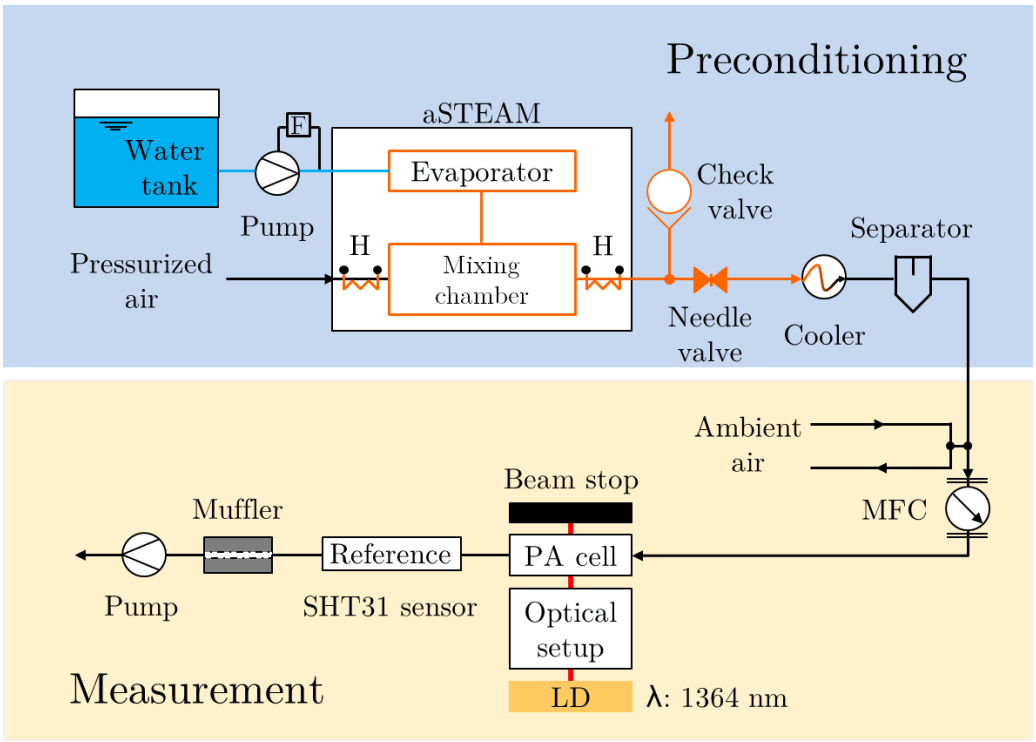

Figure 31: Schematic illustration of the total PA measurement setup subdivided into the preconditioning and the measurement part. Optimized for the PA sensor principle validation in humid environment.

Resonant Photoacoustic Cell

The PA resonator illustrated in Figure 32a represents the centerpiece of the measurement concept. On the inlet side, short concentric resonators (SCRs) were implemented in order to reduce and filter environmental noise. Size and separation distance of the acoustic bandstop filter, i.e SCRs, were tuned to the resonance frequency of the resonator and to maximum transmission loss using *COMSOL*[17]. Silencing on the outlet side was achieved by a muffler at the end of the PA setup. In addition, flow guiding perforates were integrated between the main duct and SCRs. These features lead to a reduction of the flow noise and prevent flow induced pulsation. Literature has highlighted a strong dependence of the geometry and flow regime on the aeroacoustic behavior of wall perforations [50, 111, 116]. The longitudinal resonator section with a resonance frequency of 4660 Hz utilizes the same SCRs for PA resonance enhancement. The microphone was placed on top of the resonator section with the maximum pressure amplitude. As discussed in Section 3.2, N-BK7® laser windows, HT15W heat resistive cartridge heater and PT100 temperature sensors were implemented into the PA mount, displayed in Figure 32a.
Successful validation tests were performed in nitrogen dioxide (NO_2) environment (high absorption cross section σ) for different flow rates using the *Qioptiq* laser module with a center wavelength of 402 nm and maximum output power of 160 mW. The resonator concept was developed and tested by *Benjamin Lang* as part of his dissertation.

Optical Setup

The design and optimization process of the optical setup was discussed in detail in Section 3.1. On the basis of the obtained results, the three lens setup B was selected for the PA measurement. A 3D printed mounting bracket was used to integrate the resonant PA cell into the the 60 mm cage system. According to water absorption characteristics in Figure 5, LD one with a center wavelength of 1364 nm was selected for the humid test atmosphere. The connection to the optical setup was established by the SMA adapter plate, which is part of the cage system as discussed in Section 3.3. The required LD amplitude modulation was realized and controlled by the CompactRIO component.
In order to restrict the propagation of the emitted laser pulses beyond the resonant PA cell, a beam stop was installed right after the PA cell. A schematic illustration of the resonator implementation into the cage system can be seen in Figure 32b. The 60 mm cage plate enables an easy and quick installation of the optical system with the PA resonator.

[17] (2016), *COMSOL Multiphysics Modeling Software* (5.2a), *COMSOL Inc.* [Software] Accessed: January, 2017.

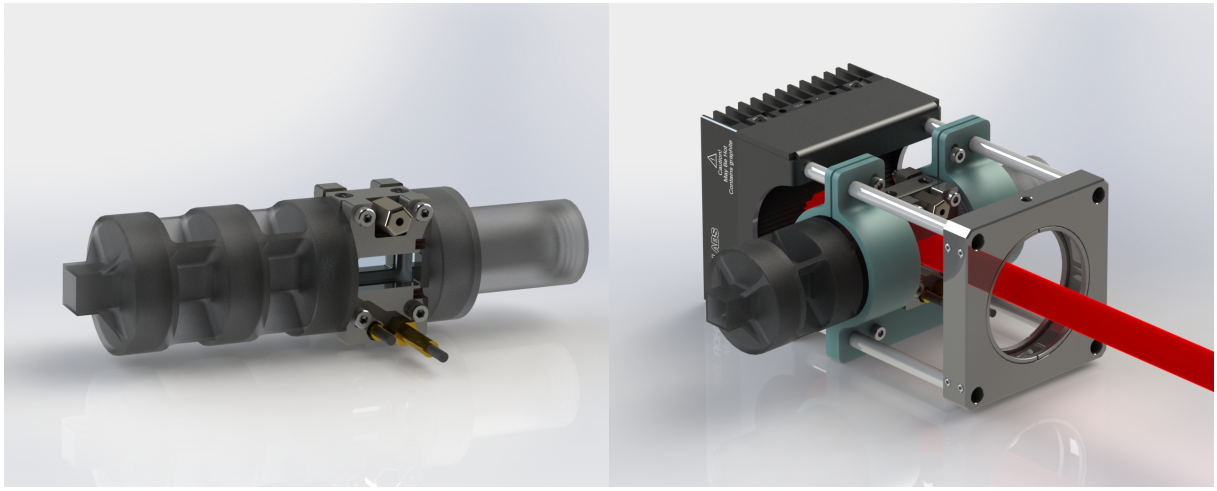

(a) **(b)**

Figure 32: (a) Longitudinal PA resonator with acoustic bandstop filters (SCRs), N-BK7® laser windows, HT15W heat cartridges and PT100 temperature sensors. (b) Illustration of the implementation into the 60 mm cage system used for the optical setup. The red beam represents the collimated incoming laser beam.[18]

Humidifier

The humidity generation was achieved by the aSTEAM direct evaporator, providing a dynamic humidity range of (3 to 97) % rH. The reported stability of each set point is within ± 2 % rH [15]. Implemented electrical heating elements provide the necessary energy for the evaporation process of liquid water. The subsequent mixing chamber combines the generated steam with preheated pressurized air in order to avoid condensation, resulting in a saturated air mixture of about 100 °C. After passing the cooler and liquid separator, the obtained humid air mixture shows a theoretically 100 % rH at room temperature. PTFE tubes were installed to connect the components to the measurement setup due to relatively high temperatures. The flow of humid air through the PA system is controlled by the vacuum pump and the mass flow controller (MFC). The ratio of filtered air and humid air can be adjusted by the needle valve, leading to sufficient fast response time for variations in rH. The humidifier concept was developed and tested by *Anton Buchberger* as part of his master's thesis [15].

Data Acquisition and Signal Processing

The core component is the CompactRIO system, manufactured by *National Instruments Corporation*. It consists of a field-programmable gate array (FPGA) based lock-in amplifier

[18] Used with permission of *Benjamin Lang, AVL List GmbH*, (July, 2017).

and conditioned I/O modules, operated via a *LabVIEW*[19]interface. The LD modulation signal required for the lock-in amplifier and the LD driver ITC4005 is provided by the device itself. The acoustic signal, amplified by a factor 10 using an intermediate amplifier board, is sampled and digitized by the integrated analog I/O module. The necessary supply voltage of the microphone is delivered by the CompactRIO as well. A commercial temperature controller was utilized to manage the heating process of the heat cartridges implemented in the laser window mount as seen in Figure 25. The reference rH measurements were performed using a digital humidity sensor SHT31[20]. The associated accuracy is $\pm$ 2 % rH in accordance with the *Sensirion AG* specifications [97].

3.6.2 Laser Diode Tuning

Prior to the actual PA validation measurement, wavelength tuning was performed on LD one in humid environment. As discussed in Section 2.1.2, the fine-tuning process, driven by LD operating temperature variations, is based on the nature of DFB-LD architecture. In context with the direct correlation of the PA effect to the wavelength dependent absorption cross-section characteristics of the surrounding atmospheric gas mixture, the PA signal amplitude was further maximized for measurements in humid atmosphere.

Measurement Setup

Figure 31 displays the principle measurement setup. LD tuning was performed in ambient air with a rH[21]of (40.0 ± 0.8) % at room temperature. This was realized by simply disconnecting the PTFE tubes from the PA resonant cell. rH was assumed to be constant over the entire duration of the tuning process. The window temperature was regulated to 50 °C and maintained constant throughout the entire measurement process by the temperature controller. On the basis of the specified LD operating temperature of 25 °C in the data sheet, an interval of (25 ± 5) °C with a step size ΔT of 1 °C was examined for the maximum PA signal. Subsequently, the PA signal and phase were recorded with higher resolution in the vicinity of the previously obtained PA peak, starting from (25 to 29) °C with a ΔT of 0.1 °C. The variation of the LD operating temperature T_{op} was controlled by the ITC4005 laser driver.

[19] (2017), *LabVIEW* (2017), *National Instruments Corporation.* [Software] Accessed: April, 2017.

[20] (2017), *Sensor Viewer* (2.84), *Sensirion AG.* [Software] Accessed: June, 2017.

[21] Measured by the humidity sensor SHT31 with USB evaluation kit (EK-H5), *Sensirion AG.*

All necessary CompactRIO input parameters for the LD amplitude modulation signal and lock-in amplifier are displayed in the table below. In total, 200 samples were recorded for each temperature set point.

Settings CompactRIO:

LD amplitude modulation		Lock-in	
Frequency (Hz)	: 4660	Frequency (Hz)	: 4660
Amplitude (V)	: 0.05	Integration time (s)	: 1
Offset (V)	: 0.05	Sampling rate (Hz)	: 10
Duty cycle (%)	: 50	Time (s)	: 20

Data Analysis

Data analysis focused on the SD and AM calculations according to Equations (D.8) and (D.9) for each temperature set point. The obtained PA signal was compared to the atmospheric gas mixture absorption data given by the HITRAN [22]database [34]. All results are displayed in Section 4.4.1.

3.6.3 Photoacoustic Measurement

On the basis of LD tuning results, the parameter T_{op} was adjusted from 25.0 °C to 26.9 °C in order to maximize the PA signal. Identical to the LD tuning experiment, the window temperature was regulated to 50 °C throughout the entire measurement process by the temperature controller.

Measurement Setup

As previously discussed, Figure 31 shows the complete PA measurement setup for a humid environment. The PA signal and phase were recorded at different rH set points over a range of (5 to 85) %. The variation in rH was controlled by the opening position of the needle valve, as seen in Figure 31. At every single measurement point, a transient time of two minutes was specified in order to obtain relatively constant rH value within the resonator. In total, 13 measurement points were randomly spread over the rH interval to further investigate the PA sensor sensibility and correlation to a variation in rH. Simultaneously to the PA measurement, the rH was measured by the reference sensor SHT31.

[22] HITRAN *on the Web*, USA model, mean latitude, summer, H=0 [41]. [Online] Accessed: March, 2018.

In order to guarantee a constant rH set point, a delay time of about two minutes was considered in between each PA measurement step. The transient time of the humid system was dynamically controlled by the humidity sensor, and extended if necessary to obtain constant conditions. All parameters for the humidity generation and reference measurement can be found in the table below. The CompactRIO settings are almost identical to the LD tuning experiment. Only the lock-in measuring time was reduced to approximately 10 s.

Settings:

Humidifier			Humidity sensor SHT31		
Vacuum pump (L/min)	:	25	Integration time (s)	:	1
Water pump (mL/min)	:	10	Time (s)	:	10
Pressurized air (bar)	:	3			
aSTEAM evaporator (°C)	:	120			
aSTEAM mixer (°C)	:	100			

Data Analysis

SD and AM calculations according to Equations (D.8) and (D.9) were performed on PA and reference rH measurement results. The correlation of the PA signal and the rH set point was further investigated by a quadratic fit in a least-square sense in *MATLAB*. The fit model displays a second degree polynomial function with the fitting parameters a, b and c as seen in Equation (3.18).

$$y(x) = ax^2 + bx + c \tag{3.18}$$

In addition, the 95 % prediction interval half-widths for new observations were calculated based on the polynomial error estimation. All results are discussed in more detail in Section 4.4.2.

CHAPTER 4

Results and Discussion

This chapter presents the obtained ray tracing results of the optical system for the PA measurement, followed by the I-V-P characterization findings of all three fiber coupled LDs and subsequent extensive discussion of the beam profiling analysis of LD three. Ultimately, the outcome of the final validation test of the PA measurement in humid environment is addressed in great detail.

4.1 Optical Setup

This section covers the ray tracing results in SQ and NSQ mode for the optimized light source, two lens and three lens system based on the calculations and simulation settings explained in Section 3.1. In detail, the irradiation distribution of the 2D beam profile as well as the irradiation along the x- and y-axis at the image surface are considered and discussed in great depth. In case of the 2D beam profile, the ray tracing results with the largest beam dimensions (configuration three) were used as a representation for the others. The corresponding boundary conditions for the optical setup and the LD parameters can be found in Section 3.1.2 and Table 2, respectively.

4.1.1 Light Source Modeling

The optimized light source model described in Section 3.1.1 is valid for both illumination types. The geometric concept shown in Figure 14 is validated by the optimization results of distance f. All ray tracing results at the image surface for both illumination types

are illustrated in Figures 33 to 37. Further information about ray tracing settings can be found in Section 3.1.1.5. The simulation results in SQ and NSQ mode represented the starting point for both optical concepts, namely two lens and three lens setup.

4.1.1.1 Sequential Mode

Figure 33 shows the irradiance distribution of the 2D beam profile at the image surface for both illumination profiles in SQ mode. The corresponding normalized irradiance along the x- and y-axis at the image surface is illustrated in Figures 34 and 35 respectively. Each figure displays the ray tracing results of all three configurations, defined in the MCE in Section 3.1.1.2. Supplementary curve smoothing can be achieved by increasing the analysis ray number even further in *Zemax*. On the basis of the defined entrance pupil in the SE interface, only rays within the system aperture are considered for the ray tracing process. In case of Gaussian illumination, the edge of the entrance pupil represents the $1/e^2$ point in intensity. Hence, the low intensity part is not considered during the ray tracing process in SQ mode. Further information about the definition of the system aperture in SQ mode can be found in Section 3.1.1.2. The final beam diameter $\varnothing$ in both axes at the image surface was determined by the operands REAX and REAY. As a consequence of the symmetric light source model, the dimensions in the x- and y-axis are identical for all configurations as seen in Figures 34 and 35. Due to the absence of optical devices in the beam path, the ray tracing process shows no effect on the recorded power and efficiency at the image surface. All obtained parameters for both illumination types are summarized in Table 14.

Table 14: Light source: Ray tracing results at the image surface in SQ mode for both illumination types.

	Uniform/ Gaussian illumination				
	λ (nm)	$\varnothing_x/2$ (mm)	$\varnothing_y/2$ (mm)	Power (W)	Efficiency (%)
CF 1	1364	1.228	1.228	0.02	100
CF 2	1550	1.228	1.228	0.6	100
CF 3	1940	1.228	1.228	0.2	100

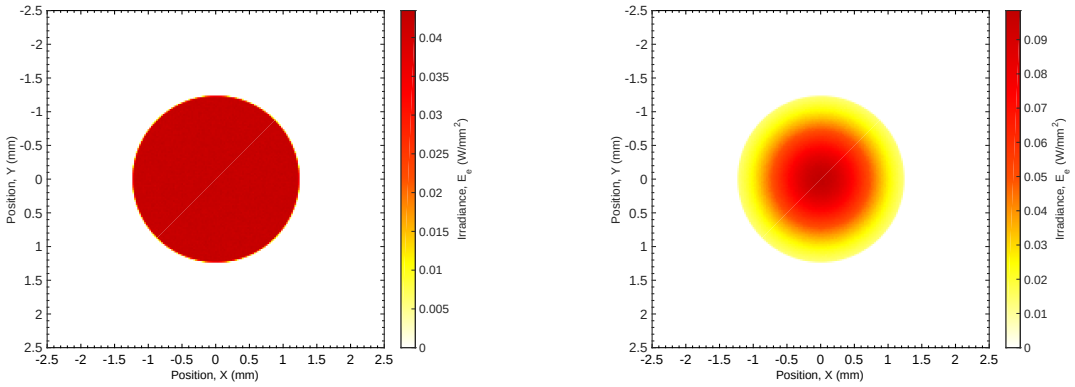

(a) Uniform illumination. **(b)** Gaussian illumination.

Figure 33: Light source: Irradiance distribution of the 2D beam profile at the image surface for both illumination types with respect to configuration three in SQ mode.

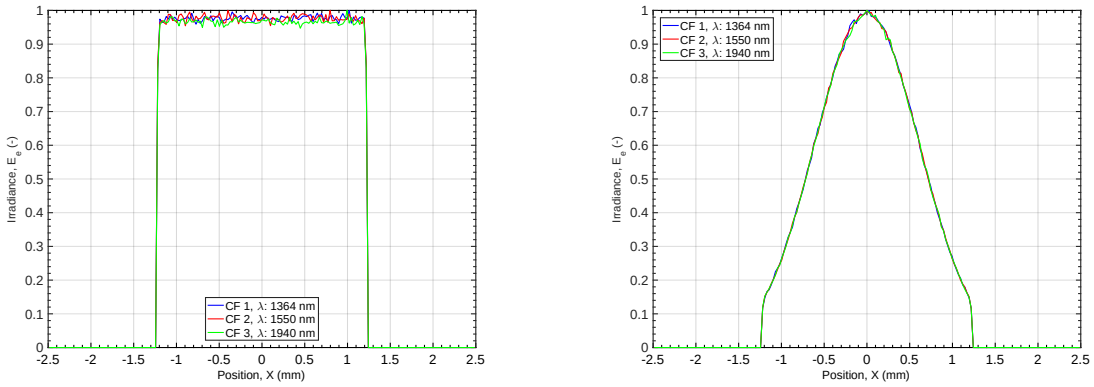

(a) Uniform illumination. **(b)** Gaussian illumination

Figure 34: Light source: Normalized irradiance along the x-axis at the image surface for all configurations with respect to both illumination types in SQ mode.

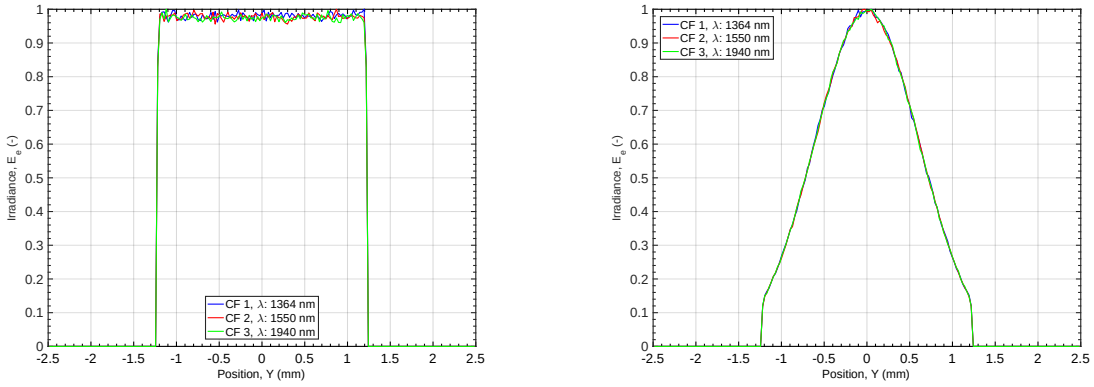

(a) Uniform illumination. **(b)** Gaussian illumination.

Figure 35: Light source: Normalized irradiance along the y-axis at the image surface for all configurations with respect to both illumination types in SQ mode.

4.1.1.2 Non-Sequential Mode

A Gaussian source was defined in NSQ mode by using the paraxial Gaussian beam calculation results of the light source model in SQ mode as shown in Table 5. Further information about the exact model transfer to NSQ mode and the geometrical illustration of the light source in NSQ mode for ray tracing can be found in Section 3.1.1.4. The irradiance distribution of the 2D beam profile at the image surface for configuration three is displayed in Figure 36. The corresponding normalized irradiance profile in the x- and y-direction at the image surface for all configurations is illustrated in Figure 37. It is apparent from this figure, that the ray tracing operations in NSQ consider the entire Gaussian intensity profile instead of a limited fraction within the pre-defined entrance pupil in SQ mode. Subsequently, the final beam radius in the x- and y-axis at the image surface and the power efficiency of the optical setup are displayed for each configuration in Table 15. As expected, the obtained beam dimensions in the x- and y-axis are the exact same at the image surface for all three configurations in NSQ mode.

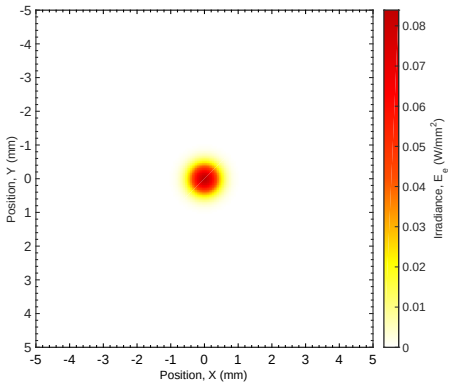

Figure 36: Light source: Irradiance distribution of the 2D beam profile at the image surface for Gaussian illumination with respect to configuration three in NSQ mode.

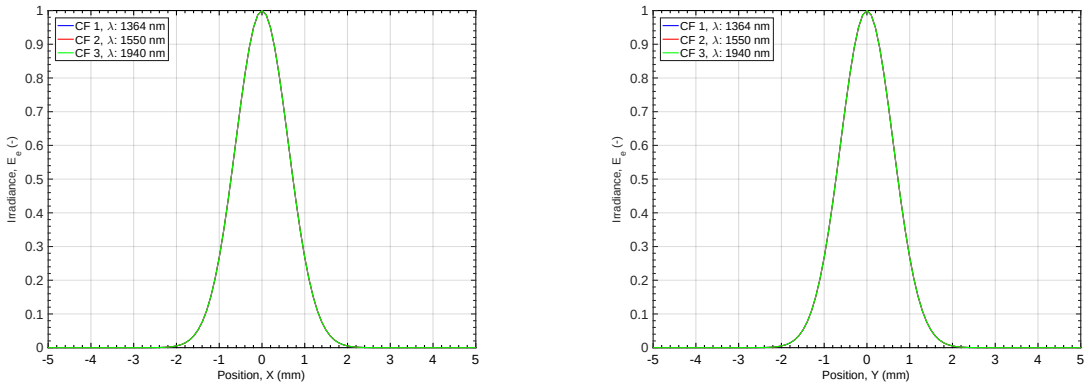

(a) X-axis. **(b)** Y-axis.

Figure 37: Light source: Normalized irradiance along both axes at the image surface for all configurations with respect to Gaussian illumination in NSQ mode.

Table 15: Light source: Ray tracing results at the image surface in NSQ mode for Gaussian illumination.

	Gaussian illumination				
	λ (nm)	$\varnothing_x/2$ (mm)	$\varnothing_y/2$ (mm)	Power (W)	Efficiency (%)
CF 1	1364	2.757	2.757	0.02	100
CF 2	1550	2.757	2.757	0.6	100
CF 3	1940	2.757	2.757	0.2	100

4.1.2 Two Lens Setup

Based on the geometrical concept, developed in Section 3.1.3, the optimized two lens setup is valid for both illumination types in SQ mode. Figures 38 to 45 present the obtained ray tracing results at the image surface. Important lens parameters can be found in Table 7.

4.1.2.1 Sequential Mode

Figure 38 illustrates the irradiance distribution of the 2D beam profile at the image surface for both illumination profiles. In addition, the normalized irradiance profile along the x- and y-direction at the image surface is displayed in Figures 39 and 40, respectively. Each figure consists of two sub figures in order to compare the ray tracing results for both illumination distributions. Identical to the light source, the corresponding beam diameter $\varnothing_i$ at the image surface was determined by using the operands REAX and REAY. The optimized RMS angular radius is 2.03×10^{-3} rad, equivalent to 1.16×10^{-1} °, as discussed in Section 3.1.3.3. All ray tracing results are summarized in Table 16. The obtained x- and y-profile of the final beam shape at the image surface, combined with the evaluated beam diameter suggests that the boundary conditions of Section 3.1.2 are satisfied for both uniform and Gaussian illumination in SQ mode.
However, closer inspection of the ray tracing data revealed several difficulties, e.g efficiency and beam diameter dependence on wavelength and intensity spikes at the edge of the beam shape, that required further investigation. The efficiency drop for each configuration is primarily based on the lens material N-BK7® and AR-C coating. On the basis of the transmission characteristics of N-BK7®, displayed in Figure 23, a decrease in efficiency is expected towards higher wavelengths. Furthermore, the AR-C coating is significantly less effective for configuration three, as discussed in Section 3.2.

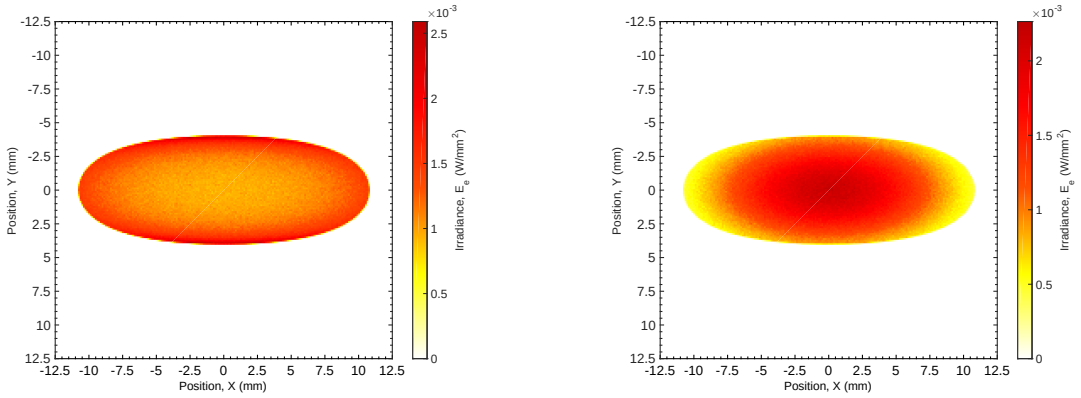

(a) Uniform illumination. **(b)** Gaussian illumination.

Figure 38: Two lens setup: Irradiance distribution of the 2D beam profile at the image surface for both illumination types with respect to configuration three in SQ mode.

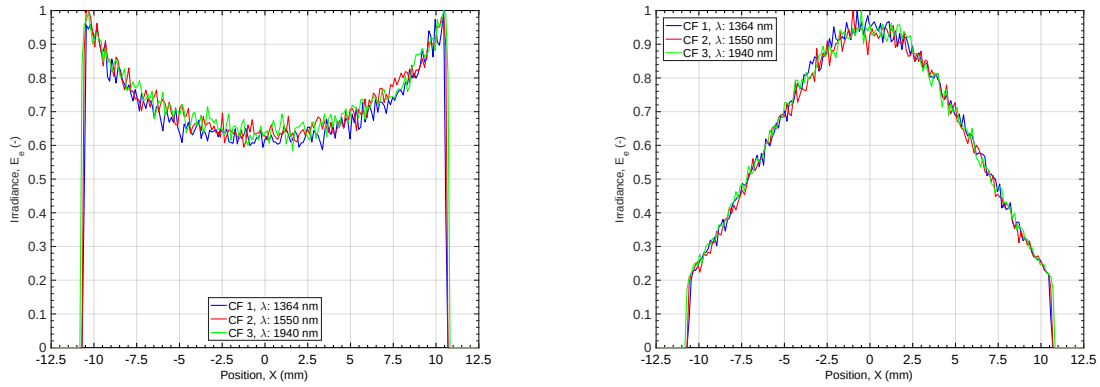

(a) Uniform illumination. **(b)** Gaussian illumination

Figure 39: Two lens setup: Normalized irradiance along the x-axis at the image surface for all configurations with respect to both illumination types in SQ mode.

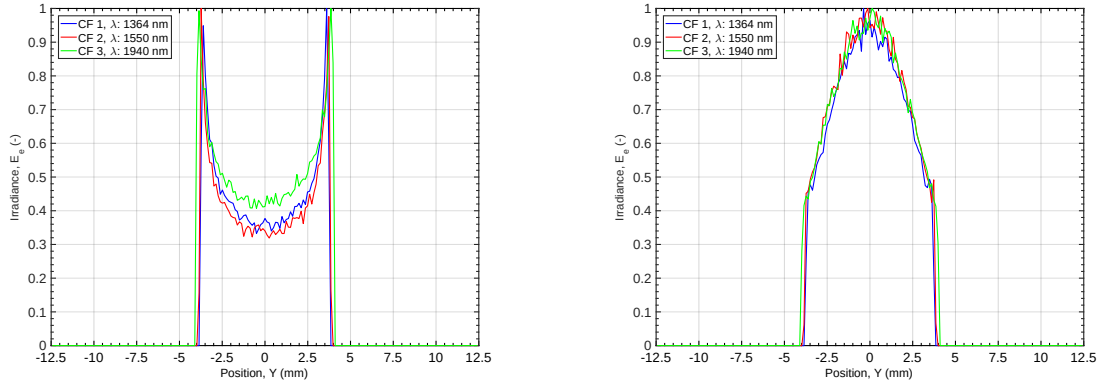

(a) Uniform illumination. **(b)** Gaussian illumination.

Figure 40: Two lens setup: Normalized irradiance along the y-axis at the image surface for all configurations with respect to both illumination types in SQ mode.

The second phenomenon can be linked to to the inverse proportional relationship between the wavelength and the index of refraction for N-BK7®. In general, the nominal focal length for all optical devices used are specified at the design wavelength of 587.6 nm[23]. Due to this inverse proportionality, the actual focal length magnifies with increasing wavelength resulting in an enlargement of the beam diameter at the image surface for each configuration. This behavior can be seen in all obtained ray tracing results, illustrated in Figures 39 and 40 and Table 16.

Further analysis clarified that primarily the total number of analysis rays and the image position have an impact on the existence of the intensity spikes at the edge of the entrance pupil at the image surface for uniform illumination. An increase in total number of rays and in the separation distance between the light source and the image surface leads to a more pronounced intensity feature. By moving the lenses closer to the light source, this feature can be slightly reduced at the expense of the collimation quality. Hence, it seems more likely that this feature is linked to ray tracing limitations in *Zemax*, e.g. total number of rays hitting the edge of the lens, than to actual crucial problems for the final PA setup. However, the most striking aspect of the two lens setup is the high sensitivity to the actual lens position of L_1 and L_2. As a result of the highly divergent MM fiber output, a minimal change in the placement of the optical devices along the propagation axis can result in a significant change in the final beam diameter and collimation quality.

Table 16: Two lens setup: Ray tracing results at the image surface in SQ mode for both illumination types.

	Uniform/ Gaussian illumination				
	λ (nm)	$\varnothing_x/2$ (mm)	$\varnothing_y/2$ (mm)	Power (W)	Efficiency (%)
CF 1	1364	10.56	3.727	1.969×10^{-2}	98.43
CF 2	1550	10.62	3.809	5.907×10^{-1}	98.45
CF 3	1940	10.74	4.000	1.760×10^{-1}	88.01

[23] (2014), Plano-convex cylindrical lenses, N-BK7®, *Thorlabs, Inc.* [Online] Accessed: February, 2018.

4.1.2.2 Non-Sequential Mode

Further information about the NSQ setup transfer can be found in Section 3.1.3.4. Table 5 displays all Gaussian source settings and parameters in NSQ mode. The irradiance distribution of the final 2D beam profile at the image surface for configuration three is illustrated in Figure 41. In accordance with the beam profile, the normalized irradiance in linear and log scale is presented in Figures 42 and 43, respectively. Each figure compares the obtained beam profile along the x- and y-direction at the image surface for all configurations.

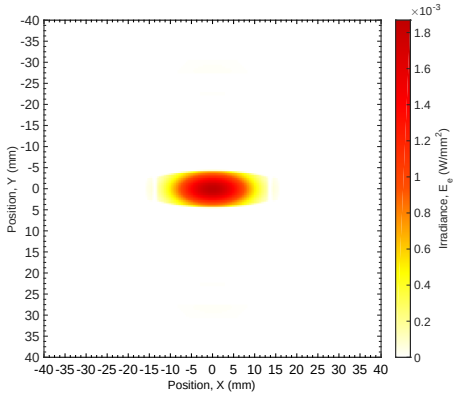

Figure 41: Two lens setup: Irradiance distribution of the 2D beam profile at the image surface for Gaussian illumination with respect to configuration three in NSQ mode.

The data revealed the appearance of several low intensity side peaks in close proximity to the central irradiance peak in both axes. These intensity feature might be caused by considering the whole Gaussian intensity profile in NSQ. Further investigation was accomplished by placing a detector D_i right after each lens, illustrated in Figure 18b. The obtained normalized irradiance in log scale along the x-axis at detector surface D_2 and the y-axis at detector surface D_1 is illustrated in Figure 44. It clearly shows that the low intensity part of the Gaussian profile is not collimated by lens L_1 and L_2 and therefore diverges over distance.

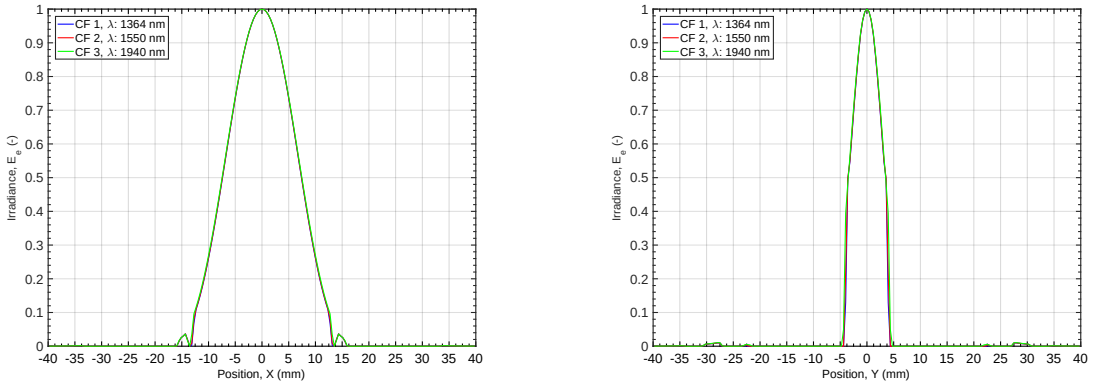

(a) X-axis. **(b)** Y-axis.

Figure 42: Two lens setup: Normalized irradiance along both axes at the image surface for all configurations with respect to Gaussian illumination in NSQ mode.

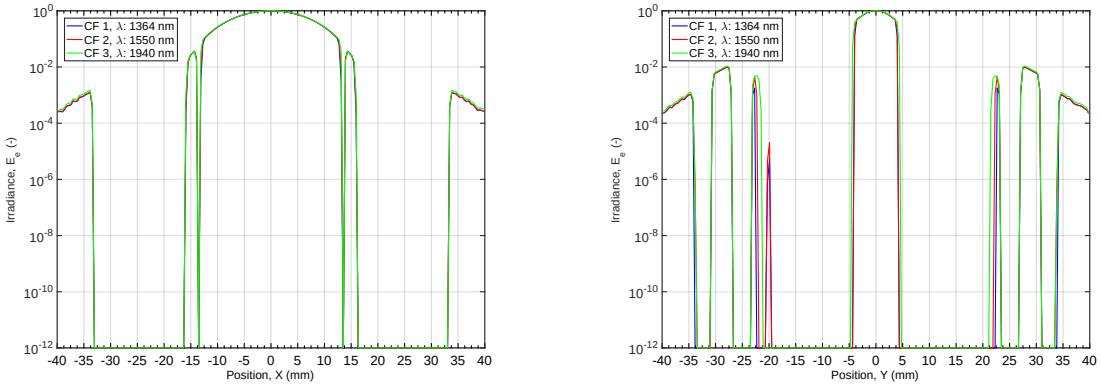

(a) X-axis. **(b)** Y-axis.

Figure 43: Two lens setup: Normalized irradiance in log scale along both axes at the image surface for all configurations with respect to Gaussian illumination in NSQ mode.

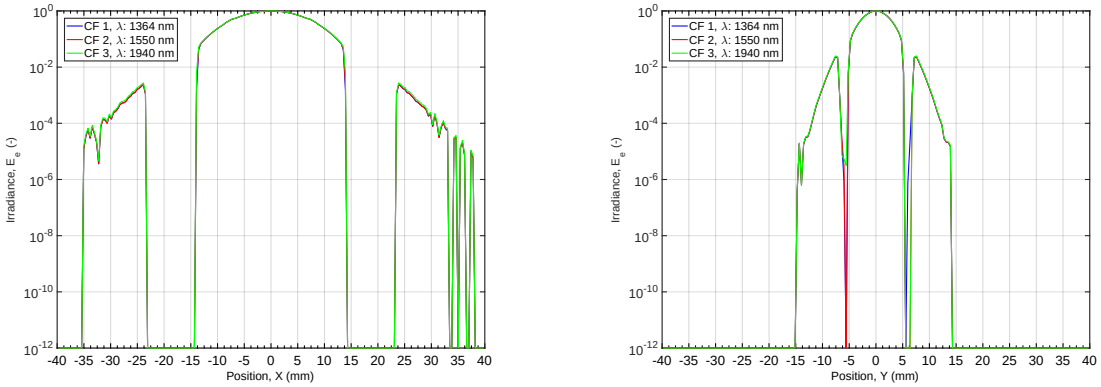

(a) X-axis. **(b)** Y-axis.

Figure 44: Two lens setup: Normalized irradiance in log scale along the x-axis at detector surface D_2 and the y-axis at detector surface D_1 for all configurations with respect to Gaussian illumination in NSQ mode.

Each figure reveals the identical behavior for each configuration in NSQ mode. Together these results indicate that the intensity side peaks can be primarily related to low intensity cut-offs along the x- and y-axis and reflections within the optical setup, caused by the implemented lenses. Furthermore, the ray tracing process showed geometrical errors for each configuration. They are mainly based on the fact that the whole Gaussian intensity profile is considered for ray tracing in contrast to SQ mode, which only considers rays within the pre-defined entrance pupil. The energy loss for each configuration is shown in Table 17. Marginal rays R_i get either reflected, transmitted or do not hit the lens at all. As described in Section 3.1.1.5, all rays are saved in a database.

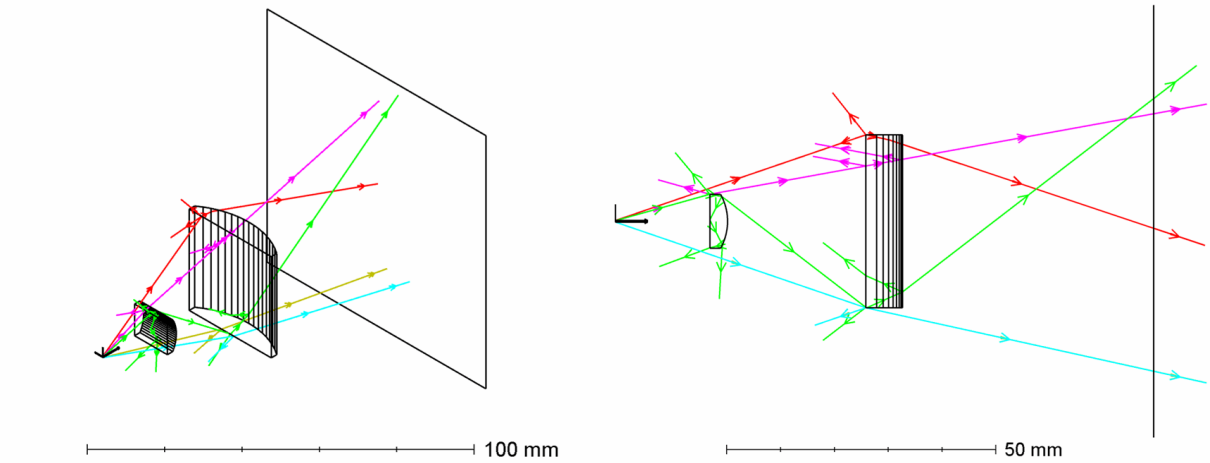

(a) Isometric illustration of geometric error rays.

(b) Geometric error rays in the y-z plane.

Figure 45: Two lens setup: Geometric error ray analysis for all configurations with respect to Gaussian illumination in NSQ mode.

Error Rays:

- R_1: Reflection on L_1 and L_2
- R_2: Missed L_1; Reflection on L_2
- R_3,R_5: Missed L_1 and L_2
- R_4: Multiple reflections on L_2

Figure 45 shows a collection of error rays R_i propagating through the two lens system. All ray tracing results are listed in Table 17. It is apparent from this data that the total energy loss E_L, caused by geometrical errors, is still insignificantly small in comparison to the total power output. Considering the whole Gaussian intensity profile, the parameters $\varnothing_x/2$ and $\varnothing_y/2$ represent the beam radius in the x- and y-axis at $1/e^{11}$ point in intensity, respectively. Especially for the x-axis, the boundary conditions regarding the intensity at the resonator edge are not fulfilled. The low intensity cut-offs may interact with the resonant PA cell material and have a negative influence on the final PA measurement.

Table 17: Two lens setup: Ray tracing results at the image surface in NSQ mode for Gaussian illumination.

	Gaussian illumination						
	λ (nm)	$\varnothing_x/2$ (mm)	$\varnothing_y/2$ (mm)	Peak Intensity (W/mm^2)	Power (W)	Efficiency (%)	Energy Loss (W)
CF 1	1364	16.16	4.289	2.230×10^{-4}	1.952×10^{-2}	97.61	6.659×10^{-8}
CF 2	1550	16.25	4.321	6.551×10^{-3}	5.858×10^{-1}	97.64	2.035×10^{-6}
CF 3	1940	16.26	4.729	1.869×10^{-3}	1.749×10^{-1}	87.44	3.314×10^{-7}

In conclusion, the two lens setup is not satisfying for this specific application with all its boundary conditions. The energy cut-offs may interact with the resonant PA cell, which would have a negative impact on the measurement quality. Furthermore, the reflections of marginal rays and the high sensitivity to the lens position with regard to the collimation quality also affects the final measurement setup. In order to minimize the energy cut-offs for Gaussian illumination, an extended intensity profile, $1/e^8$ beam diameter, needs to be considered for the geometrical calculations and subsequently for the lens selection. The previous calculation based on the $1/e^2$ beam diameter is not sufficient. This leads to better collimation of the low intensity parts. Further increase in resilience and collimation quality can be achieved by an additional ACL.

On the basis of all ray tracing results, the next step was focused on the design of the three lens setup. Further information about the three lens setup can be found in Section 3.1.4.

4.1.3 Three Lens Setup A

This section shows the ray tracing results for the three lens setups developed in Section 3.1.4. As previously discussed, the extended Gaussian intensity profile was considered for the geometrical calculations in order to minimize the energy cut-offs with respect to the Gaussian illumination. Subsequently a better optimization of the low intensity parts was achieved. For each illumination type, one optical setup was designed. Important lens parameters can be found in Tables 8 and 9 for uniform and Gaussian intensity distribution, respectively.

4.1.3.1 Sequential Mode

The irradiance distribution of the 2D beam profile at the image surface for uniform and Gaussian illumination is illustrated in Figure 46. The corresponding normalized irradiance along the x- and y-axis at the image surface for all configurations is displayed in Figures 47 and 48, respectively. Each figure presents the ray tracing results for both uniform and Gaussian ($1/e^8$) illumination in SQ mode. Again, the final beam diameter $\varnothing_i$, power and efficiency were determined based on the obtained data. All important ray tracing results at the image surface for each configuration can be found in Table 18. A closer look reveals that all boundary conditions, defined in Section 3.1.2, are fulfilled for both illumination types in SQ mode. Especially, the fact that even the low intensity parts of the Gaussian profile are collimated ensures zero intensity at the PA cell edge as pictured in Figures 47 and 48. The decrease in efficiency is primarily caused by the light interaction with the lens material and the AR-C coating characteristics, as extensively discussed in Section 4.1.2. The transmission data for both lens materials, B270 and N-BK7®, is shown in Figure 23.

Table 18: Three lens setup A: Ray tracing results at the image surface in SQ mode for both illumination types.

	Uniform illumination				Gaussian illumination ($1/e^8$)			
	$\varnothing_x/2$ (mm)	$\varnothing_y/2$ (mm)	Power (W)	Efficiency (%)	$\varnothing_x/2$ (mm)	$\varnothing_y/2$ (mm)	Power (W)	Efficiency (%)
CF 1	10.70	2.573	1.961×10^{-2}	98.03	10.66	3.123	1.960×10^{-2}	98.00
CF 2	10.77	2.641	5.903×10^{-1}	98.39	10.82	3.293	5.902×10^{-1}	98.37
CF 3	10.90	2.793	1.721×10^{-1}	86.06	11.16	3.668	1.720×10^{-1}	86.01

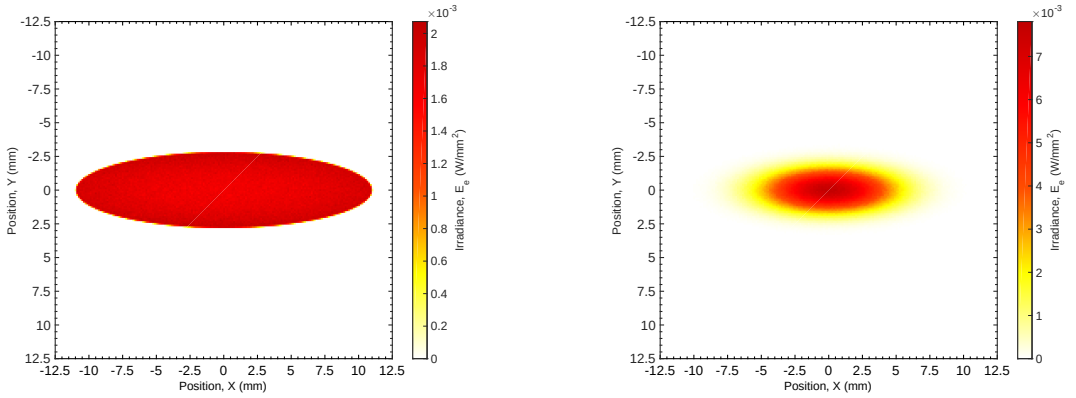

(a) Uniform illumination. **(b)** Gaussian illumination ($1/e^8$).

Figure 46: Three lens setup A: Irradiance distribution of the 2D beam profile at the image surface for both illumination types with respect to configuration three in SQ mode.

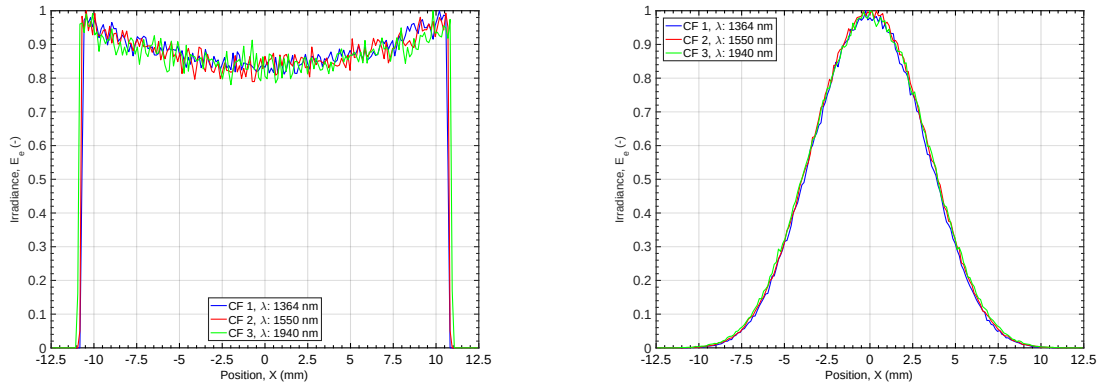

(a) Uniform illumination. **(b)** Gaussian illumination ($1/e^8$).

Figure 47: Three lens setup A: Normalized irradiance along the x-axis at the image surface for all configurations with respect to both illumination types in SQ mode.

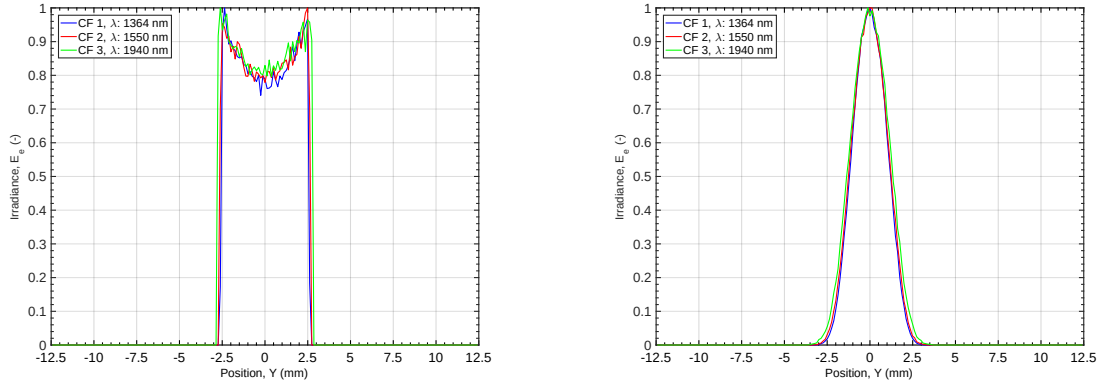

(a) Uniform illumination. **(b)** Gaussian illumination ($1/e^8$).

Figure 48: Three lens setup A: Normalized irradiance along the y-axis at the image surface for all configurations with respect to both illumination types in SQ mode.

As mentioned in the previous Section 4.1.2.1, the focal length shift directly affects the final beam dimensions for each configuration. Hence, a slight increase in beam diameter towards higher wavelengths can be seen in Figures 47 and 48. In contrast to the two lens system, the implementation of an additional collimation lens reduced the divergence and the marginal rays for the beam expanding part of L_2 and L_3. Therefore, the appearance of intensity spikes at the edge of the entrance pupil for uniform illumination was further reduced due to a more convergent laser beam. Moreover, the overall resilience to the lens position was dramatically improved, resulting in a higher collimation quality and lower error susceptibility. The optimized RMS angular radius is 1.10×10^{-3} rad and 5.40×10^{-4} rad, equivalent to $6.30 \times 10^{-2}\,^{\circ}$ and $3.09 \times 10^{-2}\,^{\circ}$, for uniform and Gaussian illumination, respectively. Further information can be found in Section 3.1.4.3.

4.1.3.2 Non-Sequential Mode

Figure 49 displays the irradiance distribution of the 2D beam profile at the image surface for configuration three. The corresponding normalized irradiance in log scale along both axes is illustrated in Figure 50. It consists of the overlay of ray tracing results at the image surface for all three configurations. In comparison to the two lens setup, the obtained x- and y-profile are free from low intensity cut-offs and potential reflection within the optical system, ensuring a significantly better collimation of the entire Gaussian profile. The little spikes at the edge of the irradiance profile in Figure 50 are simply caused by the small number of locally incident analysis rays during the ray tracing process. Hence, this low resolution feature can be considered insignificant for future application in PA measurements. Nonetheless, additional smoothing can be achieved by increasing the total number of emitted rays at the expense of computation time. It is noteworthy that the ray tracing process showed no geometrical errors, resulting in zero energy loss for all configurations.

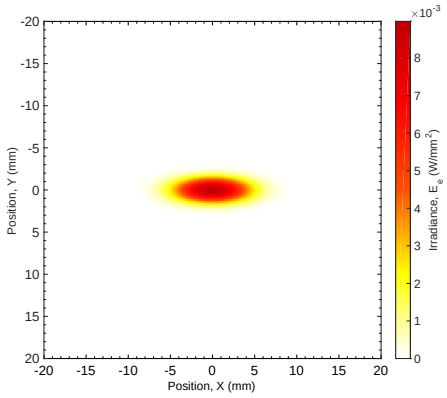

Figure 49: Three lens setup A: Irradiance distribution of the 2D beam profile at the image surface for Gaussian illumination with respect to configuration three in NSQ mode.

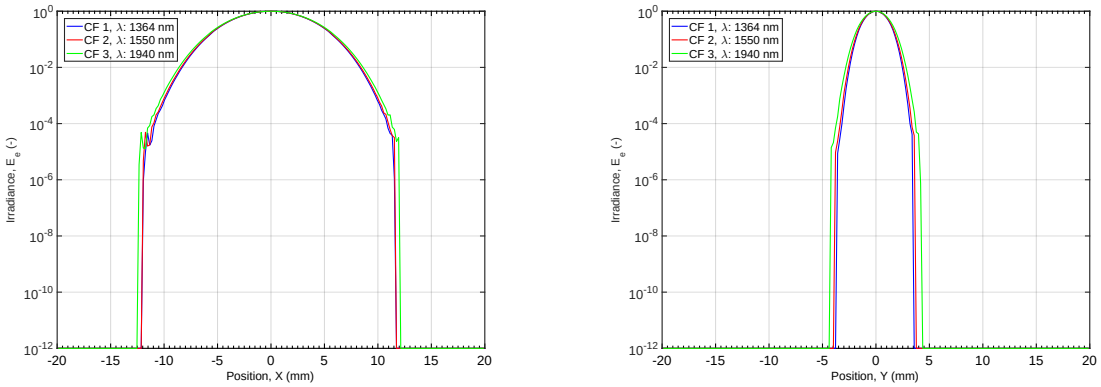

(a) X-axis. **(b)** Y-axis.

Figure 50: Three lens setup A: Normalized irradiance in log scale along both axes at the image surface for all configurations with respect to Gaussian illumination in NSQ mode.

All ray tracing results at the image surface in NSQ mode are displayed in Table 19. Identical to the two lens system, the parameter $\varnothing_i$ represents the beam diameter in the x- and y-axis at the $1/e^{11}$ point in intensity of the Gaussian intensity profile. As a consequence of the previous results in Section 4.1.2, the collimation of the entire intensity profile plays a decisive role alongside the beam dimensions and the potential intensity at the edge of the resonant PA cell in order to minimize the influence on the PA measurement. Although the final beam dimension in the x-axis at the image surface slightly exceeds the boundary conditions in Section 3.1.2, the effective intensity at the edge of the beam profile is extremely low (10^{-4}) and the influence on the PA measurement can be neglected. As discussed in Section 4.1.2, the difference in efficiency between the configurations can be related to the lens material and AR-C coating properties. Supporting transmission characteristics for both lens materials, namely B270 and N-BK7®, are illustrated in Figure 23. Compared to the two lens setup results in NSQ mode, summarized in Table 17, the deviation in efficiency and power at the image surface is negligible.

Table 19: Three lens setup A: Ray tracing results at the image surface in NSQ mode for Gaussian illumination.

	Gaussian illumination ($1/e^8$)						
	λ (nm)	$\varnothing_x/2$ (mm)	$\varnothing_y/2$ (mm)	Peak Intensity (W/mm^2)	Power (W)	Efficiency (%)	Energy Loss (W)
CF 1	1364	11.86	3.632	1.181×10^{-3}	1.950×10^{-2}	97.49	0.0
CF 2	1550	11.93	3.880	3.393×10^{-2}	5.871×10^{-1}	97.85	0.0
CF 3	1940	12.31	4.329	8.977×10^{-3}	1.716×10^{-1}	85.81	0.0

In conclusion, the three lens setup is superior to the two lens concept for this particular application. The final optical setup for uniform or Gaussian illumination is well-collimated, exhibits no intensity cut-offs, shows high efficiency and fulfills the boundary conditions defined in Section 3.1.2.

4.1.4 Three Lens Setup B

As discussed in Section 3.1.5, the previous three lens setup was adapted in order to incorporate the new boundary conditions with respect to the laser beam dimensions. All important lens parameters are displayed in Tables 10 and 11 for uniform and Gaussian illumination, respectively.

4.1.4.1 Sequential Mode

Figure 51 illustrates the irradiance of the 2D beam profile at the image surface for both illumination profiles. The normalized irradiance along the x- and y-axis at the image surface for all configurations can be seen in Figures 52 and 53, respectively. Again, each figure provides the ray tracing results for both uniform and Gaussian ($1/e^8$) illumination in SQ mode. Identical to previous sections, all important ray tracing parameters at the image surface for each configuration are summarized in Table 20. All together, these results confirmed that the optical setup meets the adapted boundary conditions, discussed in Section 3.1.5, for both illumination types in SQ mode. Based on the fact that the lens material and the AR-C coating remained the same, Table 20 shows similar results for the beam efficiency and power at the image surface compared to the original three lens setup A. The data confirms the observed increase in beam diameter towards higher wavelengths. A more detailed discussion can be found in the previous Section 4.1.3.

Table 20: Three lens setup B: Ray tracing results at the image surface in SQ mode for both illumination types.

	Uniform illumination				Gaussian illumination ($1/e^8$)			
	$\varnothing_x/2$ (mm)	$\varnothing_y/2$ (mm)	Power (W)	Efficiency (%)	$\varnothing_x/2$ (mm)	$\varnothing_y/2$ (mm)	Power (W)	Efficiency (%)
CF 1	8.413	2.570	1.960×10^{-2}	98.02	7.893	3.124	1.960×10^{-2}	98.00
CF 2	8.473	2.639	5.903×10^{-1}	98.39	8.038	3.294	5.902×10^{-1}	98.36
CF 3	8.605	2.790	1.721×10^{-1}	86.05	8.359	3.669	1.720×10^{-1}	86.00

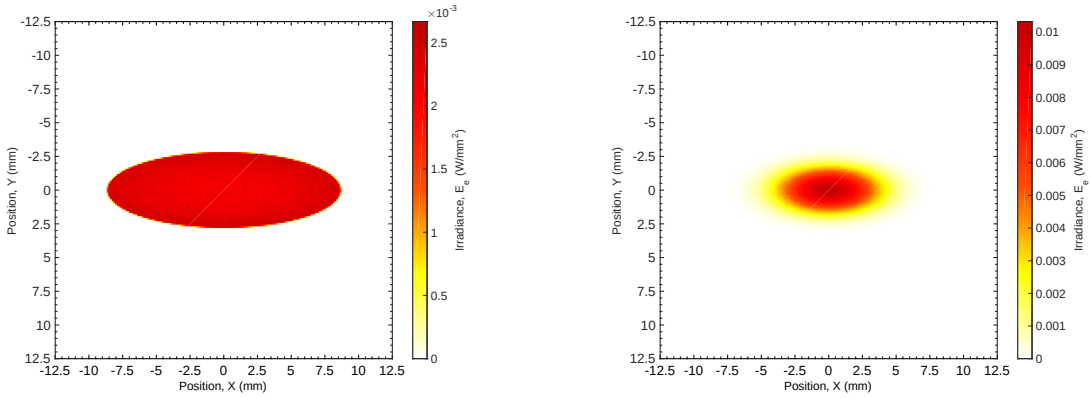

(a) Uniform illumination. **(b)** Gaussian illumination ($1/e^8$).

Figure 51: Three lens setup B: Irradiance distribution of the 2D beam profile at the image surface for both illumination types with respect to configuration three in SQ mode.

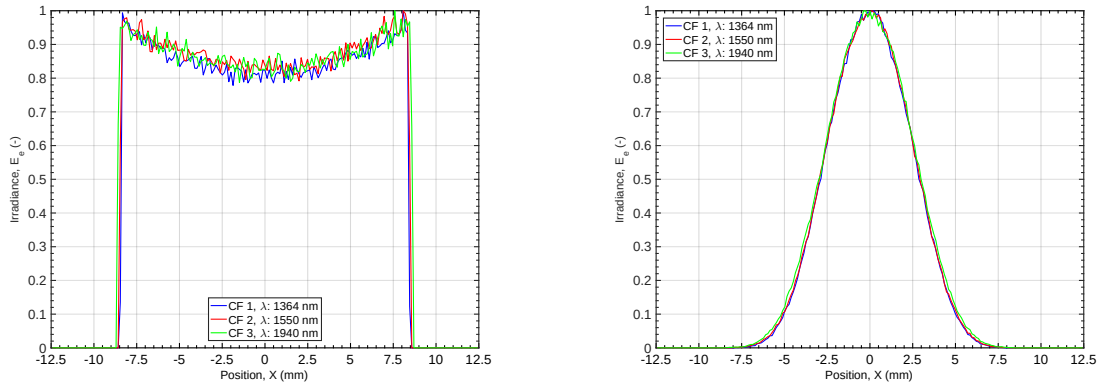

(a) Uniform illumination. **(b)** Gaussian illumination ($1/e^8$).

Figure 52: Three lens setup B: Normalized irradiance along the x-axis at the image surface for all configurations with respect to both illumination types in SQ mode.

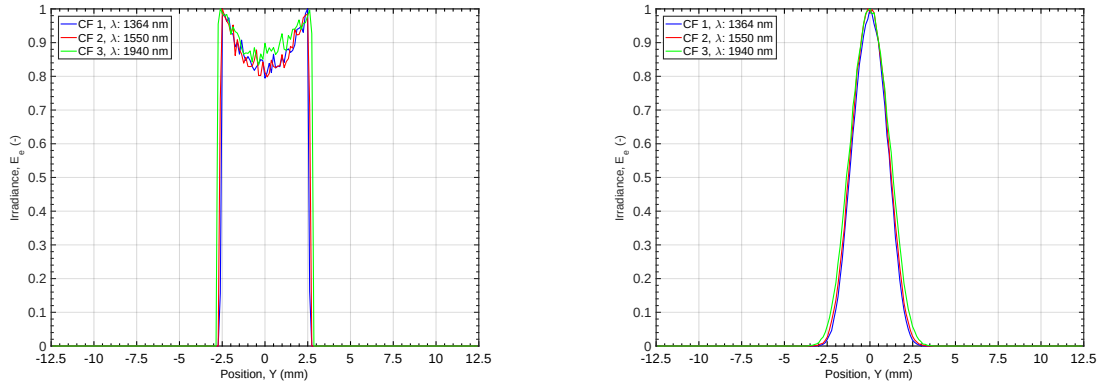

(a) Uniform illumination. **(b)** Gaussian illumination ($1/e^8$).

Figure 53: Three lens setup B: Normalized irradiance along the y-axis at the image surface for all configurations with respect to both illumination types in SQ mode.

For this case, an optimized RMS angular radius of 6.481×10^{-4} rad and 5.275×10^{-4} rad, equivalent to $3.71 \times 10^{-2}\,^{\circ}$ and $3.02 \times 10^{-2}\,^{\circ}$, was obtained for uniform and Gaussian illumination, respectively. Further information can be found in Section 3.1.5. In comparison with the previous three lens setup, a subtle improvement of the final beam collimation quality and resilience to the lens position was achieved for both illumination types.

4.1.4.2 Non-Sequential Mode

Figure 54 displays the irradiance distribution of the 2D beam profile at the image surface for configuration three. In addition, the normalized irradiance in log scale along the x- and y-axis at the image surface is provided in Figure 55. It is apparent that the ray tracing results show neither intensity side peaks nor low intensity cut-offs in any of the configurations. As discussed in Section 4.1.3.2, the little spikes at the edge of the irradiation profile in Figure 55 are a consequence of the small number of locally incident analysis rays and are not relevant for future PA measurements. Identical to the three lens setup A, no geometrical errors occurred during the ray tracing process, resulting in zero energy loss for all three configurations. Table 21 provides all important ray tracing results at the image surface in NSQ mode. In this case, the parameter $\varnothing_i$ describes the beam diameter at the $1/e^{11}$ point in intensity for Gaussian illumination.

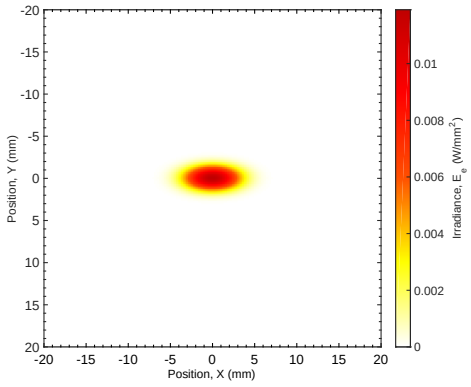

Figure 54: Three lens setup B: Irradiance distribution of the 2D beam profile at the image surface for Gaussian illumination with respect to configuration three in NSQ mode.

Table 21: Three lens setup B: Ray tracing results at the image surface in NSQ mode for Gaussian illumination.

	Gaussian illumination ($1/e^8$)						
	λ (nm)	$\varnothing_x/2$ (mm)	$\varnothing_y/2$ (mm)	Peak Intensity (W/mm^2)	Power (W)	Efficiency (%)	Energy Loss (W)
CF 1	1364	8.899	3.653	1.559×10^{-3}	1.950×10^{-2}	97.49	0.0
CF 2	1550	8.956	3.884	4.527×10^{-2}	5.871×10^{-1}	97.85	0.0
CF 3	1940	9.257	4.378	1.190×10^{-2}	1.716×10^{-1}	85.80	0.0

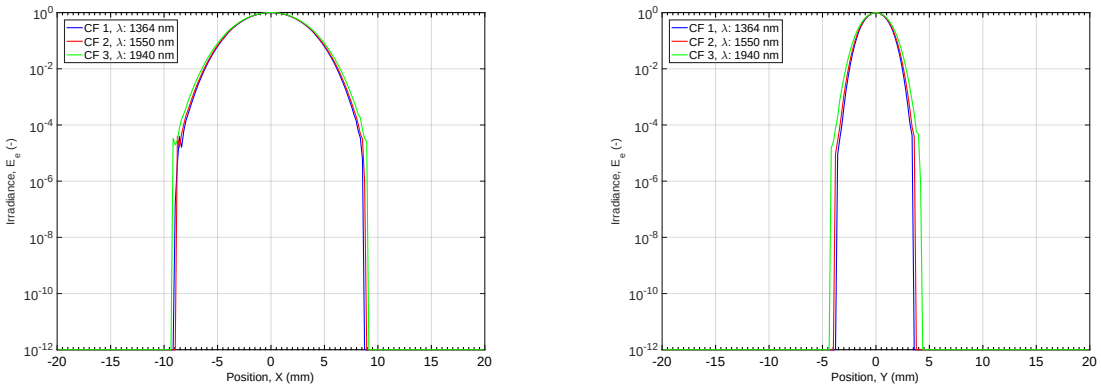

(a) X-axis. **(b)** Y-axis.

Figure 55: Three lens setup B: Normalized irradiance in log scale along both axes at the image surface for all configurations with respect to Gaussian illumination in NSQ mode.

Together with Figure 55, it confirmed that the adaptations of the previous three lens setup, discussed in Section 4.1.3, fully satisfy the adjusted boundary conditions with respect to the final beam dimensions. Furthermore, the results show that the intensity at the resonant PA cell edge drops to absolute zero providing excellent conditions for the PA measurement. As previously stated, the deviation in the beam diameter and efficiency among the individual configurations is primarily caused by the light interaction with the lens material and the AR-C coating characteristics.

In conclusion, the results for the optimized light source represent the basis for the two and three lens optical setups. In consideration of the boundary conditions, the three lens setup is superior to the two lens setup for this specific application as described in more detail in Section 4.1.3. Based on the necessary adjustments of the boundary conditions due to the laser window mount heating concept, the three lens setup A was adapted in order to satisfy the new laser beam dimensions. The two setups show similar ray tracing results regarding the peak intensity, power and efficiency at the image surface for all configurations. They display a high collimation quality and resilience to the lens position. All together, the three lens setup B was declared as the main optical setup for uniform and Gaussian illumination for the PA measurement setup. Additional ray tracing results for each configuration at different detector surfaces D_i along the LD propagation axis can be found in Appendix A.1.

4.2 Laser Diode Characteristics

This section discusses the obtained I-V-P characteristics for all three fiber coupled LDs. All results are displayed in Figure 56. Each subfigure provides the power P and voltage V dependency on the forward current I_f, and the corresponding threshold current I_{th}. The error bars mark the SD of all recorded values for each independent measurement step.

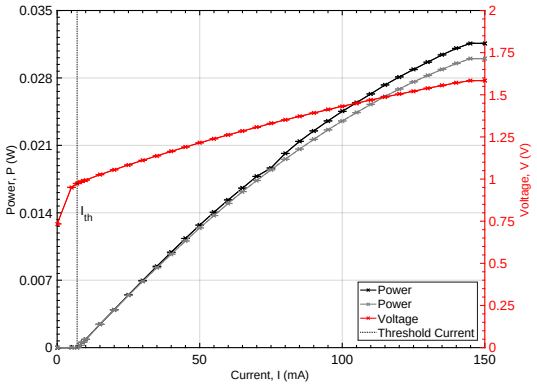

(a) LD 1: λ of 1364 nm.

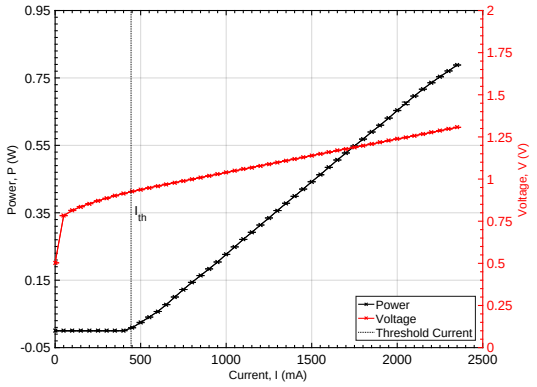

(b) LD 2: λ of 1550 nm.

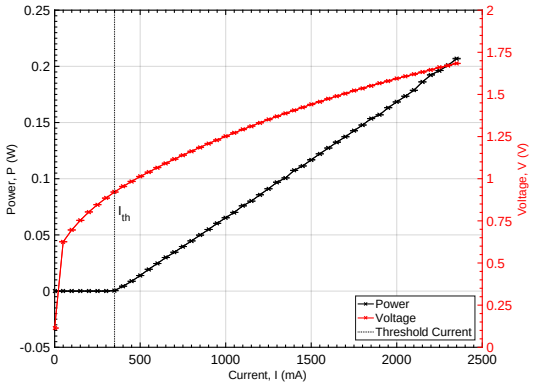

(c) LD 3: λ of 1940 nm.

Figure 56: I-V-P characteristics: Power and voltage dependency on the forward current for each individual LD.

In Figure 56a, the grey curve displays the simultaneously measured power via the integrated photodiode in the LD. All ITC4005 controller settings can be seen in Table 13. Further information about the fiber coupled LDs can be found in Table 2. In order to validate the LDs, the measured power was compared to the output power P_{DS}, given by the data sheet, for a specific $I_{f_{SP}}$ set point. As seen in Table 22, the difference in output power P to P_{DS} is insignificant and can be neglected. LD three even exceeds the

specified reference value P_{DS}. The subscripts DS and SP stand for data sheet and set point respectively. In conclusion, it is apparent from the obtained characteristics that all three LDs are in good agreement with the data sheet specifications. Furthermore, these results demonstrate that the accessible optical power, combined with an efficient coupling into the resonant cell, is sufficient for the PA measurement.

Table 22: I-V-P characteristics: Comparison of the measurement results to the data sheet specifications[24].

	Measurement				Data sheet	
	λ (nm)	T_{op} (°C)	$I_{f_{SP}}$ (mA)	P (mW)	P_{DS} (mW)	I_{th} (mA)
LD 1	1364	25	120	28	30.2	7
LD 2	1550	25	2300	771	780	350
LD 3	1940	25	2300	200	157	443.93

4.3 Beam Profile Analysis

As previously mentioned, the existing literature focuses particularly on two beam profiling methods, SSM and KEM respectively. The first segment compares the validation test results for each individual method in terms of accuracy and simplicity. Based on these assessments, the second part provides the beam profile analysis results of LD three with emphasis on beam divergence and diameter in order to identify the transverse beam profile, collimation quality and potential LD intensity side peaks. Additional information about beam profile analysis can be found in Sections 2.4 and 3.5.

4.3.1 Validation Tests

The experiments were performed on a laser module with a center wavelength of 402 nm in order to determine the accuracy and quality of each beam profiling method. All reference measurements were accomplished with the BC106N beam profiler. A more detailed description of the measurement setup can be seen in Section 3.5.1. Further information on the beam profiler can be retrieved from Appendix D.2.2.

[24] LD specifications: *NEL* (February, 2017); *FLC* (October, 2016); *OECA* (November, 2016).

4.3.1.1 Scanning Slit Method

The manufacturing process of the finite slit turned out to be the critical and limiting part of the experiment. The handmade slit is limited by the parallel alignment of the two razor blades resulting in an average minimum finite slit size of (450.0 ± 0.5) µm. Based on the reference measurement, the convolution integral was calculated for different slit sizes in order to make an assessment of the quality and resolution of the experimental data.

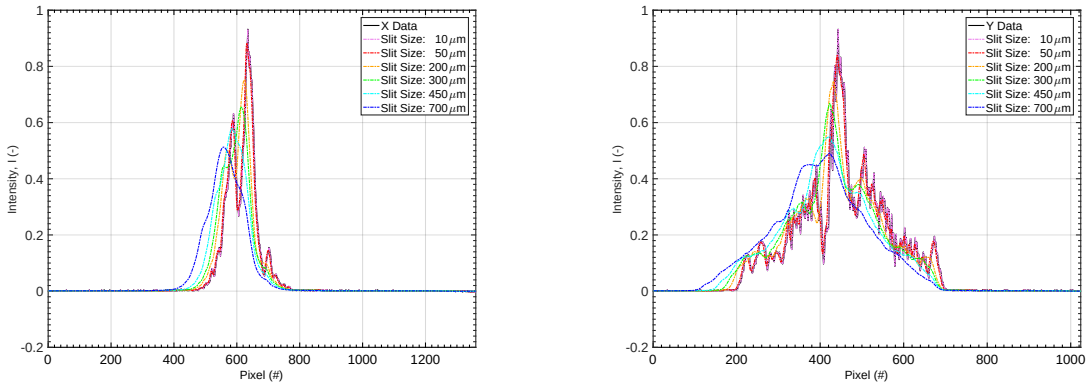

(a) X-profile. **(b)** Y-profile.

Figure 57: SSM: Reference measurement results for both beam profiles combined with convolution integrals for several slit sizes.

Figures 57a and 57b show the reference measurement results combined with the convolution integrals for several slit sizes for the x- and y-axis, respectively. Closer inspection of the figure indicates that a maximum slit size of around 300 µm is necessary to resolve small intensity features and to achieve a representative SSM result. It is worth mentioning that the obtained beam profile data for both axes is not an accurate representation of the whole laser beam due to the fact that the x- and y-profile only illustrate a single pixel row and column of the entire laser beam, respectively.

Overall, these calculated results verify that a slit size of 450 µm is not sufficient enough to obtain high resolved SSM results of the LD. Literature has shown that the ideal slit size is around 10 µm for SSM experiments in order to obtain high quality results [69]. Nevertheless, the reference data was fitted in accordance with the Gaussian model (Equation (3.7)). All results are illustrated in Appendix D.2.3.1, Figure 79. Subsequent shape-preserving piecewise cubic interpolation at the two $1/e^2$ points in intensity resulted in a $1/e^2$ beam radius $\omega_i(z)$ for the x- and y-profile. In comparison, Figure 58 provides the experimental SSM results along the x-profile of the LD. It shows the transmitted

power P over translation distance for two different step sizes Δx. The nonlinear regression results of the measurement data, indicated by the blue curve, and the corresponding 95 % prediction bounds for a new observation, represented by the red dotted lines, are displayed in Figure 58b. Identical to reference data analysis, $\omega_i(z)$ was derived by the interpolation results at the two $1/e^2$ points in intensity.

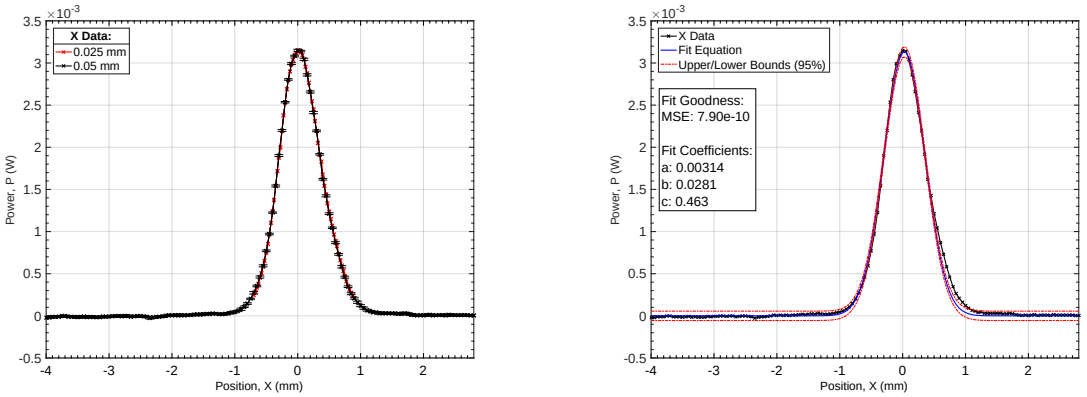

(a) Two step sizes. **(b)** Nonlinear fit.

Figure 58: SSM: Transmitted power over translation distance and nonlinear fit results for the x-profile.

From the figure, it is apparent that the LD intensity distribution slightly deviates from the ideal Gaussian intensity profile. Hence, the evaluated fit parameters a, b and c may only be considered an approximation. All obtained values for the $1/e^2$ beam radius $\omega_i(z)$ are displayed in the following table.

Interpolation:

Reference data	Experimental data	Deviation
$\omega_x(z)\,(\mathrm{mm}) : 0.595 \pm 0.005$	$\omega_x(z)\,(\mathrm{mm}) : 0.656 \pm 0.005$	$\Delta\omega_x(z)\,(\mathrm{mm}) : 0.061 \pm 0.010$
$\omega_y(z)\,(\mathrm{mm}) : 1.413 \pm 0.005$		

As can be seen from the table above, the difference between the two calculated beam radii $\omega_x(z)$ is $(0.061 \pm 0.010)\,\mathrm{mm}$, equivalent to $(9.29 \pm 1.52)\,\%$. This discrepancy could be attributed to certain factors that slightly affect the measurement and data analysis. Experimental data might be influenced by the limited finite slit size and parallel alignment of the two razor blades. Minimal variation in the mounting position of the beam profiler with respect to the aperture need to be taken into account as well. Further information about the beam profiler and sensor position can be found in Section D.2.2.

Another source of uncertainty is related to the shape-preserving piecewise cubic interpolation process. Each interpolated $1/e^2$ point in intensity strongly depends on the goodness and accuracy of the obtained nonlinear fitting results. Furthermore, the reference data is not an accurate representation of the entire laser beam but rather of a single pixel row/column through the center. Hence, all these uncertainties must be taken into account in the analysis and assessment of the obtained $\omega_x(z)$ values. In conclusion, the SSM validation test was successful, despite the not negligible value of $\Delta\omega_x(z)$. However, $\omega_x(z)$ need to be considered a good approximation of the $1/e^2$ beam radius.

4.3.1.2 Knife-Edge Method

In contrast to the SSM, the manufacturing process of the aperture is of little importance. Figure 59a shows the change in transmitted power versus the translation position of the sharp edge of the razor blade along the x-axis. Data analysis with respect to the actual beam profile was mainly focused on the slope of the actual measurement, representing the biggest change in transmitted power.

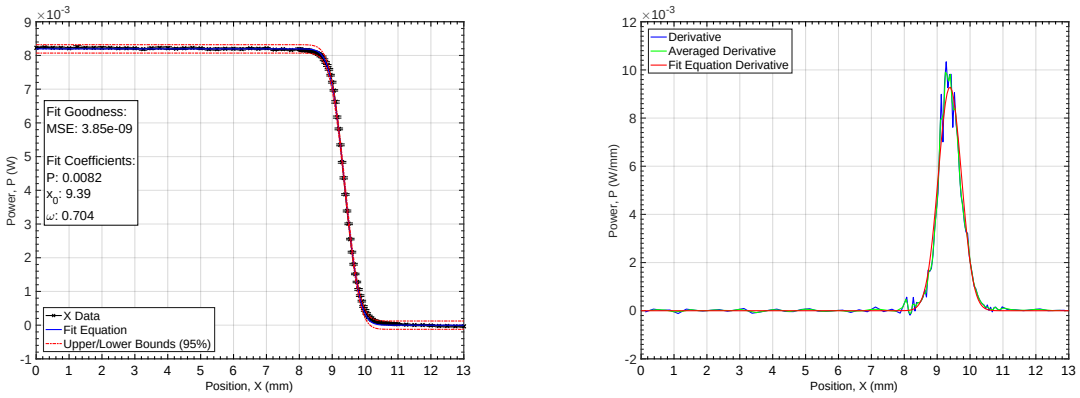

(a) **(b)**

Figure 59: KEM: (a) Transmitted power over translation distance and nonlinear fit results for the x-profile. (b) Overlap of all three data evaluation methods.

The nonlinear fitting results based on Equation (3.8) are highlighted by the blue line in Figure 59a. It is apparent that the nonlinear regression is in good agreement with the experimental data, showing only minimal deviations related to LD fluctuations at the fitting curve tails. In contrast to the SSM, the obtained fitting parameter $\omega_i(z)$ represents the $1/e^2$ beam radius of the Gaussian intensity profile. Figure 59b compares the data analysis results obtained according to Equations (3.9), (3.10) and (3.12). It can be seen that all evaluation methods yield almost the same LD beam profile in the x-axis.

A more detailed analysis of each individual method can be found in Appendix D.2.3.2.

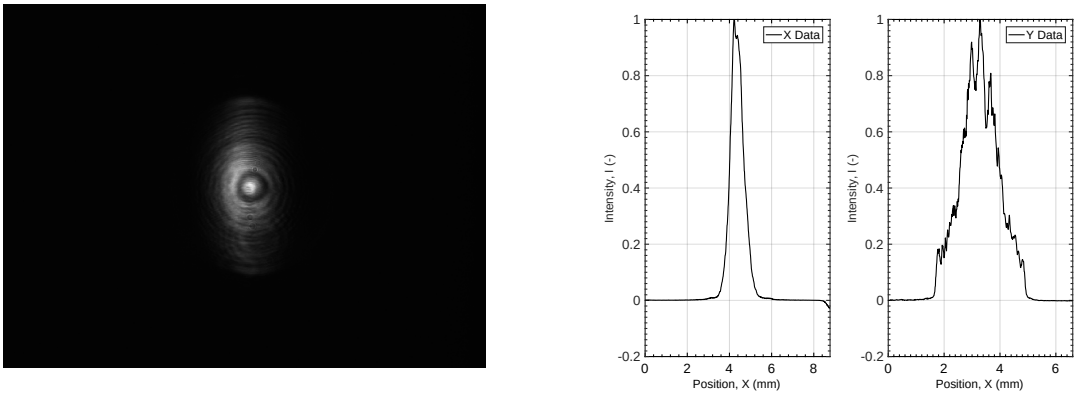

(a) **(b)**

Figure 60: KEM: Reference measurement result (a) illustrates the 2D beam profile grayscale image and (b) provides the corresponding normalized x- and y-profile, obtained by integration across all columns and rows.

The 2D beam profile grayscale image obtained by the reference measurement is illustrated in Figure 60a. As described in Section 3.5.1.2, the integration over all columns and rows yield the corresponding x- and y-profile, illustrated in Figure 60b. Reference data fitting was performed using the Gaussian model, followed by shape-preserving piecewise cubic interpolation at the two $1/e^2$ point in order to determine the $1/e^2$ beam radius $\omega_i(z)$ for both profiles. The obtained fitting results for both axes can be seen in Appendix D.2.3.2. The table below compares the $1/e^2$ beam radius $\omega_i(z)$ determined by the experimental and reference measurement. It can be seen that the deviation $\Delta\omega_x(z)$ of the two determined beam radii in the x-axis is $(0.065 \pm 0.011)\,\mathrm{mm}$, equivalent to $(9.23 \pm 1.56)\,\%$.

Interpolation:	**Fitting Parameter:**	
Reference data	Experimental data	Deviation
$\omega_x(z)\,(\mathrm{mm}) : 0.639 \pm 0.005$	$\omega_x(z)\,(\mathrm{mm}) : 0.704 \pm 0.006$	$\Delta\omega_x(z)\,(\mathrm{mm}) : 0.065 \pm 0.011$
$\omega_y(z)\,(\mathrm{mm}) : 1.389 \pm 0.005$		

As a matter of fact, $\Delta\omega_x(z)$ is in the same order of magnitude as for the SSM. Again, the difference might be related to razor blade alignment and minimal variation in the mounting position as previously discussed in Section 4.3.1.1. Another potential for bias relies on data analysis procedure due to two different fit formulas, Equations (3.7) and (3.8). The experimental and reference data (Figures 59b and 60b) were normalized and subsequently

plotted as an overlay graphic, displayed in Figure 61. It is apparent that the obtained x-profiles are relatively well aligned and in good agreement. Although $\Delta\omega_x(z)$ is not negligible, the KEM validation test was successful as well, providing an attractive tool for LD beam profile analysis. In conclusion, both beam profiling methods were successfully tested and revealed a $1/e^2$ beam radius $\omega_x(z)$ of similar size, varying only by $\Delta\omega_x(z)$ of $(0.048 \pm 0.011)\,\mathrm{mm}$, equivalent to $(6.81 \pm 1.56)\,\%$. Due to potential measurement and data analysis uncertainties, the obtained $\omega_x(z)$ values need to be considered a good approximation of the $1/e^2$ beam radius. Overall, the simple manufacturing process and alignment of the aperture indicate that the KEM is superior to the SSM and less prone to errors for this specific task.

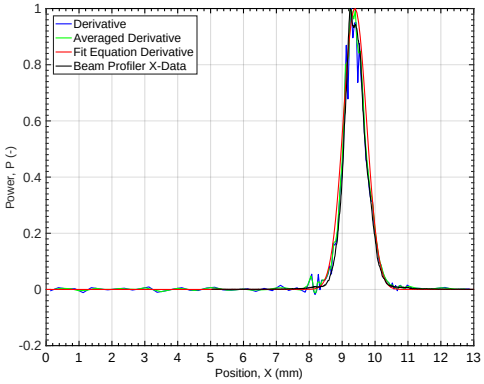

Figure 61: KEM: Comparison of the normalized x-profile reference data and experimental data analysis results.

4.3.2 Beam Profiling Measurements

The translation direction of the razor blade was reversed for all following measurements, in order to optimize the sensitivity and resolution for low transmitted power features. Further information can be found in Section 3.5.2.

4.3.2.1 Laser Diode

Figures 62 and 63 provide the experimental data, the change in transmitted power versus translation position, for measurement points P_1 and P_2 along the x- and y-axis. What is striking about the data is the presence of two minor measurement artifacts at low energy levels in both profiles. A possible explanation for the slightly negative values, illustrated by the green rectangle, is that heat in any form is hitting the power meter housing. The second phenomenon, highlighted by the orange rectangle, may be attributed to scattering effects on the physical aperture or to an LD artifact. Despite several attempts to minimize these artifacts, such as covering the razor blade by tape, power meter position fine-tuning with respect to the physical aperture, improvement of fiber coupling quality and mode mixing, the measurement data always displayed similar features.

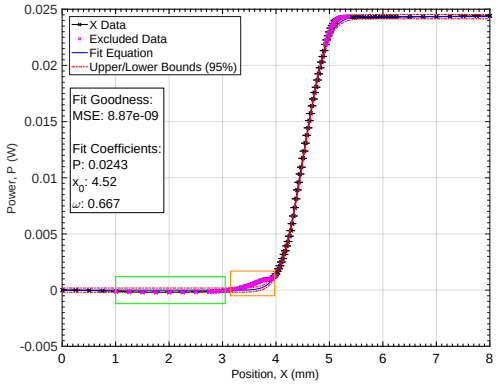

(a) P_1.

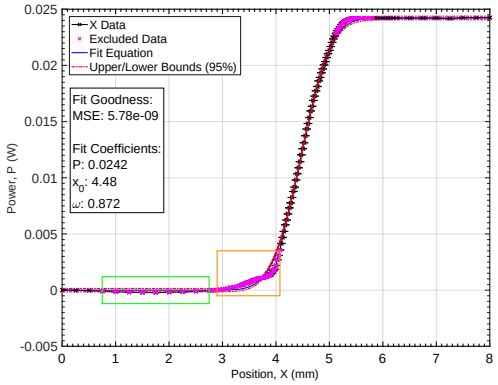

(b) P_2.

Figure 62: LD: Transmitted power over translation distance and nonlinear fit results for the x-profile at measurement points P_i.

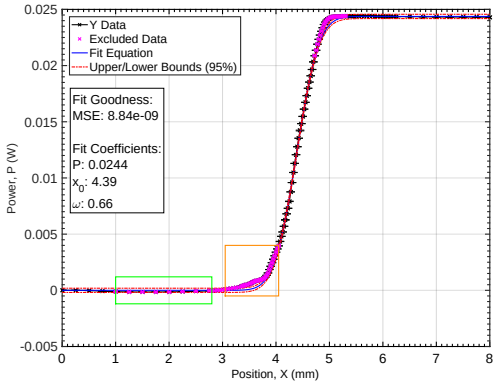

(a) P_1.

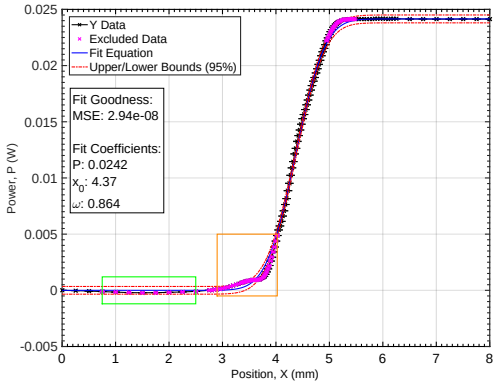

(b) P_2.

Figure 63: LD: Transmitted power over translation distance and nonlinear fit results for the y-profile at measurement points P_i.

Therefore, outliers and data points located at the tails were excluded from the nonlinear fitting model, highlighted in pink, in order to minimize the influence of these artifacts. From Figures 62 and 63 it can be seen that the nonlinear regression in accordance with Equation (3.8), highlighted by the blue curve, is in good agreement with the slope of the experimental data for the x- and y-beam profile. In addition, minimal deviations at the fitting curve tails can be related to LD fluctuations, as discussed in Section 4.3.1.2.
Data analysis results obtained according to Equations (3.9), (3.10) and (3.12) are compared in Figures 64 and 65 for P_1 and P_2 along both axes. It is apparent that all evaluation methods yield a similar LD beam profile for both axes. Additional data smoothing is achieved by the averaged derivative method compared to the derivative method.

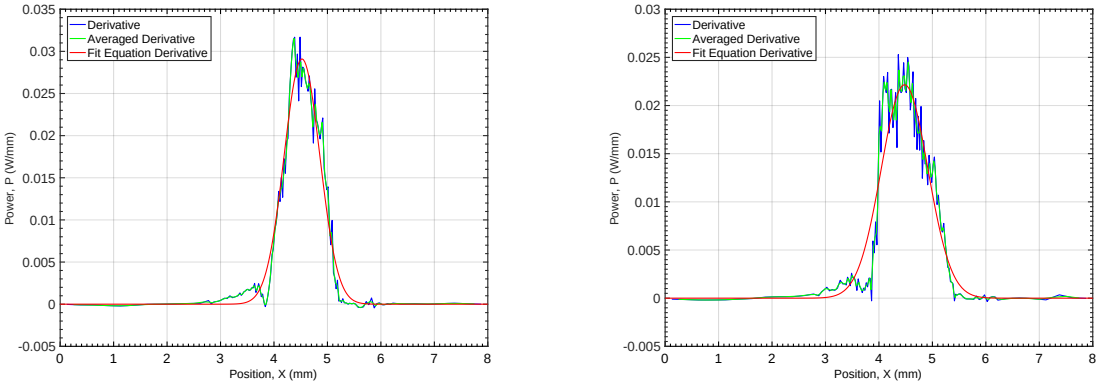

(a) P_1. **(b)** P_2.

Figure 64: LD: Overlap of all data evaluation methods for the x-profile at measurement points P_i.

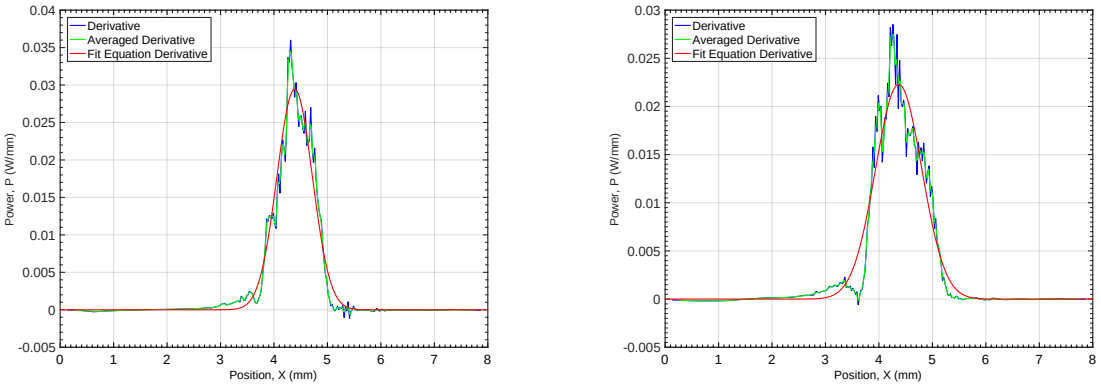

(a) P_1. **(b)** P_2.

Figure 65: LD: Overlap of all data evaluation methods for the y-profile at measurement points P_i.

A more detailed analysis of each individual evaluation method can be found in Appendix D.2.4.1. The fit parameter of interest for the subsequent determination of the divergence angle is the $1/e^2$ beam radius $\omega_i(z)$. In combination with the separation distance ΔL_{21}, the beam divergence angle ϕ_i was determined using Equation (3.14) for the x- and y-profile. All beam radii $\omega_i(z)$ and obtained divergence angles for both axes are summarized in the following table. The corresponding $\Delta\omega_i(z)$ represents the standard error of the nonlinear regression, while $\Delta\phi_i$ is derived from Equation (3.15). It can be seen that both beam profiles display a divergence angle of similar size. However, it is worth mentioning that the obtained divergence angles differ significantly from the MM fiber's NA of 12.71 °. This discrepancy might be related to previously mentioned sources of uncertainties regarding the accuracy and goodness of the nonlinear fitting results.

The evaluation process manifested a high sensitivity of the obtained fitting parameters to the exclusion of specific experimental data points in immediate vicinity of those artifacts. A minimal change in $\omega_i(z)$ has a big impact on the divergence calculation according to Equation (3.14). Overall, these results must be interpreted with caution and can only be considered a good approximation of the divergence angle for both axes.

Beam Radius:

X-profile

$\omega_1(z)\,(\mathrm{mm}) : 0.667 \pm 0.002$

$\omega_2(z)\,(\mathrm{mm}) : 0.872 \pm 0.003$

Y-profile

$\omega_1(z)\,(\mathrm{mm}) : 0.660 \pm 0.003$

$\omega_2(z)\,(\mathrm{mm}) : 0.864 \pm 0.006$

Beam Divergence:

X-profile

$\phi_x\,(^\circ) : 9.31 \quad \pm 0.23$

Y-profile

$\phi_y\,(^\circ) : 9.28 \quad \pm 0.42$

4.3.2.2 Laser Diode with Aspheric Condenser Lens

In an attempt to gather more details about the present artifacts, the collimated LD beam profile was investigated. Additional information can be found in Section 3.5.2.2. Figure 66 presents the change in transmitted power versus translation position for the x- and y-profile, respectively. Each subfigure provides an overlay of the experimental data at two distinct measurement points P_1 and P_2 separated by ΔL_{21}.

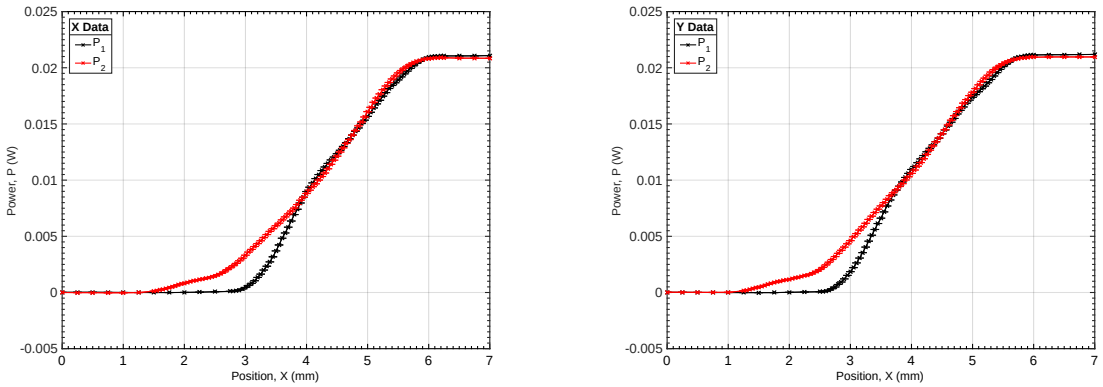

(a) X-profile. **(b)** Y-profile.

Figure 66: LD with ACL: Overlay of transmitted power over translation distance for both profiles at measurement points P_i.

This figure is quite revealing in several ways. First, it is apparent that the experimental data clearly deviates from the cumulative Gaussian distribution defined in Equation (3.8), leading to the assumption that the nonlinear fit is not a good representation of the experimental data. Secondly, the previously discussed artifacts disappeared at P_1 in both profiles, highlighted by the black curve. Instead a slight change in slope can be seen, leading to a more pronounced intensity peak on the left side of the obtained beam profile as seen in Figures 67a and 68a. Lastly, the experimental data at P_2 displays an intensity feature similar to the obtained artifacts in Section 4.3.2.1, illustrated by the red curve. Data analysis results for the x- and y-profile according to Equations (3.10) and (3.12) are summarized in Figures 67 and 68.

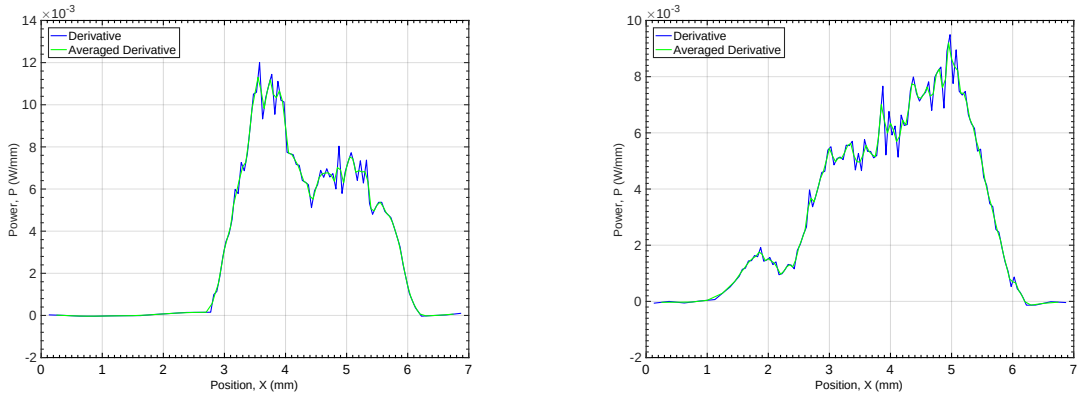

(a) P_1. **(b)** P_2.

Figure 67: LD with ACL: Overlap of all data evaluation methods for the x-profile at measurement points P_i.

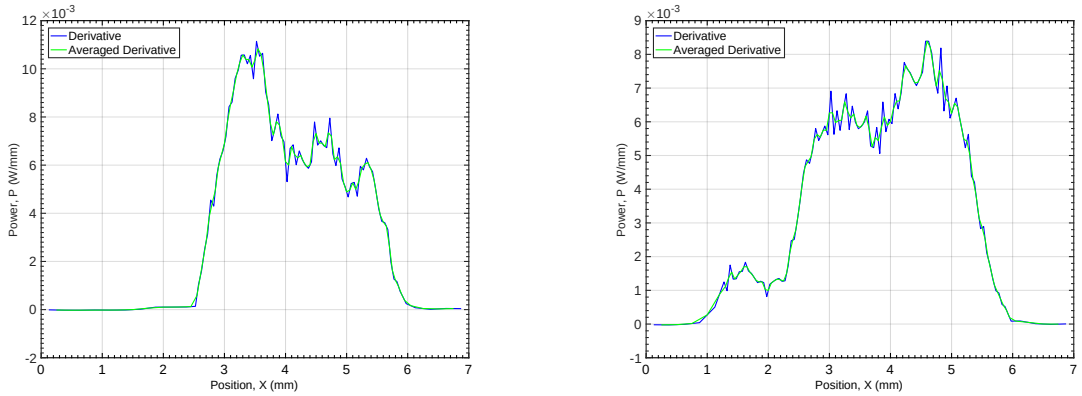

(a) P_1. **(b)** P_2.

Figure 68: LD with ACL: Overlap of all data evaluation methods for the y-profile at measurement points P_i.

As previously discussed, the beam diameter $D_i(z)$ for P_i was derived from shape-preserving piecewise cubic interpolation results at the two $1/e^2$ points in intensity of both data sets. Combined with the separation distance ΔL_{21}, the beam divergence angle was obtained for the x- and y-profile in accordance with Equations (3.16) and (3.17). The resulting beam diameters and divergence angles for both data sets are compared in the table below.

Derivative	**Averaged Derivative**
Beam Diameter:	
X-profile	X-profile
$D_1(z)\,(\mathrm{mm}) : 3.07 \pm 0.01$	$D_1(z)\,(\mathrm{mm}) : 3.09 \pm 0.01$
$D_2(z)\,(\mathrm{mm}) : 3.52 \pm 0.01$	$D_2(z)\,(\mathrm{mm}) : 3.59 \pm 0.01$
Y-profile	Y-profile
$D_1(z)\,(\mathrm{mm}) : 3.13 \pm 0.01$	$D_1(z)\,(\mathrm{mm}) : 3.15 \pm 0.01$
$D_2(z)\,(\mathrm{mm}) : 3.77 \pm 0.01$	$D_2(z)\,(\mathrm{mm}) : 4.35 \pm 0.01$
Beam Divergence:	
X-profile	X-profile
$\phi_x\,(^\circ) : 0.650 \pm 0.045$	$\phi_x\,(^\circ) : 0.723 \pm 0.047$
Y-profile	Y-profile
$\phi_y\,(^\circ) : 0.916 \pm 0.052$	$\phi_y\,(^\circ) : 1.71 \pm 0.07$

The discrepancy in ϕ_i relates specifically to the influence of intensity side peaks and fluctuations on the nature of shape-preserving piecewise cubic interpolation. A minimal change in the obtained beam diameter $D_i(z)$ can lead to significant variation in the final divergence angle according to Equation (3.16). A closer look at the interpolation results in Figures 90 and 91 verify that the significant increase in beam diameter of the y-profile at P_2, and consequently the beam divergence, is related to the existence of the intensity side peak. In addition, minor deviations in $D_i(z)$ and ϕ_i can be attributed to the fact that two different data sets, namely the derivative and averaged derivative, were employed for the interpolation process. In summary, the absence of the intensity feature at P_1 in both axes further supports the hypothesis that this intensity feature can be related to an LD artifact. It can be seen that the collimation quality of the light source is the key factor to minimize and suppress the appearance of the intensity peak along the propagation axis.

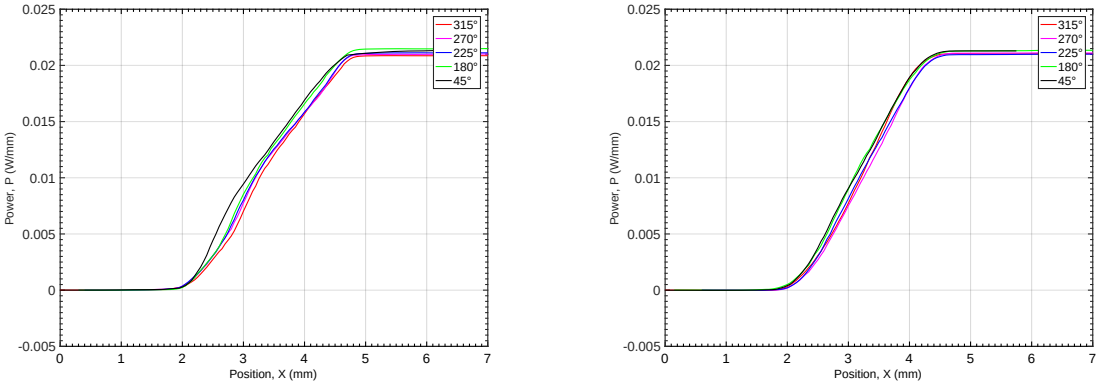

(a) P_1. **(b)** P_2.

Figure 69: LD with ACL: Overlap of the experimental data for specific set of angles at measurement points P_i.

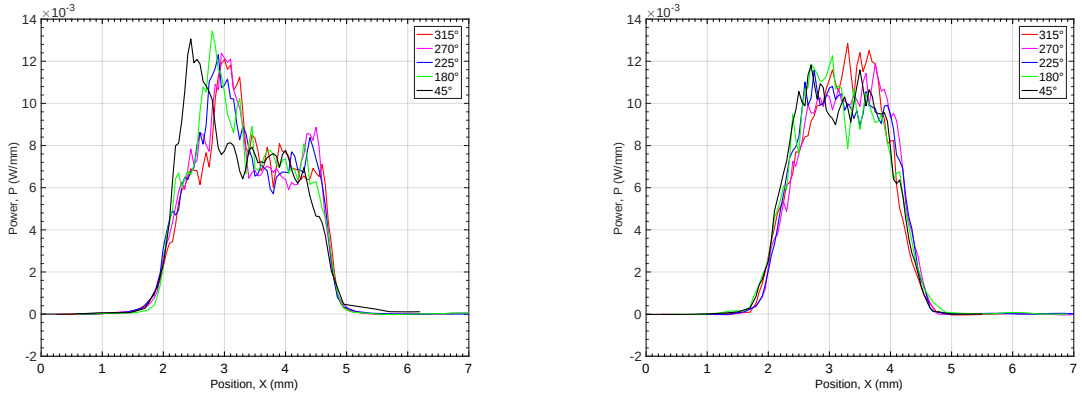

(a) P_1. **(b)** P_2.

Figure 70: LD with ACL: Overlap of the averaged derivative data for specific set of angles at measurement points P_i.

In order to further investigate and verify this hypothesis, the beam profile was analyzed at different angles for both measurement points P_1 and P_2. Figure 69 shows the overlay of the experimental data, transmitted power over translation position, for a specific set of angles at measurement points P_i. The corresponding data analysis results in accordance with Equations (3.10) and (3.12) are compared in Figure 70. The most interesting aspect is that no more artifacts are visible at both measurement points P_i. Instead, a significant change in slope can be detected for specific angles at different razor blade positions, leading to a more pronounced intensity peak at P_1 in Figure 70. Closer inspection of the data revealed an alleged dependence of the LD rotation on the observed intensity peak shift along the x-axis. Separated by ΔL_{21}, measurement point P_2 shows a more homogenous intensity profile throughout all beam profile axes. Together, these results provide strong

evidence for the validity of the proposed hypothesis. In addition, a minimal decrease in beam diameter $D_i(z)$ with distance can be observed in Figure 70b, indicating a negative non-zero divergence angle ϕ_i. The table below provides an overview of the calculated divergence angles ϕ_i for multiple profiles in accordance with Equations (3.16) and (3.17).

Beam Divergence:

Derivative	Averaged derivative
$\phi_{315}\,(^\circ) : -0.615 \pm 0.059$	$\phi_{315}\,(^\circ) : -0.653 \pm 0.060$
$\phi_{270}\,(^\circ) : -0.546 \pm 0.056$	$\phi_{270}\,(^\circ) : -0.547 \pm 0.056$
$\phi_{225}\,(^\circ) : -0.626 \pm 0.059$	$\phi_{225}\,(^\circ) : -0.613 \pm 0.059$
$\phi_{180}\,(^\circ) : -0.393 \pm 0.051$	$\phi_{180}\,(^\circ) : -0.368 \pm 0.051$
$\phi_{45}\,(^\circ) : -0.388 \pm 0.051$	$\phi_{45}\,(^\circ) : -0.440 \pm 0.053$

It can be seen that both data sets yield similar results for each selected beam profile axis. As previously discussed, minimal deviations in ϕ_i can be related to the shape-preserving piecewise cubic interpolation process of the derivative and averaged derivative data and to potential alignment and mounting uncertainties. The variation of the divergence angle leads to a different beam width reduction across the 2D beam profile with separation distance, as seen in Figure 70b. Together these results provide important insights into the collimation quality and final beam profile.

The impact of the reported LD artifact on the PA measurement is closely related to the boundary conditions and design of the optical system. In this case, the main objective of the illumination system is to maximize the energy transfer into the PA cell without light interaction with the PA cell material. Hence, the relevance of the intensity side peak for the optical system depends on the collimation quality and the final beam diameter. These experiments confirmed that the obtained collimation minimizes and suppresses the appearance of this low intensity feature along the propagation direction, as seen in Figures 69 and 70. Therefore, it can be concluded that the LD artifact is negligible and has no effect on the measurement quality. To develop a full and more comprehensive picture of the 2D beam profile, a large number of KEM measurements must be carried out at points P_i. This would go beyond the scope of the work. Hence, all results need to be considered a good approximation due to the sensitivity of the interpolation process to the experimental data and limited number of measuring angles.

4.4 Validation Test

This section covers the optimization process of PA signal amplitude using the LD tuning method, based on the direct correlation between the PA signal amplitude, the medium's absorption characteristics and LD spectral properties, followed by the analysis of PA measurement in humid environment. Further information can be found in Section 3.6.

4.4.1 Laser Diode Tuning

According to LD specifications[25], the peak wavelength is approximately 1364.66 nm at an LD operating temperature of 25 °C. Possible minor deviations of the nominal peak wavelength are in the range of (1363.69 to 1365.69) nm. The tuning results display the obtained lock-in PA signal amplitude and phase over the LD operating temperature increments. Error bars represent the SD of all recorded sample points per measurement increment. In this section, the discussion is focused on the temperature sweep results in the vicinity of the maximum PA signal amplitude, illustrated in Figure 71a. Closer inspection of the figure reveals a global maximum (GM) and local maximum (LM) of the PA signal amplitude at 26.9 °C and 26.2 °C, respectively. A more comprehensive picture was obtained by comparing the experimental data to the absorption specifics of the atmospheric gas mixture for two temperatures, 296 K and 298 K, displayed in Figure 71b.

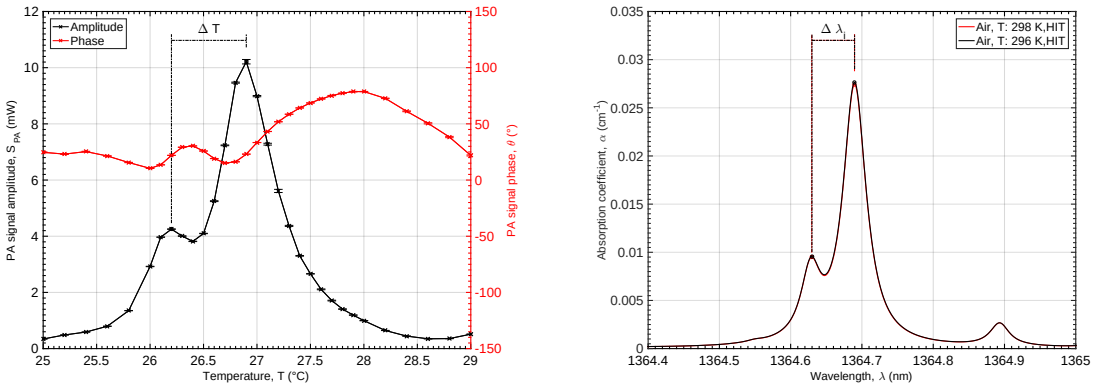

(a) **(b)**

Figure 71: LD tuning: (a) Lock-in PA signal amplitude and phase over the LD operating temperature [(25 to 29) °C]. (b) HITRAN [26] absorption coefficient data of the atmospheric gas mixture at 296 K and 298 K.

[25] LD specifications: *NEL* (February, 2017).

The absorption coefficient α shows virtually the same behavior and features as the experimental data in Figure 71a. The fine-tuning process of the wavelength by the temperature parameter corresponds to the movement along the absorption coefficient curve in Figure 71b. A more detailed analysis of the absorption data given by the HITRAN [26]database [34] with respect to the GM and LM features can be seen in the following table.

HITRAN:

GM		LM	
$\alpha_{296\,\mathrm{K}}\,(\mathrm{cm}^{-1})$:	0.028	$\alpha_{296\,\mathrm{K}}\,(\mathrm{cm}^{-1})$:	0.0096
$\alpha_{298\,\mathrm{K}}\,(\mathrm{cm}^{-1})$:	0.027	$\alpha_{298\,\mathrm{K}}\,(\mathrm{cm}^{-1})$:	0.0095
$\lambda_{296\,\mathrm{K}}\,(\mathrm{nm})$:	1364.689	$\lambda_{296\,\mathrm{K}}\,(\mathrm{nm})$:	1364.629
$\lambda_{298\,\mathrm{K}}\,(\mathrm{nm})$:	1364.689	$\lambda_{298\,\mathrm{K}}\,(\mathrm{nm})$:	1364.629

To estimate the wavelength change per degree, the separation distances $\Delta\lambda_i$ and ΔT between GM and LM must be determined in the respective subfigure. The subscript i stands for either 296 K or 298 K. The obtained separation distances equal 0.06 nm and 0.7 °C, resulting in an approximate peak wavelength change of 0.085 nm per one degree Celsius. Unlike the PA signal amplitude, the lock-in signal phase shows a surprising behavior in Figure 71a. Against the expectations of a constant phase, the experimental data revealed significant phase fluctuations with temperature variation. This phenomenon can be related to the relatively strong changes of the LD driver signal at different temperatures. Even the smallest changes in frequency and amplitude of the LD can significantly influence the phase and PA signal. Supplementary information about the LD tuning results over a broad temperature interval of (20 to 30) °C can be found in Appendix E, Figure 92.

In conclusion, the LD tuning process in ambient air with a rH of $(40.0 \pm 0.8)\,\%$ was successful. The obtained PA signal amplitude variation over temperature is in good agreement with the absorption coefficient data in Figure 71b. By altering the operating temperature set point from 25.0 °C to 26.9 °C, an amplification of the PA signal by a factor 10 was achieved. Hence, Figure 71a provides a reliable measure for optimizing the PA signal with respect to the subsequent PA validation test in humid environment.

[26] HITRAN *on the Web*, USA model, mean latitude, summer, H=0 [41]. [Online] Accessed: March, 2018 .

4.4.2 Photoacoustic Measurement

Figure 72 displays the obtained lock-in PA signal amplitude and phase over the measured values for specific rH set points. The error bars of the PA signal amplitude and phase represent the SD of all recorded sample points per rH measurement increment and the uncertainty of the reference humidity sensor (± 2 % rH) in accordance with the *Sensirion AG* specifications [97]. The ideal scenario describes a linear correlation between the measured PA and rH signals. This means a small variation of the rH within the resonator implies an immediate change of the obtained PA signal amplitude in the same order of magnitude. The true correlation of the experimental data is represented by a second degree polynomial function. The 95 % prediction bounds for new observations are displayed by green dotted lines in Figure 72. Minor deviations from the ideal result might be explained by potential damping effects (e.g. air/water dispersion and molecular relaxation processes related to the buffer gas mixture), the measurement uncertainty of the rH sensor and measurement fluctuations of the PA signal amplitude. The basis of potential attenuation effects caused by the buffer gas are discussed more closely in context with the PA phase.

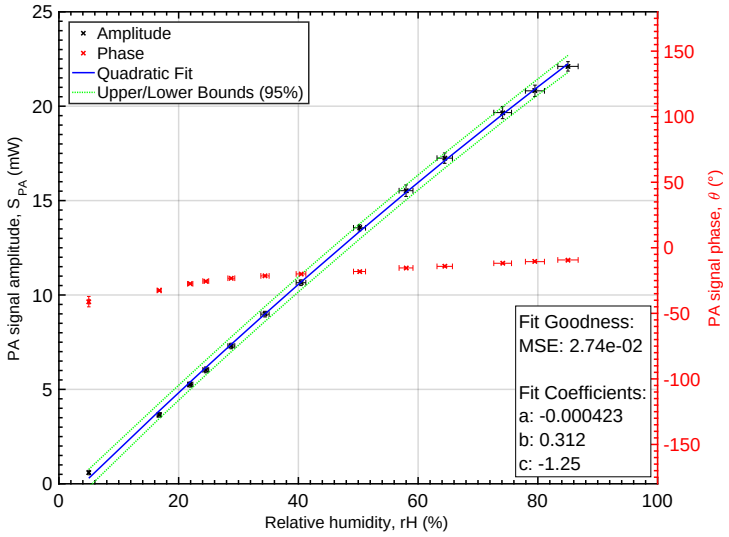

Figure 72: PA measurement: Lock-in PA signal amplitude and phase over rH. Correlation of the experimental data is represented by a quadratic fit equation with 95 % prediction bounds for new observations.

Precautions such as delay time and dynamic control of the rH value within the PA cell resulted in a constant rH value with a reported stability of ± 2 % rH [15] for each PA measuring step. The residual analysis of the quadratic fit is presented in Appendix E.2.

The second part of the PA signal provides the phase information of every measurement point, as seen in Figure 72. The obtained PA phase signal reveals a significant phase shift to the laser modulation and fluctuations with varying humidity conditions. A possible explanation for the phase shift may be the influence of the buffer gas (humidified atmosphere), especially the existence of diatomic molecules such as O_2, N_2, on the PA signal. Instead of the immediate release of heat, excess energy is transferred by collision to long lifetime excited states of diatomic molecules (e.g. O_2) resulting in an elongated global relaxation lifetime τ. In this specific case, the PA signal experiences a phase shift ($\theta \neq 0$), potential damping due to less efficient sample heating and a parabolic dependency on the measured gas concentration C. Additional information about the influence of molecular relaxation on the PA signal generation can be found in Section 2.2.1.1.
It is noteworthy, that the obtained phase shift decreases with increasing concentration of water vapor in Figure 72. This trend could be attributed to the potential catalyzing effect of water vapor on the relaxation processes of many species. It has been shown that a small percentage of water vapor significantly reduces the relaxation lifetime of O_2 [71, 73], promoting vibrational relaxation of water vapor-O_2 system. Hence, the higher the VWC, the faster the relaxation process and the weaker the obtained phase shift. For a complete picture of the PA phase signal, the influence of temperature and pressure within the PA cell and the potential humidity dependence of the microphone must likewise be taken into account.

In summary, the experimental results confirm and validate the functionality of the entire PA measurement setup described in Section 3.6.3 in humid environment. Despite slight deviations from the ideal linear model, the PA signal amplitude varies almost in the same magnitude as the change in rH, as seen in Figure 72. The PA sensor indicated a significantly faster response (τ_{63}) compared to the reference sensor for changes in rH within the resonant cell. Explicit response time measurements are still to come in the near future. However, the PA phase information indicates a strong dependency on the buffer gas, especially on diatomic molecules, and the molecular relaxation processes involved. These phenomena may explain the obtained phase shift and signal amplitude damping in Figure 72. Considerably more work will need to be done in order to fully understand the implications of the buffer gas on the PA signal with respect to molecular relaxation processes. All in all, the first successful proof of concept is a good basis for further improvements and calibrations with the ultimate goal of implementation in a LT-PEMFC.

CHAPTER 5

Conclusion and Outlook

The exploration of a PA sensor system for the determination of phase and concentration of water for potential application in LT-PEMFC water balance analysis represent the central motivation of this thesis. The essential contribution of this work was the development of the concept and design of the PA experimental setup with regard to the integration of the PA resonator prototype, developed by *Benjamin Lang*, and the subsequent first validation measurement in humid environment.

The design of a universal optical setup, eligible for all three lasing wavelengths, was performed on the basis of calculations and ray tracing simulations of two optical concepts in order to optimize the configuration of the optical devices along the propagation direction. The three lens system B delivers the optimum results in terms of collimation quality, resilience, coupling efficiency of the laser beam into the resonance cell and prevention of intensity cut-offs for a given set of boundary conditions. All ray tracing results for both illumination types (uniform and Gaussian) are shown in Section 4.1.4, Tables 20 and 21. The realization of the optical setup for a stable and compact implementation of the PA resonant cell was developed in *SolidWorks*.
A possible improvement for the future is the installation of a fiber splitter, which allows the simultaneous connection of all three LDs to the SMA fiber adapter plate. Furthermore, it reduces potential power and beam shape fluctuations of the MM LDs caused by contact with the MM fiber (e.g. mode mixing) and coupling process.

The intended potential application in a LT-PEMFC entails special limitations and challenges on materials and components. In detail, the presence of aggressive, humid H_2 and DI water may give rise to hydrogen embrittlement of materials and contamination of the catalyst layer, respectively. In order to ensure reliable and safe operation of these systems, high-strength stainless steel (316L) and insoluble materials (e.g. N-BK7® for laser windows) were selected for components in direct contact with the humid environment. A potential future improvement of the PA system in terms of transmission and coupling efficiency into the resonant cell is the application of specially manufactured AR coatings for the entire spectral range ((1 to 2) μm) onto the laser window surface.

Aside from the optical setup, the quality of the laser source in terms of power, beam diameter and spectral properties also plays a tremendous role in a PA system. The created beam profile analysis setup, based on the KEM, revealed a low intensity side peak of LD three (1940 nm) for the x- and y-profile in a series of measurements, highlighted in Section 4.3.2.1, Figures 64 and 65. It has been demonstrated that the collimation quality is the key factor to minimize and suppress the appearance of this LD artifact along the propagation direction. These experiments confirmed that the impact of the LD artifact on the PA signal quality is negligible due to the achieved collimation quality and final beam diameter, limited by the optical setup. Data analysis exhibits minor deficiencies in case of deviation to an ideal Gaussian intensity profile, presence of outliers and artifacts and potential measurement uncertainties. Hence, the obtained beam diameters and divergence angles must be regarded as good approximations for further optimization steps.

The first validation of the PA sensor system was focused on the humid phase, the most relevant phase for LT-PEMFC applications due to potential external humidification of reactant gases and the predominance of water in the vapor phase at the inlet and outlet. Prior to the experiment, wavelength fine-tuning of the DFB-LD in ambient air was performed in order to maximize the PA signal amplitude in accordance with HITRAN atmospheric gas absorption data. The data evaluation revealed an approximate peak wavelength shift of 0.085 nm per one degree Celsius. The maximum PA signal amplitude was obtained at an operating temperature of 26.9 °C, equal to an amplification by a factor of 10 compared to the initial operating temperature, as shown in Figure 71. The obtained PA phase fluctuations can primarily be associated to relatively strong changes of the LD driver signal (frequency and amplitude) at different temperatures.

Considering the early stages and the development of the project from scratch, the first validation test is successful and satisfying. The results discussed in Section 4.4.1 confirm the functionality of the PA measurement setup in humid environment. The PA sensor, limited by the humidifier, displays a quadratic response to variations in the humidity conditions ((5 to 85) % rH) of the gas flow through the PA cell. Furthermore, the first validation test indicated a significantly faster response time (τ_{63}) compared to the reference sensor for various humidity steps. Experimental proof in form of detailed response time measurements for abrupt changes in the humidity level and subsequent determination of τ_{63} is still to come. The obtained PA phase shift to the laser modulation and fluctuations with varying humidity conditions may be linked to interactions with the buffer gas, especially the existence of diatomic molecules such as O_2 and N_2. Further research is required to fully understand the implications of the buffer gas on the PA signal with respect to molecular relaxation processes.

Outlook

The next stages in this project consist of LWC and IWC validation measurements in the icing wind tunnel under constant environmental conditions with well-established reference methods (e.g. blade method, rotating cylinder and hot-wire principle) to determine the LWC and IWC and subsequent comparison to numerical simulations. In addition, the response time for abrupt changes in the respective phase are investigated.

The transition from the PA system prototype for validation experiments to potential LT-PEMFC applications poses further challenges that need to be addressed to guarantee a safe and reliable operation. The anticipated installation of the PA sensor in the exhaust tract entails a potential modification of the inlet diverter design of the PA cell to prevent water return and the simultaneous N_2 purging of bandstop filter. In case of dynamic FC operations, the influence of gas composition, pressure and temperature on the speed of sound and the occurrence of possible damping effects in the air/water dispersion demands an active resonance frequency tracking. The long time goal should be the first integration at the exhaust tract in a stationary LT-PEMFC system. Simultaneous monitoring of both the physical state and the concentration of water is realized by LD modulations at three slightly different frequencies, all within the same resonance peak of the PA cavity, combined with a highly selective lock-in detection. The ability to determine the TWC (= LWC+VWC) with a high time resolution within a LT-PEMFC system would dramatically improve the water balance analysis, its overall performance and lifetime.

APPENDIX A

Optical Setup

A.1 Three Lens Setup B

This section shows additional ray tracing results for the three lens setup B in NSQ mode, discussed in Sections 3.1.5 and 4.1.4. Figure 73 illustrates the irradiance distribution of the 2D beam profile at the image surface for each configuration. In addition, the collimation quality and impact of the broad wavelength range on the beam dimensions at the image surface for each configuration are provided in Figures 74 to 76.
Each figure displays the irradiance in log scale along the x- and y-axis at detector surfaces D_1, D_2 and D_3, which were placed in the optical setup along the propagation axis at (70, 85 and 100) mm, as shown in the geometrical drawing in Figure 20b. In this scenario, detector D_3 simultaneously represents the image surface of the optical system.

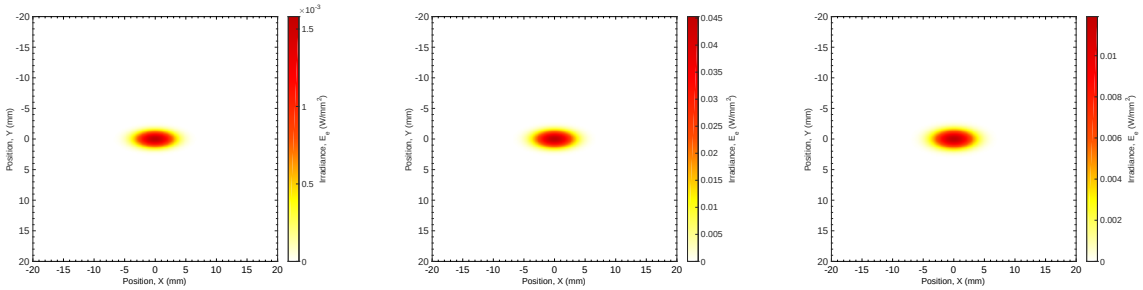

(a) CF 1. **(b)** CF 2. **(c)** CF 3.

Figure 73: Three lens setup B: Irradiance distribution of the 2D beam profile at image surface for all configurations with respect to Gaussian illumination in NSQ mode.

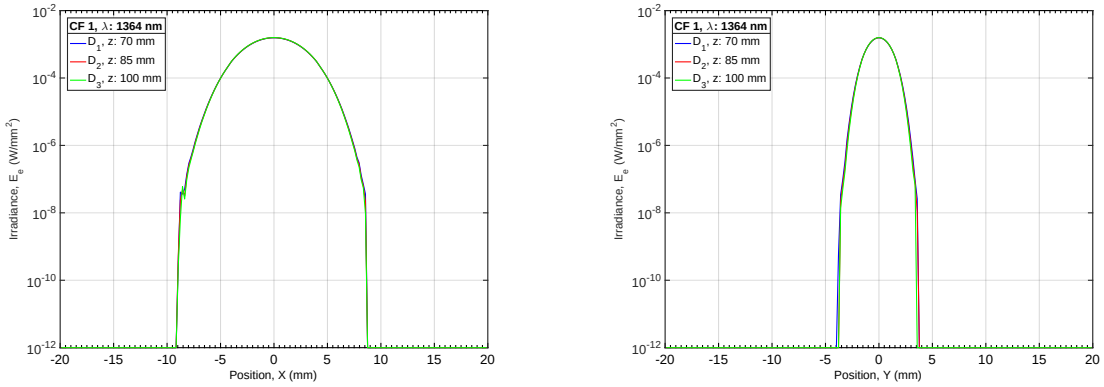

(a) X-axis. **(b)** Y-axis.

Figure 74: Three lens setup B: Irradiance along both axes at multiple detector surfaces D_i for configuration one with respect to Gaussian illumination in NSQ mode.

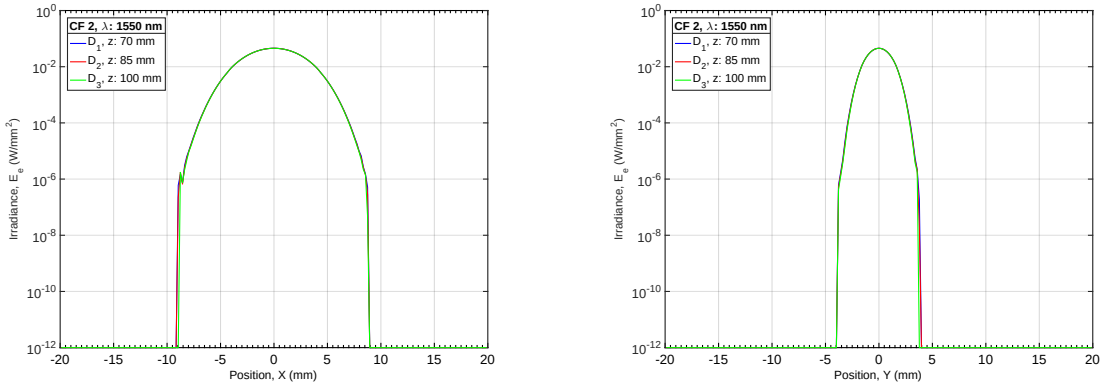

(a) X-axis. **(b)** Y-axis.

Figure 75: Three lens setup B: Irradiance along both axes at multiple detector surfaces D_i for configuration two with respect to Gaussian illumination in NSQ mode.

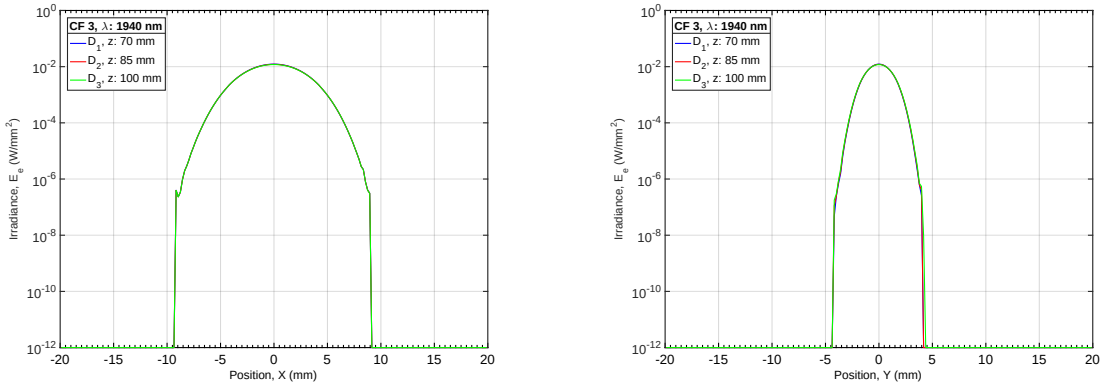

(a) X-axis. **(b)** Y-axis.

Figure 76: Three lens setup B: Irradiance along both axes at multiple detector surfaces D_i for configuration three with respect to Gaussian illumination in NSQ mode.

APPENDIX B

Component and Material Selection

B.1 Laser Window Heating Methods

Joule Heating

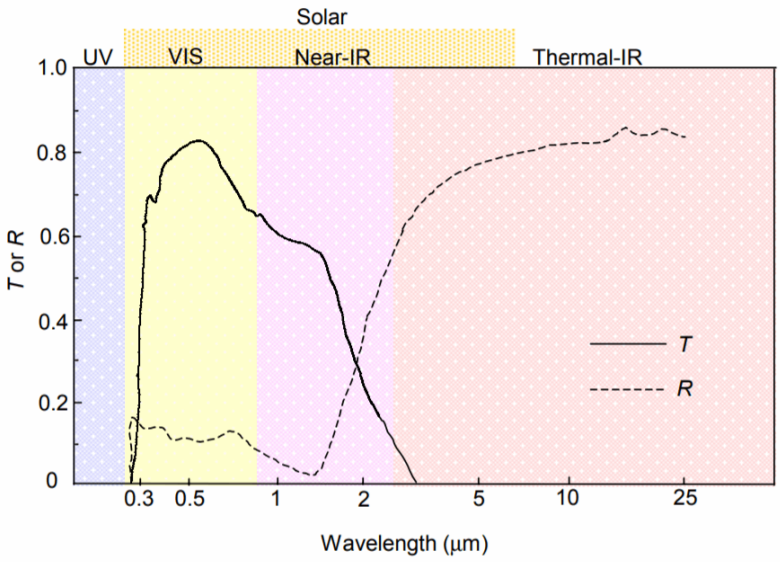

Figure 77: Resistive heating concept: Variation of transmission T and reflectance R over wavelength λ for ITO. Figure reprinted from reference [40].

ITO thin films have been widely used as transparent conducting oxide in research and industry. Solar cells, flat panel displays [40, 54, 66] and organic light emitting diode (OLED) displays [55, 109] are among the most important applications.
As mentioned in Section 3.2.3, the high transmission in the visible region combined with

high electrical conductivity is primarily based on its highly degenerative behavior as a heavily doped n-type semiconductor. Its tunable work function is approximately in the range of (3.5 to 4.3) eV [54]. The electrical and optical properties of ITO show a strong dependency on its structure, Sn and O_2 content, deposition conditions and growth techniques [33, 55, 70, 78, 119].

Figure 77 illustrates the variation of transmission and reflectance over wavelength for ITO thin films. It shows a high optical transmission in the visible and NIR and high reflectance in the IR region. In the ultraviolet, ITO thin films show an opaque character. Further information about the change in transmission T and reflection R for ITO films with respect to its thickness, Sn concentration and sheet resistance can be found in [40, 72].

Mount Heating

All components used for the mount heating concept are listed in Table 23. As mentioned in Section 3.2.2, the window dimensions are $(21.2 \times 14 \times 3)$ mm. The production tolerance of $\pm$ 0.1 mm and $\pm$ 0.2 mm in dimensions and thickness, respectively, was defined by the company *Edmund Optics, Inc.*

Table 23: List of components for the laser window mount heating concept.

Item	Specifications	Manufacturer	Qty.
HT15W	15 W resistive cartridge heater, ∅3.1 mm x 12.7 mm	*Thorlabs, Inc*	4
PT100	Temperature sensor, M3, 250 °C max. temperature	*AVL List GmbH*	3
49-470	N-BK7® window, $\lambda/4$ surface flatness, uncoated	*Edmund Optics, Inc*	6
TR-81	*A-Senco* temperature controller for PT100 sensors	*Pohltechnic.com GbR*	1

APPENDIX C

Measurement Setup Realization

This chapter consists of the components and tools used for the LD adaptation and optical setup realization as discussed in Section 3.3. The list of components is divided into four major parts as seen in Table 24. Part one covers the FC/PC-SMA custom MM fiber and the associated mating sleeve properties. The remaining sections feature all elements of the cage system, lens tube and optical setup employed during the *SolidWorks* design procedure. Additional lens parameters for uniform and Gaussian illumination can be found in Section 3.1.5, Tables 10 and 11. All components listed in this chapter are manufactured and distributed by *Thorlabs, Inc.*

Table 24: List of components for the LD adaptation and the optical setup realization.

FC/PC to SMA

Item	Specifications	Qty.
ADAFC2	FC/PC to FC/PC mating sleeve, wide key 2.2 mm	1
FG200LEA	MM fiber, NA: 0.22, 200 µm Core, (400 to 2400) nm	1

Cage system

Item	Specifications	Qty.
ER6E	Engraved cage assembly rod, 6 " long, ∅6 mm	4
SM2A21	Externally SM2-threaded 2 " mounting adapter, ∅1.20 " bore	1
LCP06/M	60 mm cage plate with ∅2 " double-bore optic mount, M4 tap	1
LCP01/M	60 mm cage plate, SM2 threads, 0.5 " thick, M4 tap	1
LCRM2/M	60 mm cage rotation mount for ∅2 " optics, M4 tap	1

Continued on next page.

Table 24 – *Continued from previous page.*

Item	Specifications	Qty.
CYLCP/M	60 mm cage mount for cylindrical lenses, M4 Tap	2

Lens tube

Item	Specifications	Qty.
SM1M15	SM1 lens tube without external threads, 1.5 " long	2
SM1RR	SM1 retaining ring for ∅1 " lens tubes and mounts	4
SM1SMA	SMA fiber adapter plate with external SM1 thread	2
SM1AD10	Externally SM1-threaded adapter for ∅10 mm optic, 0.4 " thick	1
SM1AD15	Externally SM1-threaded adapter for ∅15 mm optic, 0.4 " thick	1

Optics

Item	Specifications	Qty.
ACL108U	B270 aspheric condenser lens, ∅10 mm, FL: 8 mm, NA: 0.61	1
ACL1512U	B270 aspheric condenser lens, ∅15 mm, FL: 12 mm, NA: 0.61	1
LK1900L1-C	N-BK7® plano-concave cylindrical lens, FL: 25.4 mm	1
LK1037L1-C	N-BK7® plano-concave cylindrical lens, FL: −19 mm	1
LJ1430L1-C	N-BK7® plano-convex cylindrical lens, FL: 60 mm	1

APPENDIX D

Laser Diode Characterization

D.1 Laser Diode Characteristics

Table 25 displays all three fiber-coupled LDs with the corresponding mount and the LD/TEC controller. Detailed LD parameter specifications are listed in Table 2. Additional information about the PM16-401 power meter, LMR1/M mount and SMA fiber adapter plate can be found in Tables 24 and 26.

Table 25: List of components for the I-V-P characteristics analysis.

Item	Specifications	Manufacturer	Qty.
NLK1E5GAAA	DFB-LD in a butterfly 14-pin package SM pigtail fiber with FC/PC λ: (1364.69 ± 1.00) nm	*NEL*	1
LM14S2	14-pin butterfly mount	*Thorlabs, Inc*	1
FLX-1550-840M-FC200	FP-LD with 9 mm FC-SMA package MM fiber, λ: (1550 ± 20) nm	*FLC*	1
TCLDM9	Temperature cooled mount for $\varnothing$9 mm transistor outline LD	*Thorlabs, Inc*	1
LQ5-1940-200/HHL-FSMA	FP-LD with FSMA package MM fiber, λ: (1940 ± 10) nm	*OECA*	1
LDM-4442	High heat load (HHL) mount	*Newport C.*	1
ITC4005	Benchtop LD/TEC controller 5 A/225 W	*Thorlabs, Inc*	1

D.2 Beam Profile Analysis

This section displays all components and alignment tools used for the beam profiling analysis in Section 3.5. All elements listed in Table 26 are distributed by *Thorlabs, Inc* and *Qioptiq Photonics GmbH*. The measurement setup was realized by using the same 60 mm cage system components as described in Appendix C, Table 24.

Table 26: List of components for the beam profile analysis.

Thorlabs, Inc

Item	Specifications	Qty.
FTFC1	FC/PC fiber optic light trap	1
ADAFCSMA1	FC/PC to SMA fiber optic mating sleeve	1
LB2/M	Beam block, (1 to 12) µm, 80 W max. avg. power, pulsed and CW	1
VRC2	VIS/IR detector card, (400 to 640) nm, (800 to 1700) nm	1
VRC6S	MIR liquid crystal detector card, (1.5 to 13.2) µm	1
PM16-401	USB power meter, thermal sensor, (0.19 to 20) µm, 1 W max.	1
LMR1/M	Lens mount with retaining ring for ∅1 " optics, M4 tap	1
BC106N-VIS/M	CCD camera beam profiler, VIS, (350 to 1100) nm	1
XYR1/M	XY stage with ∅1 " hole, 13 mm travel, 360 ° rotation	1
RLA600/M	Dovetail optical rail, 600 mm	1
RC1	Dovetail rail carrier, (1 × 1) "	1
FP01	Plate holder, 0.9 " wide, holds plates up to 0.58 " thick	1

Qioptiq Photonics GmbH

Item	Specifications[27]	Qty.
NANO 250	Module 250-405-160, λ : (405 ± 5) nm, output power 160 mW Fundamental Gaussian mode TEM_{00}, divergence < 0.8 mrad	1

Regular chrome platinum double edge razor blades by *Socieété BIC S.A* were used as apertures for all beam profiling methods and tests. Additional posts, post holders and mounting plates manufactured by *Thorlabs, Inc* were implemented in the setup. For the validation measurement, a center wavelength of 402 nm was assumed. The actual beam profile analysis, discussed in Section 4.3.2, was performed on LD three. LD specifications and LD/TEC controller details can be seen in Tables 2 and 25.

[27] LD specifications: *Qioptiq Photonics GmbH* (May, 2012).

D.2.1 Error Function

As seen in Section 2.4, the error function was used to solve the integrals for total and transmitted beam power as a function of knife-edge displacement. The error function shows a sigmoidal behavior and is defined as

$$\mathrm{erf} = \frac{1}{\sqrt{\pi}} \int_{-x}^{x} \exp\left(-t^2\right) \mathrm{d}t \tag{D.1}$$

$$\mathrm{erf} = \frac{2}{\sqrt{\pi}} \int_{0}^{x} \exp\left(-t^2\right) \mathrm{d}t \tag{D.2}$$

with the properties

$$\mathrm{erf}(-\infty) = -1 \tag{D.3}$$

$$\mathrm{erf}(+\infty) = +1 \tag{D.4}$$

$$\mathrm{erf}(-x) = -\,\mathrm{erf}(x) \tag{D.5}$$

$$\mathrm{erf}(\overline{x}) = \overline{\mathrm{erf}(x)}. \tag{D.6}$$

Figure 78 illustrates the error function $\mathrm{erf}(x)$ over the interval $[-3, 3]$ for x. The complementary error function is obtained by

$$\mathrm{erfc} = \frac{2}{\sqrt{\pi}} \int_{x}^{\infty} \exp\left(-t^2\right) \mathrm{d}t = 1 - \mathrm{erf}\,. \tag{D.7}$$

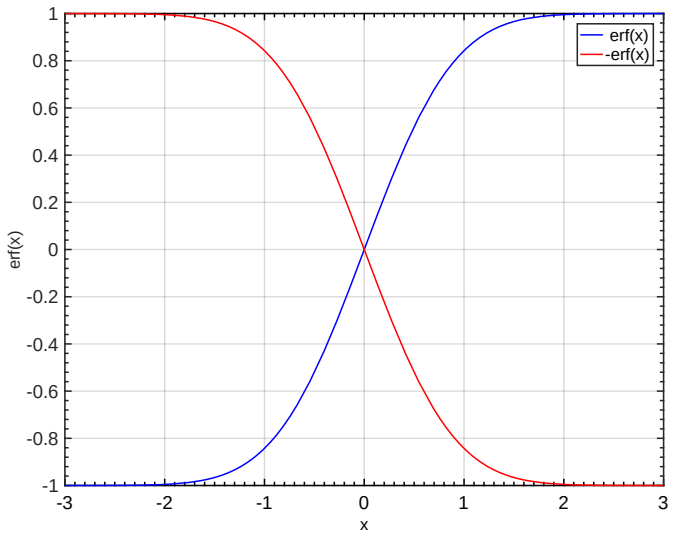

Figure 78: Error function: Graphical illustration in the range of ± x.

D.2.2 Beam Profiler

The BC106N, a charge-coupled device (CCD) camera based beam profiler by *Thorlabs, Inc*, was used for the validation measurements in the visible part of the electromagnetic spectrum (VIS). All specifications are based on the reference [110].

Technical Data

Sensor			Model		
Sensor resolution	:	(1360×1024) pixel	Wavelength range	:	(350 to 1100) nm
Pixel size	:	(6.45×6.45) µm	Power range	:	1 fW to 1 W
Aperture	:	(8.77×6.66) mm	Beam diameter	:	(0.03 to 6.66) mm

The x- and y-profile of the 2D laser beam are part of the standard GUI in the *Thorlabs Beam* software[28]. Two things have to be considered while using this measurement feature with respect to the data analysis:

1. **Measurement Type**
   "The X profile displays a single pixel row taken from the received camera image, while the Y profile shows a single pixel column. The column and row are defined by the position of cross hair within the 2D Projection graph [110, p. 61]."

2. **Scaling**
   "If "Autoscale to Peak" is enabled and the cross hair in 2D projection is fixed to peak, the measured curve shows relative intensities from 0 to 100 %, where 100 % denotes the maximum value in the selected row / column [110, p. 61]."

In order to obtain a more comprehensive and accurate x- and y-profile, the whole laser beam needs to be considered. Furthermore, the actual sensor position within the beam profile plays a crucial role for the alignment:

> "The sensor is centered with respect to the holes in the mounting base, its depth measured from the front surface of the filter wheel is 12.2 mm [0.48 inches]; from the front of the BC106N housing - 5.0 mm [0.20 inches] [110, p. 20]."

[28] (2017), *Thorlabs Beam* (6.0.785.2502), *Thorlabs, Inc.* [Software] Accessed: April, 2017.

D.2.3 Validation Tests

Additional data analysis results for each beam profiling method are presented in this section. Further information about each technique can be found in Section 3.5.1.

D.2.3.1 Scanning Slit Method

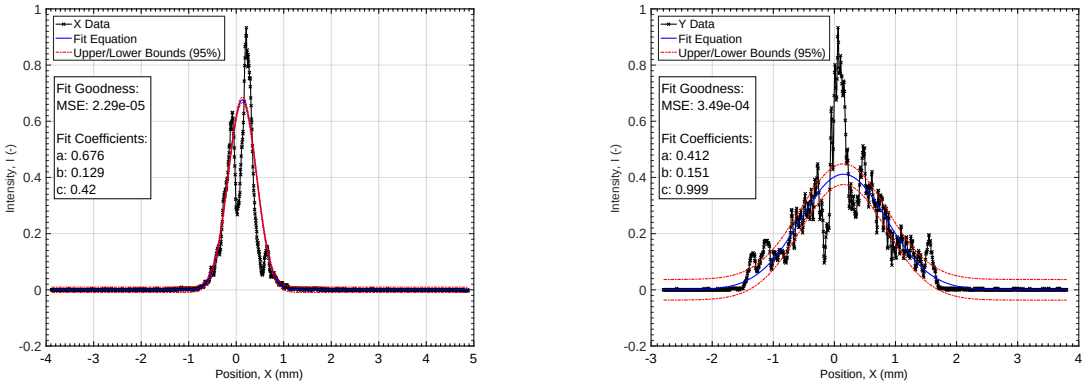

(a) X-profile. **(b)** Y-profile.

Figure 79: SSM: Reference measurement data fitting results in accordance with the Gaussian model for both axes.

D.2.3.2 Knife-Edge Method

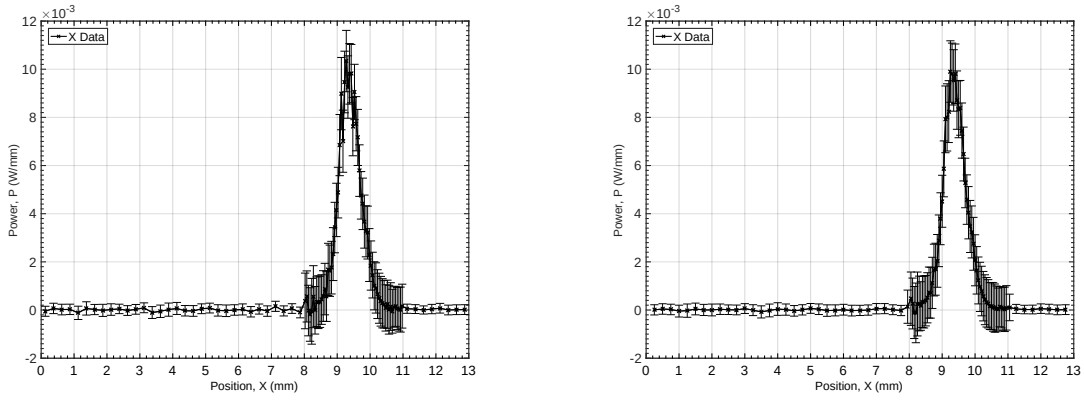

(a) Derivative of data. **(b)** Averaged derivative of data.

Figure 80: KEM: Data evaluation results inclusive error calculation of methods two and three for the x-profile.

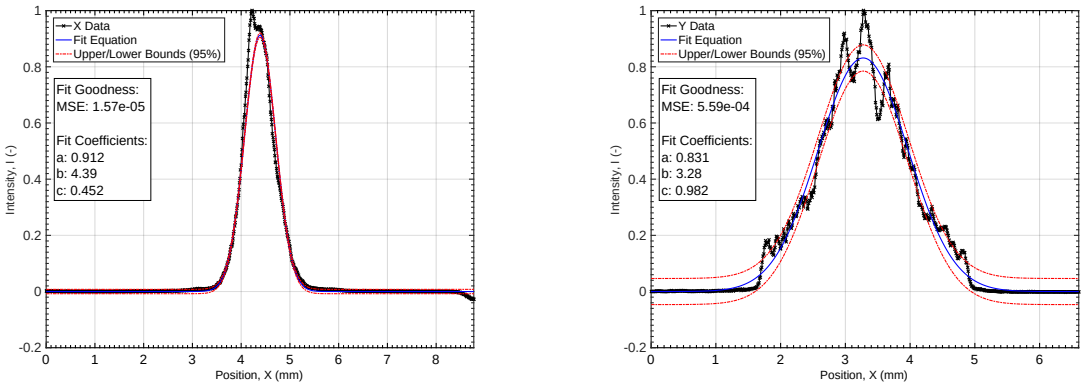

(a) X-profile. **(b)** Y-profile.

Figure 81: KEM: Normalized reference measurement data fitting results in accordance with the Gaussian model for both axes.

D.2.4 Beam Profiling Measurements

This section provides supplemental data analysis results for all beam profiling measurements on LD three with a center wavelength of 1940 nm. A more detailed description can be found in Section 3.5.2.

D.2.4.1 Laser Diode

Figures 82 to 85 display the evaluated experimental data according to methods two and three for the x- and y-profile at measurement points P_i.

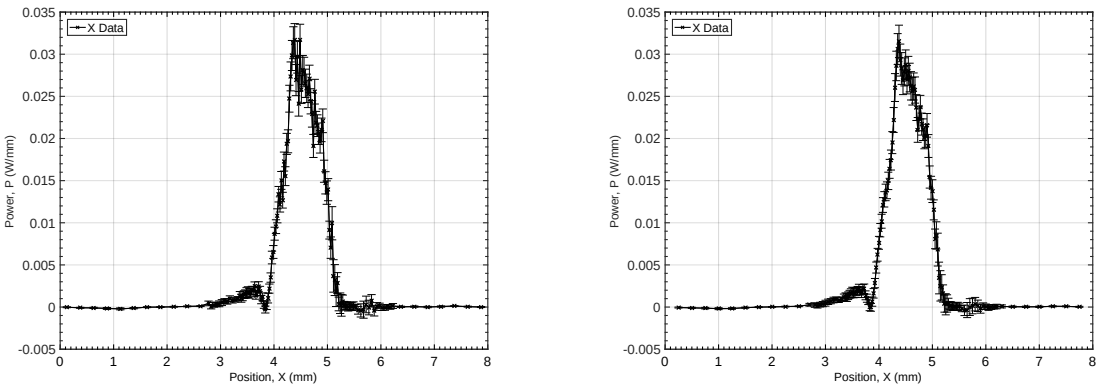

(a) Derivative of data. **(b)** Averaged derivative of data.

Figure 82: LD: Data evaluation results inclusive error calculation of methods two and three for the x-profile at measurement point P_1.

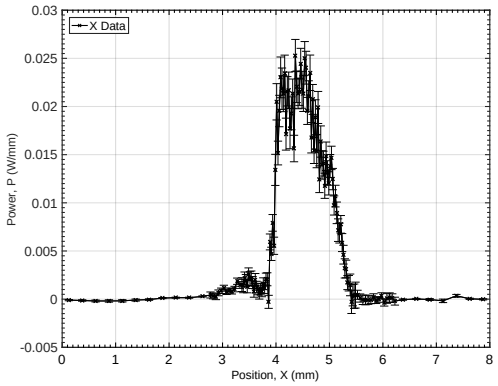

(a) Derivative of data.

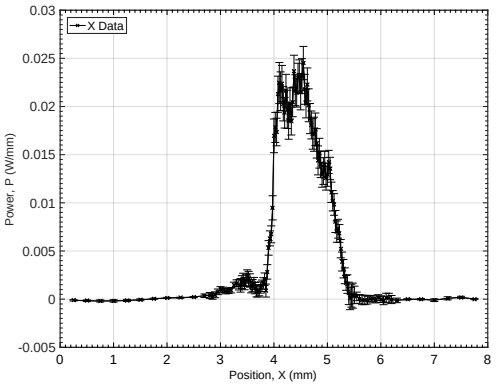

(b) Averaged derivative of data.

Figure 83: LD: Data evaluation results inclusive error calculation of methods two and three for the x-profile at measurement point P_2.

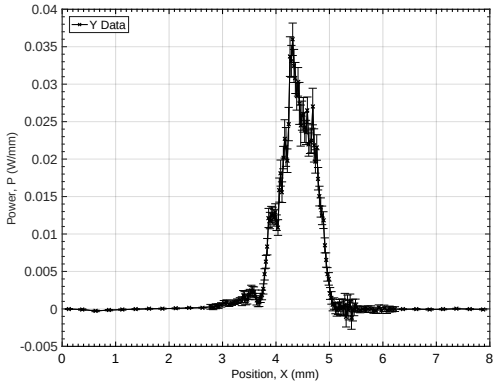

(a) Derivative of data.

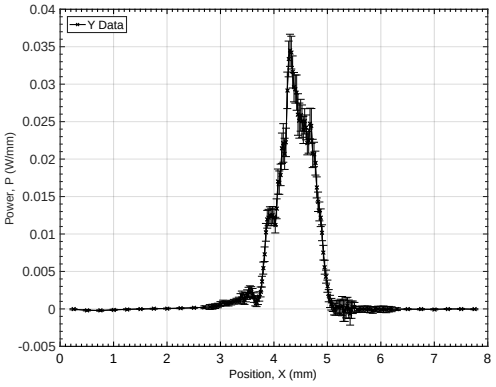

(b) Averaged derivative of data.

Figure 84: LD: Data evaluation results inclusive error calculation of methods two and three for the y-profile at measurement point P_1.

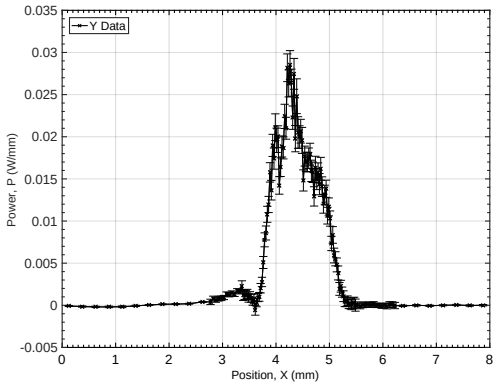

(a) Derivative of data.

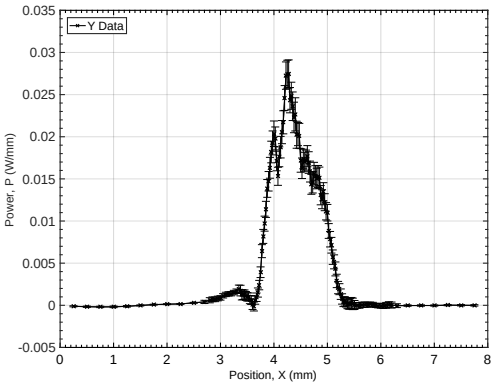

(b) Averaged derivative of data.

Figure 85: LD: Data evaluation results inclusive error calculation of methods two and three for the y-profile at measurement point P_2.

D.2.4.2 Laser Diode with Aspheric Condenser Lens

Figures 86 to 89 present the obtained data analysis results in accordance with methods two and three for the x- and y-profile at measurement points P_i. In addition, the shape-preserving piecewise cubic interpolation results are highlighted in Figures 90 and 91. The red curve illustrates the interpolation of the whole data set, whereas the blue point indicates the interpolated $1/e^2$ beam radius.

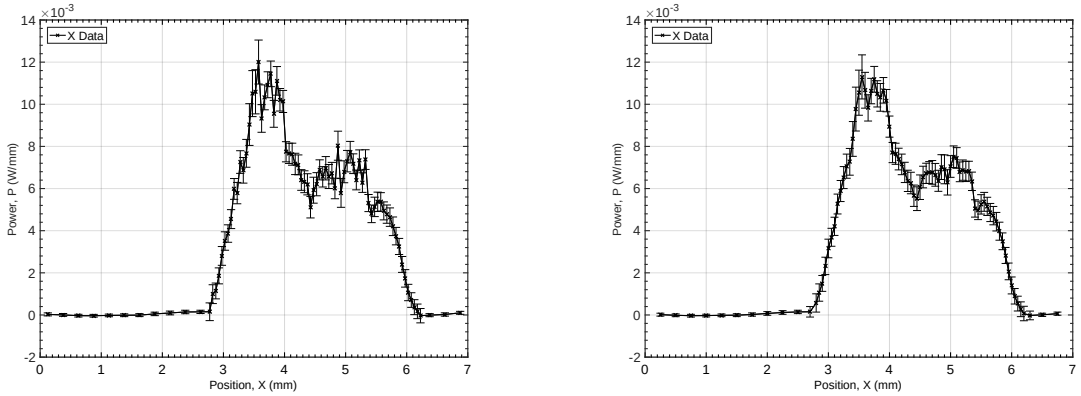

(a) Derivative of data. **(b)** Averaged derivative of data.

Figure 86: LD with AL: Data evaluation results inclusive error calculation of methods two and three for the x-profile at measurement point P_1.

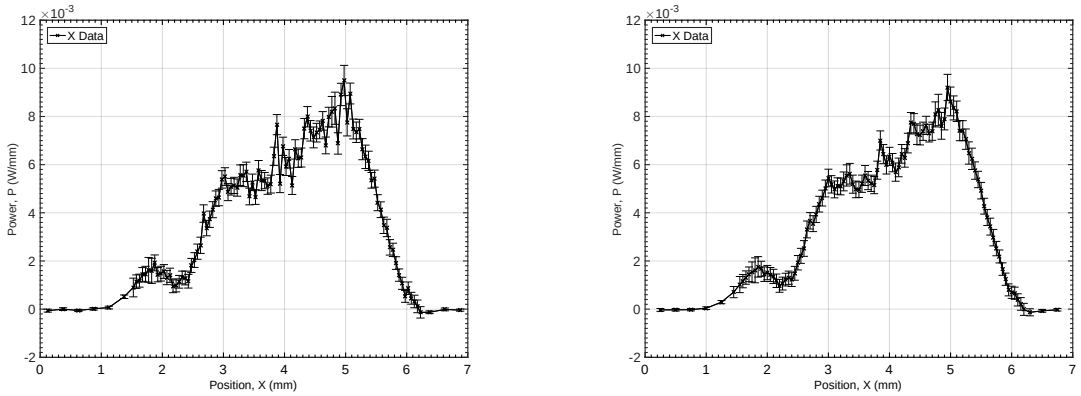

(a) Derivative of data. **(b)** Averaged derivative of data.

Figure 87: LD with AL: Data evaluation results inclusive error calculation of methods two and three for the x-profile at measurement point P_2.

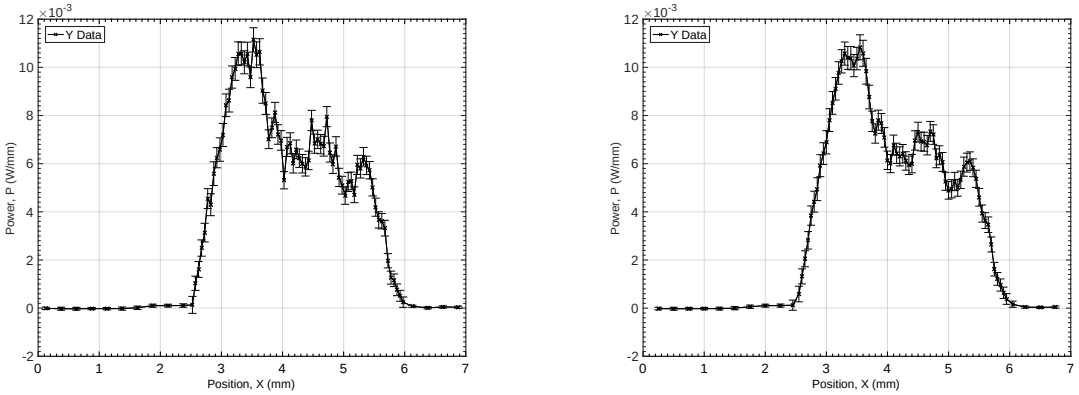

(a) Derivative of data. **(b)** Averaged derivative of data.

Figure 88: LD with AL: Data evaluation results inclusive error calculation of methods two and three for the y-profile at measurement point P_1.

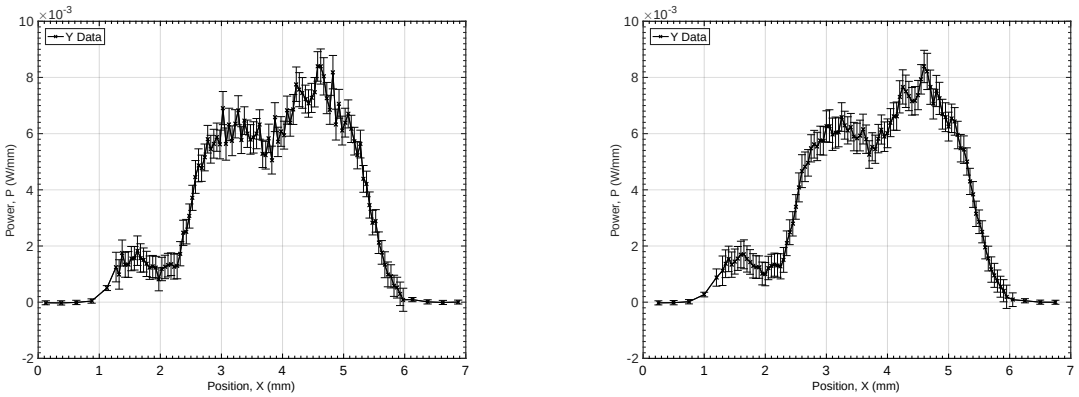

(a) Derivative of data. **(b)** Averaged derivative of data.

Figure 89: LD with AL: Data evaluation results inclusive error calculation of methods two and three for the y-profile at measurement point P_2.

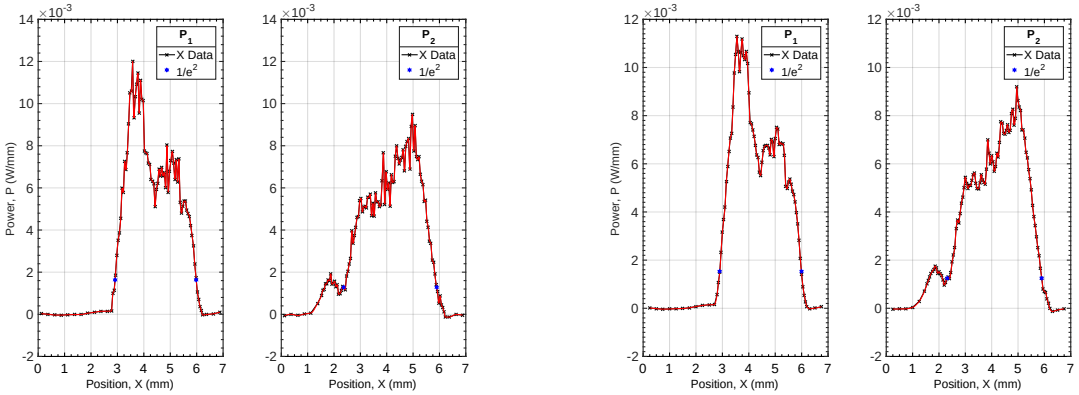

(a) Derivative of data. **(b)** Averaged derivative of data.

Figure 90: LD with AL: Beam radius interpolation results of the evaluated data in accordance with methods two and three for the x-profile at measurement points P_i.

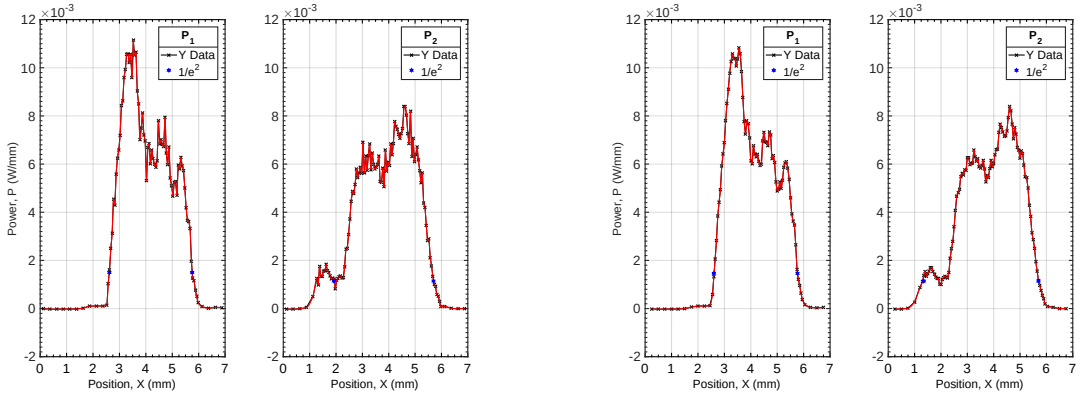

(a) Derivative of data.

(b) Averaged derivative of data.

Figure 91: LD with AL: Beam radius interpolation results of the evaluated data in accordance with methods two and three for the y-profile at measurement points P_i.

D.3 Data Analysis

As mentioned in Sections 3.4 and 3.5, for all LD characterization measurements a certain number of sample points were recorded for each measurement step by the power meter. The AM is defined by

$$\overline{x} = \frac{1}{N} \sum_{i=1}^{N} x_i \tag{D.8}$$

for a data set containing the values $x_1, x_2, ..., x_N$. The parameter N is the total number of values in this specific data set. The corresponding SD is given by Equation (D.9), where $\overline{x}$ represents the mean value of all samples.

$$\sigma = \sqrt{\frac{\sum_{i=1}^{N} (x_i - \overline{x})^2}{N-1}} \tag{D.9}$$

APPENDIX E

Validation Test

All main components regarding the optical setup, window heating concept, measurement realization and alignment tools are displayed in Appendices B to D. The DFB-LD specifications, provided by *NTT Electronics (NEL) Corporation*, and LD/TEC controller details can be seen in Tables 2 and 25. Additional components required for the PA measurement are listed in this section.

Table 27: List of components for the PA validation test in humid environment.

Item	Specifications	Manufacturer	Qty.
CompactRIO	FPGA based lock-in amplifier I/O modules, *LabVIEW* GUI	*National Instruments Corporation*	1
SHT31	USB evaluation kit (EK-H5) Range: (0 to 100) % rH Response time: $\tau_{63} < 8\,\mathrm{s}$ Error: ± 2 % rH (95 % CIs)	*Sensirion AG*	1
ATHMOS/MK/T–1502–1	aSTEAM direct evaporator Evap. rate: (25 to 1000) g/h	*aDROP Feuchtemeßtechnik GmbH*	1
Simdos 10	Dosing pump for fluids Pump. speed: (1 to 100) m L	*KNF Neuberger GmbH*	1
GSC-C9TA-BB12	MFC, red-y smart series Std. flow rate: 25 L/min	*Vögtlin Instruments GmbH*	1
WB 63 A2 STP	Oil-free vacuum pump Inlet capacity: $25\,\mathrm{m}^3/\mathrm{h}$	*Becker GmbH*	1
EK-23028-000	Subminiature microphone	*Knowles Electronics*	1

The humidity generation concept is described in great depth in the master's thesis by *Anton Buchberger*. Further information about the PA theoretical background and design process of the developed PA resonant cell can be retrieved from the ongoing dissertation by *Benjamin Lang*.

E.1 Laser Diode Tuning

Figure 92 illustrates the obtained lock-in PA signal amplitude and phase over the LD operating temperature. Error bars represent the SD of all recorded sample points per measurement increment. This temperature sweep was performed to localize the maximum PA signal amplitude as a function of the LD operating temperature.

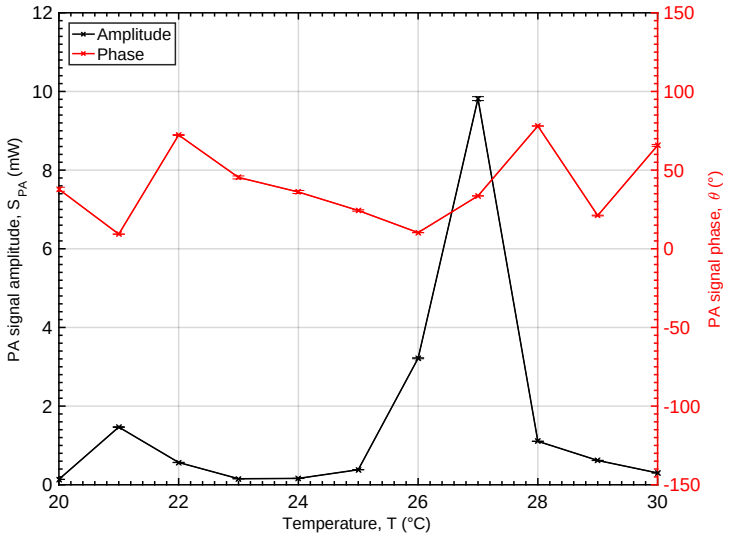

Figure 92: LD tuning: Lock-in PA signal amplitude and phase over the LD operating temperature [(20 to 30) °C].

HITRAN

It represents an online database of spectroscopic parameters. All absorption characteristics used in this work are based on the 2012 and 2016 edition of the HITRAN molecular spectroscopic compilation [34, 35]. In addition, HITRAN *on the Web* [41] was used to obtain spectroscopic parameters within a specified spectral range based on the 2012 edition. As mentioned in Section 3.6.2, LD tuning was performed in ambient air at room temperature. The rH of the ambient air was sufficient for the optimization of the PA signal amplitude as a function of operating temperature. Hence, the experimental data

was compared to the atmospheric gas mixture over a specific wavenumber $\tilde{\nu}$ range using HITRAN *on the Web* with the following specifications:

Title: USA model, mean latitude, summer, H=0

Mixing ratio, (%): H_2O: 1.860 000, CO_2: 0.033 000, O_3: 0.000 003, N_2O: 0.000 032, CO: 0.000 015, CH_4: 0.000 170, O_2: 20.900 001, N_2: 77.206 000

Various parameters: $\tilde{\nu}$ range: (7325 to 7330) cm^{-1}, T: (296 and 298) K, P: 101 325 Pa, $\tilde{\nu}$ step: 0.008 76 cm^{-1}, Profile: Voigt, Wing: 50 HW, S_{cut}: 1×10^{-28} cm/mol

E.2 Photoacoustic Measurement

The obtained residuals for the second degree polynomial function according to Equation (3.18) are displayed in Figure 93. Error bars cover the humidity sensor uncertainty (± 2 % rH) [97] and the SD of all recorded sample points per measurement increment.

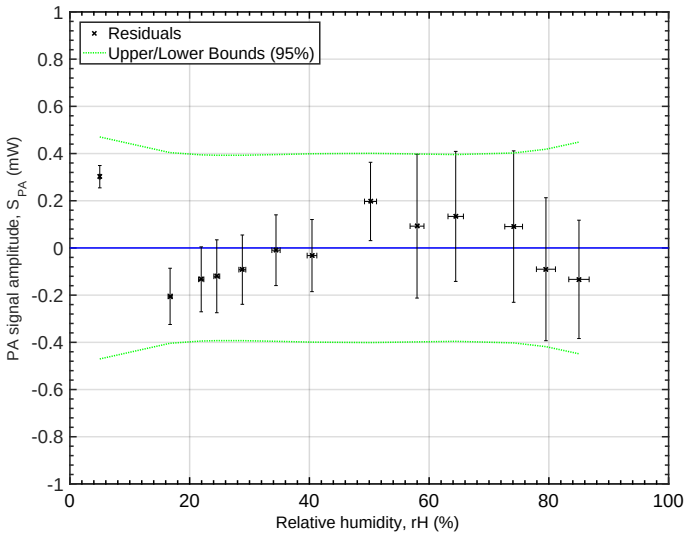

Figure 93: PA measurement: Residual analysis for the second degree polynomial function of the experimental data with 95 % prediction bounds for new observations.

It is apparent from this figure that all experimental data are within the 95 % prediction half-widths for new observations. Further improvement of the alignment of the fit can be achieved by applying higher order polynomials.

Bibliography

[1] Abramczyk, H. (2005), *Introduction to laser spectroscopy*, Elsevier, chapter: 1-2, pp. 1–30.

[2] András Miklós, S. S. and Hess, P. (1999), Photoacoustic spectroscopy, *in* 'Theory, Encyclopedia of spectroscopy and spectrometry', Academic Press, New York, pp. 1815–1822.

[3] Arora, A. (2014), 'What is non-sequential ray tracing?', Zemax Knowledgebase. [Online] Accessed: 2018-03-01.
URL:`http://customers.zemax.com/os/resources/learn/knowledgebase/exploring-non-sequential-mode-in-zemax`

[4] Barbir, F. (2013), *PEM Fuel Cells Theory and Practice*, second edition edn, Academic Press, Boston.

[5] Baudelet, M. (2014), *Laser Spectroscopy for Sensing: Fundamentals, Techniques and Applications*, Elsevier, chapter: Photoacoustic spectroscopy, pp. 208–234.

[6] Bell, A. G. (1880), 'On the production and reproduction of sound by light', *American Journal of Science* **20**(118), 305–324.

[7] Bell, A. G. (1881), 'Lxviii. upon the production of sound by radiant energy', *The London, Edinburgh, and Dublin Philosophical Magazine and Journal of Science* **11**(71), 510–528.

[8] Bernath, P. F. (2005), *Spectra of atoms and molecules*, Oxford University Press.

[9] Bernegger, S. (1988), CO-laser photoacoustic spectroscopy of gases and vapors for trace gas analysis, PhD thesis, ETH Zurich. Diss. Naturwiss. ETH Zürich, Nr. 8636, 1988. Ref.: M. W. Sigrist ; Korref.: F. K. Kneubühl.

[10] Besson, J.-P. (2006), Photoacoustic spectroscopy for multi-gas sensing using near infrared lasers, PhD thesis, EPFL.

[11] Bhattacharya, P. (2015), 'Water flooding in the proton exchange membrane fuel cell'. [Online] Accessed: 2018-07-21.
URL:`https://www.sciencetheearth.com/uploads/2/4/6/5/24658156/waterflooding_protonexchangemembrane.pdf`

[12] Bonneville, C. (2016), 'Tuning a dfb laser diode with temperature'. [Online] Accessed: 2018-08-02.
URL:`http://mylaserspectrum.com/2016/03/dfb-laser-one-wavelength-two-wavelengths-one-mode-two-modes/`

[13] Bozóki, Z., Sneider, J., Gingl, Z., Árpád Mohácsi, Szakáll, M., Bor, Z. and Szabó, G. (1999), 'A high-sensitivity, near-infrared tunable-diode-laser-based photoacoustic water-vapour-detection system for automated operation', *Measurement Science and Technology* **10**(11), 999.
URL:`http://stacks.iop.org/0957-0233/10/i=11/a=304`

[14] Bozóki, Z., Szakáll, M., Mohácsi, Á., Szabó, G. and Bor, Z. (2003), 'Diode laser based photoacoustic humidity sensors', *Sensors and Actuators B: Chemical* **91**(1-3), 219–226.

[15] Buchberger, A. (2018), Development and charaterization of a humidity measurement system based on polymeric hydrogels, Master's thesis, Graz University of Technology. Institute of Solid State Physics.

[16] Büchi, F. N., Inaba, M. and Schmidt, T. J. (2009), *Polymer electrolyte fuel cell durability*, Springer, chapter: Impact of Contaminants, pp. 289–366.

[17] Cantle, J. E. (1986), *Atomic absorption spectrometry*, Vol. 5, Elsevier, chapter: Basic Principles by J.W.Robinson, pp. 1–14.

[18] Castanheira, L., Silva, W. O., Lima, F. H., Crisci, A., Dubau, L. and Maillard, F. (2015), 'Carbon corrosion in proton-exchange membrane fuel cells: Effect of the carbon structure, the degradation protocol, and the gas atmosphere', *ACS Catalysis* **5**(4), 2184–2194.
URL:`https://doi.org/10.1021/cs501973j`

[19] Chapple, P. B. (1994), 'Beam waist and M^2 measurement using a finite slit', *Optical Engineering* **33**, 33 – 33 – 6.

[20] Chen, D. and Peng, H. (2005), 'A thermodynamic model of membrane humidifiers for pem fuel cell humidification control', *Journal of dynamic systems, measurement, and control* **127**(3), 424–432.

[21] Collegeman, A. (2017), *OpticStudio 16.5 SP3 Help Files*, Zem,ax, LLC, Kirkland, WA.

[22] Cooper, K. and Smith, M. (2006), 'Electrical test methods for on-line fuel cell ohmic resistance measurement', *Journal of Power Sources* **160**(2), 1088–1095.

[23] de Araújo, M. A., Silva, R., de Lima, E., Pereira, D. P. and de Oliveira, P. C. (2009), 'Measurement of gaussian laser beam radius using the knife-edge technique: improvement on data analysis', *Appl. Opt.* **48**(2), 393–396.

[24] Demtröder, W. (2003), *Laser Spectroscopy: Basic Concepts and Instrumentation*, Vol. 1, 3 edn, Springer.

[25] Dessler, A., Schoeberl, M., Wang, T., Davis, S. and Rosenlof, K. (2013), 'Stratospheric water vapor feedback', *Proceedings of the National Academy of Sciences* **110**(45), 18087–18091.

[26] Dewey, C. F., Kamm, R. D. and Hackett, C. E. (1973), 'Acoustic amplifier for detection of atmospheric pollutants', *Applied Physics Letters* **23**(11), 633–635. **URL:**`https://doi.org/10.1063/1.1654774`

[27] Dumitras, D., Dutu, D., Matei, C., Magureanu, A., Petrus, M. and Popa, C. (2007), 'Laser photoacoustic spectroscopy: principles, instrumentation, and characterization', *Journal of Optoelectronics and Advanced Materials* **9**(12), 3655.

[28] Fahey, D., Gao, R.-S., Möhler, O., Saathoff, H., Schiller, C., Ebert, V., Krämer, M., Peter, T., Amarouche, N., Avallone, L. et al. (2014), 'The aquavit-1 intercomparison of atmospheric water vapor measurement techniques', *Atmospheric Measurement Techniques* **7**(9), 3177–3213.

[29] Farahani, H., Wagiran, R. and Hamidon, M. N. (2014), 'Humidity sensors principle, mechanism, and fabrication technologies: a comprehensive review', *Sensors* **14**(5), 7881–7939.

[30] Fiedler, M. and Hess, P. (1989), *Laser Excitation of Acoustic Modes in Cylindrical and Spherical Resonators: Theory and Applications*, Springer Berlin Heidelberg, Berlin, Heidelberg, pp. 85–123.

[31] Fischmeister, H. and Roll, U. (1984), 'Passivschichten auf rostfreien Stählen: Eine Übersicht über oberflächenanalytische Ergebnisse', *Fresenius' Zeitschrift für analytische Chemie* **319**(6), 639–645.

[32] Gillen, G. D., Gillen, K. and Guha, S. (2017), *Light propagation in linear optical media*, CRC Press.

[33] Girtan, M., Rusu, G., Rusu, G. and Gurlui, S. (2000), 'Influence of oxidation conditions on the properties of indium oxide thin films', *Applied surface science* **162**, 492–498.

[34] Gordon, I. E., Rothman, L. S., Babikov, Y., Barbe, A., Benner, D. C., Bernath, P. F., Birk, M., Bizzocchi, L., Boudon, V., Brown, L. R. et al. (2013), 'The HITRAN2012 molecular spectroscopic database', *Journal of Quantitative Spectroscopy and Radiative Transfer* **130**, 4–50.

[35] Gordon, I. E., Rothman, L. S., Hill, C., Kochanov, R. V., Tan, Y., Bernath, P. F., Birk, M., Boudon, V., Campargue, A., Chance, K. et al. (2017), 'The HITRAN2016 molecular spectroscopic database', *Journal of Quantitative Spectroscopy and Radiative Transfer* **203**, 3–69.

[36] Görgün, H., Arcak, M. and Barbir, F. (2006), 'An algorithm for estimation of membrane water content in pem fuel cells', *Journal of power sources* **157**(1), 389–394.

[37] Grundy, W. and Schmitt, B. (1998), 'The temperature-dependent near-infrared absorption spectrum of hexagonal h2o ice', *Journal of Geophysical Research: Planets* **103**(E11), 25809–25822.

[38] Harren, F. J. M., Berkelmans, R., Kuiper, K., te Lintel Hekkert, S., Scheepers, P., Dekhuijzen, R., Hollander, P. and Parker, D. H. (1999), 'On-line laser photoacoustic detection of ethene in exhaled air as biomarker of ultraviolet radiation damage of the human skin', *Applied Physics Letters* **74**(12), 1761–1763.
URL:`https://doi.org/10.1063/1.123680`

[39] Harren, F. J. M., Reuss, J., Woltering, E. J. and Bicanic, D. D. (1990), 'Photoacoustic measurements of agriculturally interesting gases and detection of c2h4 below the ppb level', *Applied Spectroscopy* **44**(8), 1360–1368.
URL:https://doi.org/10.1366/000370290789619522

[40] Hartnagel, H., Dawar, A., Yain, A. and Jajadish, C. (1995), *Semiconducting transparent thin films*, CRC Press.

[41] Harvard-Smithsonian Center for Astrophysics (USA), V.E. Zuev Insitute of Atmosperic Optics (Russia) and National Research Tomsk State University (Russia) (2016), 'HITRAN on the Web 2.0'.
URL:http://hitran.iao.ru/

[42] Hasegawa, T., Imanishi, H., Nada, M. and Ikogi, Y. (2016), Development of the fuel cell system in the mirai fcv, *in* 'SAE Technical Paper', SAE International.
URL:https://doi.org/10.4271/2016-01-1185

[43] Haynes, W. M. (2014), *CRC handbook of chemistry and physics*, CRC press.

[44] Heisenberg, W. (1927), 'Über den anschaulichen inhalt der quantentheoretischen kinematik und mechanik', *Zeitschrift für Physik* **43**, 172–198.

[45] Hertel, I. V. and Schulz, C.-P. (2014), *Atoms, Molecules and Optical Physics 1*, Springer.

[46] Hess, P. (1983), Resonant photoacoustic spectroscopy, *in* 'Physical and Inorganic Chemistry', Springer Berlin Heidelberg, Berlin, Heidelberg, pp. 1–32.

[47] Hribšek, M. F., Tošić, D. V. and Radosavljević, M. R. (2010), 'Surface acoustic wave sensors in mechanical engineering', *FME transactions* **38**(1), 11–18.

[48] Ide, R. F. (1999), Comparison of liquid water content measurement technquies in an icing wind tunnel, Technical report, NATIONAL AERONAUTICS AND SPACE ADMINISTRATION CLEVELAND OH LEWIS RESEARCH CENTER.

[49] IDEX, C. (2014), 'Gaussian beam optics', Gaussian beam propagation, A158–A163, Figure 5.4. [Online] Accessed: 2018-02-01.
URL:https://www.cvilaseroptics.com/file/general/All_About_Gaussian_Beam_OpticsWEB.pdf

[50] Jing, X., Sun, X., Wu, J. and Meng, K. (2001), 'Effect of grazing flow on the acoustic impedance of an orifice', *AIAA journal* **39**(8), 1478–1484.

[51] Jones, P., Trenberth, K., Ambenje, P., Bojariu, R., Easterling, D., Klein, T., Parker, D., Renwick, J., Rusticucci, M., Soden, B. et al. (2007), 'Observations: surface and atmospheric climate change', *Climate change* pp. 235–336.

[52] Kamm, R. D. (1976), 'Detection of weakly absorbing gases using a resonant optoacoustic method', *Journal of Applied Physics* **47**(8), 3550–3558.
URL:`https://doi.org/10.1063/1.323153`

[53] Kerr, E. L. and Atwood, J. G. (1968), 'The laser illuminated absorptivity spectrophone: a method for measurement of weak absorptivity in gases at laser wavelengths', *Applied optics* **7**(5), 915–921.

[54] Kim, H., Gilmore, C., Pique, A., Horwitz, J., Mattoussi, H., Murata, H., Kafafi, Z. and Chrisey, D. (1999), 'Electrical, optical, and structural properties of indium–tin–oxide thin films for organic light-emitting devices', *Journal of Applied Physics* **86**(11), 6451–6461.

[55] Kim, H., Pique, A., Horwitz, J., Mattoussi, H., Murata, H., Kafafi, Z. and Chrisey, D. (1999), 'Indium tin oxide thin films for organic light-emitting devices', *Applied physics letters* **74**(23), 3444–3446.

[56] King, W., Parkin, D. and Handsworth, R. (1978), 'A hot-wire liquid water device having fully calculable response characteristics', *Journal of Applied Meteorology* **17**(12), 1809–1813.

[57] Kocha, S. S. (2011), Electrochemical degradation: electrocatalyst and support durability, *in* M. M. Mench, E. C. Kumbur and T. N. Veziroglu, eds, 'Polymer electrolyte fuel cell degradation', Academic Press, pp. 89–214.

[58] Korolev, A., Strapp, J., Isaac, G. and Nevzorov, A. (1998), 'The nevzorov airborne hot-wire lwc–twc probe: Principle of operation and performance characteristics', *Journal of Atmospheric and Oceanic Technology* **15**(6), 1495–1510.

[59] Kosterev, A. A., Tittel, F. K., Knittel, T. S., Cowie, A. and Tate, J. D. (2006), Trace humidity sensor based on quartz-enhanced photoacoustic spectroscopy, *in* 'Laser Applications to Chemical, Security and Environmental Analysis', Optical Society of America, p. TuA2.

[60] Kou, L., Labrie, D. and Chylek, P. (1993), 'Refractive indices of water and ice in the 0.65-to 2.5-μm spectral range', *Applied optics* **32**(19), 3531–3540.

[61] Kreuzer, L. B. (1971), 'Ultralow gas concentration infrared absorption spectroscopy', *Journal of Applied Physics* **42**(7), 2934–2943.
URL:`https://doi.org/10.1063/1.1660651`

[62] Kreuzer, L. B. (1977), *Optoacoustic spectroscopy and detection, edited by Y-H.Pao*, Academic Press, New York, chapter: The physics of signal generation and detection, pp. 1–25.

[63] Landry, J. (2008), Optical oblique-incidence reflectivity difference microscopy: Application to label-free detection of reactions in biomolecular microarrays, PhD thesis, University of California, Davis.

[64] Lang, B. and Bergmann, A. (2016), Design framework for a gas sensor based on an open photoacoustic resonator, *in* '2016 IEEE SENSORS', pp. 1–3.

[65] Larminie, J. and Dicks, A. (2013), *Fuel Cell Systems Explained*, second edition edn, John Wiley & Sons Ltd.

[66] Li, X., Wanlass, M., Gessert, T., Emery, K. and Coutts, T. (1989), 'High-efficiency indium tin oxide/indium phosphide solar cells', *Applied Physics Letters* **54**(26), 2674–2676.

[67] Long, R., Chen, Q., Zhang, L., Ma, L. and Quan, S. (2013), 'Online soft sensor of humidity in pem fuel cell based on dynamic partial least squares', *The Scientific World Journal* **2013**.

[68] Lozán, J., Karbe, L. and Neukirch, U. (2003), 'Wasser als Grundlage des Lebens', *Warnsignal Klima: Genug Wasser für alle* .

[69] Magnes, J., Odera, D., Hartke, J., Fountain, M., Florence, L. and Davis, V. (2006), 'Quantitative and qualitative study of gaussian beam visualization techniques', *arXiv preprint physics/0605102* .
URL:`https://arxiv.org/pdf/physics/0605102.pdf`

[70] Maruyama, T. and Fukui, K. (1991), 'Indium tin oxide thin films prepared by chemical vapour deposition', *Thin solid films* **203**(2), 297–302.

[71] Mattiello, M. (2008), Gas traces measurement by photoacoustic spectroscopy using Helmholtz resonator-based sensors, PhD thesis, EPFL, Lausanne.

[72] Mei-Zhen, G., Job, R., De-Sheng, X. and Fahrner, W. (2008), 'Thickness dependence of resistivity and optical reflectance of ito films', *Chinese Physics Letters* **25**(4), 1380.

[73] Meyer, P. L. and Sigrist, M. W. (1990), 'Atmospheric pollution monitoring using co2-laser photoacoustic spectroscopy and other techniques', *Review of Scientific Instruments* **61**(7), 1779–1807.
URL:https://doi.org/10.1063/1.1141097

[74] Miklós, A. (2015), 'Acoustic aspects of photoacoustic signal generation and detection in gases', *International Journal of Thermophysics* **36**(9), 2285–2317.

[75] Miklós, A., Hess, P. and Bozóki, Z. (2001), 'Application of acoustic resonators in photoacoustic trace gas analysis and metrology', *Review of scientific instruments* **72**(4), 1937–1955.

[76] Miklós, A. and Hess, P. (2000), 'Peer reviewed: Modulated and pulsed photoacoustics in trace gas analysis', *Analytical Chemistry* **72**(1), 30 A–37 A.
URL:https://doi.org/10.1021/ac002681m

[77] Mingfang, L. and Haiguo, L. (1993), 'Saw temperature and humidity sensor with high resolution', *Sensors and Actuators B: Chemical* **12**(1), 53–56.

[78] Nath, P., Bunshah, R. F., Basol, B. and Staffsud, O. (1980), 'Electrical and optical properties of In2O3: sn films prepared by activated reactive evaporation', *Thin Solid Films* **72**(3), 463–468.

[79] Newport, C. (2017), 'Focusing and collimating', Optics - Technical reference and fundamental applications. [Online] Accessed: 2017-03-02.
URL:https://www.newport.com/n/focusing-and-collimating

[80] Nonobe, Y. (2017), 'Development of the fuel cell vehicle mirai', *IEEJ Transactions on Electrical and Electronic Engineering* **12**(1), 5–9.

[81] Norbert Wagner, A. K. F. (2011), 'Theory and application of electrochemical impedance spectroscopy for fuel cell characterization', Presentation at the 9th International Microsymposium on Electrochemical Impedance Analysis. [Online] Accessed: 2018-08-01.
URL:`https://elib.dlr.de/71381/1/Presentation_Rovinj_2011_Wagner_short.pdf`

[82] O'hayre, R., Cha, S.-W., Prinz, F. B. and Colella, W. (2016), *Fuel cell fundamentals*, third edition edn, John Wiley & Sons.

[83] Olsson, C.-O. and Landolt, D. (2003), 'Passive films on stainless steels—chemistry, structure and growth', *Electrochimica acta* **48**(9), 1093–1104.

[84] Pascal-Delannoy, F., Sorli, B. and Boyer, A. (2000), 'Quartz crystal microbalance (qcm) used as humidity sensor', *Sensors and Actuators A: Physical* **84**(3), 285 – 291.
URL:`http://www.sciencedirect.com/science/article/pii/S0924424700003915`

[85] Paschotta, R. (2010), *Field guide to optical fiber technology*, SPIE Press.

[86] Plass, W., Maestle, R., Wittig, K., Voss, A. and Giesen, A. (1997), 'High-resolution knife-edge laser beam profiling', *Optics Communications* **134**(1), 21 – 24.

[87] Preece, W. H. (1881), 'I. on the conversion of radiant energy into sonorous vibrations', *Proceedings of the Royal Society of London* **31**(206-211), 506–520.

[88] Pukrushpan, J. T. (2003), Modeling and control of fuel cell systems and fuel processors, PhD thesis, University of Michigan Ann Arbor, Department of Mechanical Engineering.

[89] Röntgen, W. C. (1881), 'On tones produced by the intermittent irradiation of a gas', *The London, Edinburgh, and Dublin Philosophical Magazine and Journal of Science* **11**(68), 308–311.

[90] Roveti, D. K. (2001), 'Choosing a humidity sensor: A review of three technologies this discussion of the operating principles of capacitive, resisitive, and thermal conductivity humidity sensors also addresses their advantages, disadvantages, and applications', *Sensors-the Journal of Applied Sensing Technology* **18**(7), 54–58.

[91] Sasaki, K., Shao, M. and Adzic, R. (2009), Dissolution and stabilization of platinum in oxygen cathodes, *in* F. N. Büchi, M. Inaba and T. J. Schmidt, eds, 'Polymer Electrolyte Fuel Cell Durability', Springer New York, New York, NY, pp. 7–27.

[92] Schilt, S., Besson, J.-P. and Thévenaz, L. (2006), 'Near-infrared laser photoacoustic detection of methane: the impact of molecular relaxation', *Applied Physics B* **82**(2), 319–328.

[93] Schmidt, G. A., Ruedy, R., Miller, R. L. and Lacis, A. A. (2010), 'The attribution of the present-day total greenhouse effect', *J. Geophys. Res.* **115**, D20106.

[94] Schnabel, A. (2016), Material compatibility studies for low temperature pem-fc subsystems, Master's thesis, University of Technology Graz, Institute of Solid State Physics.

[95] Science Engineering Associates, I. (2016), 'Wcm-2000 documentation'. [Online] Accessed: 2018-08-03.

[96] Segelstein, D. J. (1981), The complex refractive index of water, PhD thesis, University of Missouri–Kansas City.

[97] Sensirion (2018), 'How to understand specification of relative humidity sensors', Sensor Specification Statement. [Online] Accessed: 2018-07-01.
URL:`https://www.sensirion.com/fileadmin/user_upload/customers/sensirion/Dokumente/2_Humidity_Sensors/Sensirion_Humidity_Sensors_Specification_Statement.pdf`

[98] Siegman, A. E. (1986), *Lasers*, University Science Books, chapter: 14-17, pp. 558–697.

[99] Sigrist, M. (2017), Photoacoustic spectroscopy, applications, *in* J. C. Lindon, G. E. Tranter and D. W. Koppenaal, eds, 'Encyclopedia of Spectroscopy and Spectrometry (Third Edition)', third edition edn, Academic Press, Oxford, pp. 589 – 597.
URL:`http://www.sciencedirect.com/science/article/pii/B9780124095472113071`

[100] Silfvast, W. T. (2004), *Laser fundamentals*, Cambridge university press, chapter: 11-12, pp. 371–433.

[101] Smode, W. (2016), Development of a sensor shield for fuel cell applications, Master's thesis, FH Joanneum Graz.

[102] Soden, B. J. and Held, I. M. (2006), 'An assessment of climate feedbacks in coupled ocean–atmosphere models', *Journal of Climate* **19**(14), 3354–3360.

[103] Solomon, S., Rosenlof, K. H., Portmann, R. W., Daniel, J. S., Davis, S. M., Sanford, T. J. and Plattner, G.-K. (2010), 'Contributions of stratospheric water vapor to decadal changes in the rate of global warming', *Science* **327**(5970), 1219–1223.

[104] Source, L. D. (2018), 'Understanding current and temperature tuning coefficients'. [Online] Accessed: 2018-08-02.
URL:`https://www.laserdiodesource.com/laser-diode-tuning`

[105] Springer, T. E., Zawodzinski, T. and Gottesfeld, S. (1991), 'Polymer electrolyte fuel cell model', *Journal of the electrochemical society* **138**(8), 2334–2342.

[106] Srouji, A.-K. and Mench, M. M. (2011), Freeze damage to polymer electrolyte fuel cells, *in* M. M. Mench, E. C. Kumbur and T. N. Veziroglu, eds, 'Polymer electrolyte fuel cell degradation', Academic Press, pp. 293–333.

[107] Sun, H. (2015), *A practical guide to handling laser diode beams*, Springer, chapter: 2, pp. 27–51.

[108] Sung, W., Song, Y.-I., Yu, K.-H. and Lim, T.-W. (2010), 'Recent advances in the development of hyundai - kia's fuel cell electric vehicles', *SAE International Journal of Engines* **3**(1), 768–772.

[109] Tang, C. W. and VanSlyke, S. A. (1987), 'Organic electroluminescent diodes', *Applied physics letters* **51**(12), 913–915.

[110] Thorlabs, I. (2016), *BC106 M2MS-BC106 Operation Manual*, Thorlabs, Inc, Newton, NJ.

[111] Tonon, D. (2011), Aeroacoustics of shear layers in internal flows : closed branches and wall perforations, PhD thesis, Department of Applied Physics.

[112] Träger, F. (2012), *Springer handbook of lasers and optics*, Springer Science & Business Media, chapter: 1-3, pp. 3–159.

[113] Tyndall, J. (1880), 'Action of an intermittent beam of radiant heat upon gaseous matter', *Proceedings of the Royal Society of London* **31**, 307–317.

[114] Vaisala (2015), 'Vaisala humicap® sensor for measuring relative humidity'. [Online] Accessed: 2018-08-02.
URL:`https://www.vaisala.com/sites/default/files/documents/HUMICAP-Technology-description-B210781EN-C_0.pdf`

[115] Vaisala (2018), 'Hmt330 series humidity and temperature transmitters'. [Online] Accessed: 2018-08-20.
URL:`https://www.vaisala.com/sites/default/files/documents/HMT330-Series-Datasheet-B210951EN.pdf`

[116] Walker, B. E. and Charwat, A. F. (1982), 'Correlation of the effects of grazing flow on the impedance of helmholtz resonators', *The Journal of the Acoustical Society of America* **72**(2), 550–555.

[117] Warren, S. G. (1984), 'Optical constants of ice from the ultraviolet to the microwave', *Applied optics* **23**(8), 1206–1225.

[118] Wozniak, B. and Dera, J. (2007), *Light absorption in sea water*, Vol. 33, Springer.

[119] Wu, W.-F., Chiou, B.-S. and Hsieh, S.-T. (1994), 'Effect of sputtering power on the structural and optical properties of RF magnetron sputtered ITO films', *Semiconductor science and technology* **9**(6), 1242.

[120] Yoshida, T. and Kojima, K. (2015), 'Toyota mirai fuel cell vehicle and progress toward a future hydrogen society', *The Electrochemical Society Interface* **24**(2), 45–49.

[121] Zawodzinski, T. A., Derouin, C., Radzinski, S., Sherman, R. J., Smith, V. T., Springer, T. E. and Gottesfeld, S. (1993), 'Water uptake by and transport through nafion® 117 membranes', *Journal of the electrochemical society* **140**(4), 1041–1047.

[122] Zawodzinski, T. A., Springer, T. E., Davey, J., Jestel, R., Lopez, C., Valerio, J. and Gottesfeld, S. (1993), 'A comparative study of water uptake by and transport through ionomeric fuel cell membranes', *Journal of the Electrochemical Society* **140**(7), 1981–1985.